

CERN-PH-EP/2013-037
2022/03/06

CMS-TAU-14-001

Reconstruction and identification of τ lepton decays to hadrons and ν_τ at CMS

The CMS Collaboration*

Abstract

This paper describes the algorithms used by the CMS experiment to reconstruct and identify $\tau \rightarrow \text{hadrons} + \nu_\tau$ decays during Run 1 of the LHC. The performance of the algorithms is studied in proton-proton collisions recorded at a centre-of-mass energy of 8 TeV, corresponding to an integrated luminosity of 19.7 fb^{-1} . The algorithms achieve an identification efficiency of 50–60%, with misidentification rates for quark and gluon jets, electrons, and muons between per mille and per cent levels.

Published in the Journal of Instrumentation as doi:10.1088/1748-0221/11/01/P01019.

1 Introduction

Decays of τ leptons provide an important experimental signature for analyses at the CERN LHC. Evidence for decays of the standard model (SM) Higgs boson (H) into $\tau\tau$ has been reported [1, 2], as have searches for neutral and charged Higgs bosons in decays to τ leptons that have special interest in the context of the minimal supersymmetric extension of the SM (MSSM) [3–8]. The CMS collaboration has published analyses of Drell–Yan ($q\bar{q} \rightarrow Z/\gamma^* \rightarrow \tau\tau$) and top quark pair production [9–11] in final states with τ leptons. Searches for supersymmetry, leptoquarks, W' and Z' bosons, as well as other non-SM Higgs bosons [12–17] benefit from the high performance τ reconstruction and identification capabilities of the CMS detector.

With a mass of $m_\tau = 1.777 \text{ GeV}$ [18], the τ is the only lepton heavy enough to decay into hadrons (h), and it does so in about two thirds of the cases, typically into either one or three charged pions or kaons and up to two neutral pions (π^0), and one neutrino (ν_τ). The π^0 meson decays almost exclusively into $\gamma\gamma$. In about 35% of the cases, τ leptons decay into an electron or muon and two neutrinos. The branching fractions for the main τ decay modes are given in Table 1. The decays $\tau^- \rightarrow h^- \pi^0 \nu_\tau$, $\tau^- \rightarrow h^- \pi^0 \pi^0 \nu_\tau$, and $\tau^- \rightarrow h^- h^+ h^- \nu_\tau$ (with corresponding channels for τ^+) proceed via intermediate $\rho(770)$ and $a_1(1260)$ meson resonances. The electrons and muons originating from τ decays are difficult to distinguish from electrons and muons produced directly in the primary proton-proton (pp) interaction, and are handled using the standard CMS algorithms for electron and muon reconstruction and identification. The algorithms for τ reconstruction and identification presented in this paper focus on τ lepton decays to hadrons + ν_τ , that we refer to as “hadronic” τ decays and denote by τ_h . The algorithms provide the means for reconstructing individually the dominant τ_h decay modes. In comparing the energies of reconstructed τ_h candidates to their true energies, we refer to the charged hadrons and neutral pions produced in the τ decay as “visible” τ decay products, and ignore the ν_τ .

Table 1: Approximate branching fractions (\mathcal{B}) of different τ decay modes [18]. The generic symbol h^- represents a charged hadron (either a pion or a kaon). Charge conjugation invariance is assumed in this paper.

Decay mode	Meson resonance	$\mathcal{B} [\%]$
$\tau^- \rightarrow e^- \bar{\nu}_e \nu_\tau$		17.8
$\tau^- \rightarrow \mu^- \bar{\nu}_\mu \nu_\tau$		17.4
$\tau^- \rightarrow h^- \nu_\tau$		11.5
$\tau^- \rightarrow h^- \pi^0 \nu_\tau$	$\rho(770)$	26.0
$\tau^- \rightarrow h^- \pi^0 \pi^0 \nu_\tau$	$a_1(1260)$	9.5
$\tau^- \rightarrow h^- h^+ h^- \nu_\tau$	$a_1(1260)$	9.8
$\tau^- \rightarrow h^- h^+ h^- \pi^0 \nu_\tau$		4.8
Other modes with hadrons		3.2
All modes containing hadrons		64.8

The mean lifetime of τ leptons at rest is $290 \times 10^{-15} \text{ s}$ [18]. The distances that τ leptons travel between their production and decay are small, but nevertheless significant compared to the transverse impact parameter and secondary-vertex resolution of the CMS tracking detector [19]. Energetic τ leptons originating from Z or SM Higgs boson decays typically traverse distances of a few millimetres before decaying.

The main challenge in identifying hadronic τ decays is distinguishing them from quark and gluon jet background. The cross section for multijet production from perturbative quantum chromodynamical (QCD) calculations exceeds by many orders of magnitude the rate at which

τ leptons are produced at the LHC. To reduce the background arising from quark and gluon jets, we exploit the fact that hadronic τ decays result in a lower particle multiplicity, and are more collimated and isolated relative to other particles in the event. In some analyses, the misidentification of electrons or muons as τ_h candidates may constitute a sizeable problem, and dedicated algorithms have been developed to reduce this type of background.

The performance of τ_h reconstruction and identification algorithms has been validated using the first LHC data recorded at $\sqrt{s} = 7$ TeV [20]. Since then, the algorithms have been further developed, especially to improve their performance in dealing with additional inelastic pp interactions (pileup) that occur in the same bunch crossing as the hard scattering of interest. Moreover, the rejection of backgrounds arising from misidentification of jets, electrons, and muons as τ_h has improved significantly through the introduction of multivariate analysis (MVA) techniques. In this paper, we report on the performance of the improved algorithms used to analyze the 8 TeV pp data at CMS, corresponding to an integrated luminosity of 19.7 fb^{-1} .

The paper is organized as follows. The CMS detector is described briefly in Section 2. Section 3 describes the data and the Monte Carlo (MC) simulations used for studying the performance of τ_h reconstruction and identification. The reconstruction of electrons, muons, and jets, along with various kinematic quantities is described in Section 4. The algorithms used for reconstruction and identification of τ_h decays are detailed in Section 5. The performance of the algorithms in simulated events is presented in Section 6. Sections 7–11 detail the validation of the algorithms with data. The results are summarized in Section 12.

2 CMS detector

The central feature of the CMS detector is a superconducting solenoid of 6 m internal diameter, providing a magnetic field of 3.8 T. A silicon pixel and strip tracker, a lead tungstate crystal electromagnetic calorimeter (ECAL), and a brass and scintillator hadron calorimeter (HCAL), each composed of a barrel and two endcap sections, are positioned within the solenoid volume. Muons are measured and identified in gas-ionization detectors embedded in the steel flux-return yoke outside the solenoid. Extensive forward calorimetry complements the coverage provided by the barrel and endcap detectors.

The CMS tracker is a cylindrical detector of 5.5 m length and 2.5 m diameter, constructed entirely of silicon modules. It provides an active sensor area of about 200 m^2 to reconstruct charged particles within the pseudorapidity range $|\eta| < 2.5$. The innermost region around the interaction point, subject to the highest particle flux, is instrumented with silicon pixel sensors. The central part of the pixel detector consists of three cylindrical layers, installed at transverse radii of $r = 4.4, 7.3$, and 10.2 cm , which extend over a total length of 53 cm . The central part is complemented by two forward endcap disks of radius $6 < r < 15 \text{ cm}$, located at longitudinal distances $|z| = 34.5$ and 46.5 cm on either side of the interaction point. The central part of the silicon strip detector consists of ten cylindrical layers and twelve endcap disks that surround the pixel detector volume. The cylindrical layers cover radial distances of up to 108 cm and $|z| < 109 \text{ cm}$, and the disks cover up to $r < 113 \text{ cm}$ and $|z| < 280 \text{ cm}$. Tracks of charged hadrons are reconstructed with an efficiency of 75–95% that depends on the transverse momentum p_T and η [21].

The silicon tracker adds a significant amount of material in front of the ECAL, mainly because of the mechanical structure, the services, and the cooling system. Figure 1 shows, as a function of η , the number of radiation lengths (X_0) of material that particles produced at the interaction point must traverse before they reach the ECAL. This rises from about $0.4X_0$ at $|\eta| \approx 0$ to about

$2.0X_0$ at $|\eta| \approx 1.4$, and decreases to about $1.3X_0$ at $|\eta| \approx 2.5$. As a result, photons originating from $\pi^0 \rightarrow \gamma\gamma$ decays have a high probability for converting to e^+e^- pairs within the volume of the tracking detector.

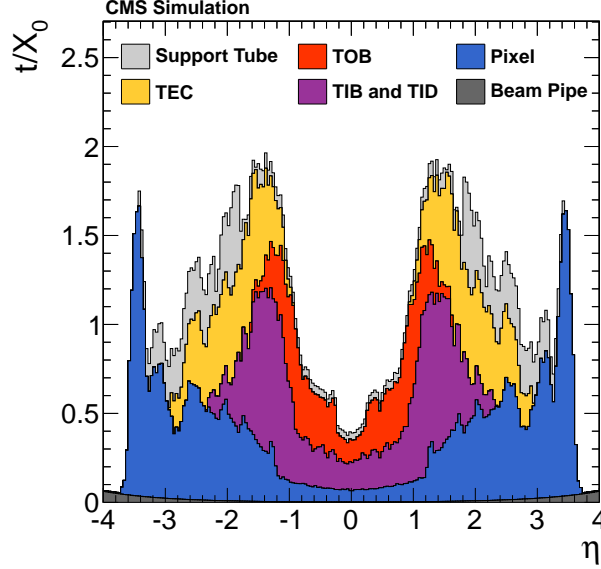


Figure 1: The total material thickness (t) in units of radiation length X_0 , as a function of η , that a particle produced at the interaction point must traverse before it reaches the ECAL. The material used for sensors, readout electronics, mechanical structures, cooling, and services is given separately for the silicon pixel detector and for individual components of the silicon strip detector (“TEC”, “TOB”, “TIB and TID”) [21]. The material used for the beam pipe and for the support tube that separates the tracker from the ECAL is also shown separately.

The ECAL is a homogeneous and hermetic calorimeter made of PbWO_4 scintillating crystals. It is composed of a central barrel, covering $|\eta| < 1.48$, and two endcaps covering $1.48 < |\eta| < 3.0$. The barrel is made of 61 200 trapezoidal crystals of front-face transverse section $22 \times 22 \text{ mm}^2$, giving a granularity of 0.0174×0.0174 in η and azimuth ϕ , and a length of 230 mm ($25.8X_0$). The crystals are organized in 36 supermodules, 18 on each side of $\eta = 0$. Each supermodule contains 1700 crystals, covers $\pi/9$ radians in ϕ , and is made of four modules along η . This structure has a few thin uninstrumented regions between the modules in η (at $|\eta| = 0, 0.435, 0.783, 1.131$, and 1.479), and between the supermodules in ϕ (every $\pi/9$ radians). The crystals are installed with a quasi-projective geometry, tilted by an angle of 3° relative to the projective axis that passes through the centre of CMS (the nominal interaction point), to minimize the passage of electrons or photons through uninstrumented regions. The endcaps consist of a total of 14 648 trapezoidal crystals with front-face transverse sections of $28.62 \times 28.62 \text{ mm}^2$, and lengths of 220 mm ($24.7X_0$). The small radiation length ($X_0 = 0.89 \text{ cm}$) and small Molière radius (2.3 cm) of the PbWO_4 crystals provide a compact calorimeter with excellent two-shower separation.

The HCAL is a sampling calorimeter, with brass as passive absorber, and plastic scintillator tiles serving as active material, and provides coverage for $|\eta| < 2.9$. The calorimeter cells are grouped in projective towers of approximate size 0.087×0.087 in $\eta \times \phi$ in the barrel and 0.17×0.17 in the endcaps.

The muon system is composed of a cylindrical barrel section, and two planar endcaps that surround the solenoid with about $25\,000 \text{ m}^2$ of detection planes. Drift tube (DT) and cathode strip chamber (CSC) layers provide muon reconstruction, identification, and trigger capability

within $|\eta| < 2.4$. The muon system consists of four muon stations, located at different distances from the centre of CMS, and separated by layers of steel plates. Drift tubes are installed in the barrel region $|\eta| < 1.2$, where the muon rate is low and the magnetic field in the return yoke is uniform. Each DT station contains eight layers of tubes that measure the position in the transverse plane (r - ϕ), and four layers that provide position information in the r - z plane, except for the outermost station, which contains only eight r - ϕ layers. In the endcaps, where the muon rates as well as the background from neutron radiation are higher and the magnetic field is non-uniform, CSC detectors cover the region $0.9 < |\eta| < 2.4$. Each CSC station contains six layers of anode wires and cathode planes to measure the position in the bending plane (precise in ϕ , coarse in r). The combination of DT and CSC detectors covers the pseudorapidity interval $|\eta| < 2.4$ without any gaps in acceptance. The DT and CSC systems are complemented by a system of resistive-plate chambers (RPC) that provide precise timing signals for triggering on muons within the region $|\eta| < 1.6$. Particles produced at the nominal interaction point must traverse more than 10 and 15 interaction lengths (λ) of absorber material before they reach their respective innermost and outermost detection planes. This greatly reduces the contribution from punch-through particles.

The first level of the CMS trigger system, based on special hardware processors, uses information from calorimeters and muon detectors to select the most interesting events in a fixed time interval of $< 4 \mu\text{s}$. The high-level trigger processor farm further decreases the event rate from $< 100 \text{ kHz}$ to $\approx 400 \text{ Hz}$, before data storage.

A more detailed description of the CMS detector and of the kinematic variables used in the analysis can be found in Ref. [19].

3 Data samples and Monte Carlo simulation

The τ reconstruction and identification performance in the data is compared with MC simulations, using samples of $Z/\gamma^* \rightarrow \ell\ell$ (ℓ corresponds to e , μ , and τ), W +jets, $t\bar{t}$, single top quark, diboson (WW , WZ , and ZZ), and QCD multijet events. The W +jets, $t\bar{t}$, and diboson samples are generated using the leading-order (LO) MADGRAPH 5.1 program [22], and single top quark events with the next-to-leading-order (NLO) program POWHEG 1.0 [23–25]. The $Z/\gamma^* \rightarrow \ell\ell$ samples are generated using MADGRAPH and POWHEG. The QCD multijet samples are produced using the LO generator PYTHIA 6.4 [26] with the Z2* tune. In fact, PYTHIA with the Z2* tune is also used to model parton shower and hadronization processes for all MC event samples. The PYTHIA Z2* tune is obtained from the Z1 tune [27], which uses the CTEQ5L parton distribution functions (PDF), whereas Z2* adopts CTEQ6L [28]. The decays of τ leptons, including polarization effects, are modelled with TAUOLA [29]. The samples produced by PYTHIA and MADGRAPH are based on the CTEQ6L1 set of PDFs, while the samples produced by POWHEG use CTEQ6M [28]. The $Z/\gamma^* \rightarrow \ell\ell$ and W +jets events are normalized to cross sections computed at next-to-next-to-leading-order accuracy [30]. The $t\bar{t}$ production cross section measured by CMS [31] is used to normalize the $t\bar{t}$ sample. A reweighting is applied to MC-generated $t\bar{t}$ events to improve the modelling of the p_T spectrum of the top quark relative to data [32, 33]. The cross sections for single top quark and diboson production are computed at NLO accuracy [34].

Simulated samples of hypothetical heavy Higgs bosons and heavy charged (W') and neutral (Z') gauge bosons are used to train MVA-based τ identification discriminators. The heavy H , W' , and Z' boson events are generated using the PYTHIA program and increase the size of the training sample with τ leptons of high p_T , for which the SM production rate is very small. The Higgs boson samples are produced in the mass range 80–1000 GeV, the W' and Z' samples in

the mass range 900–4000 GeV and 750–2500 GeV, respectively. The list of training samples is complemented by SM $H \rightarrow \tau\tau$ events, generated using POWHEG. The QCD samples used for the MVA training extend up to a scale of $\hat{p}_T = 3000$ GeV.

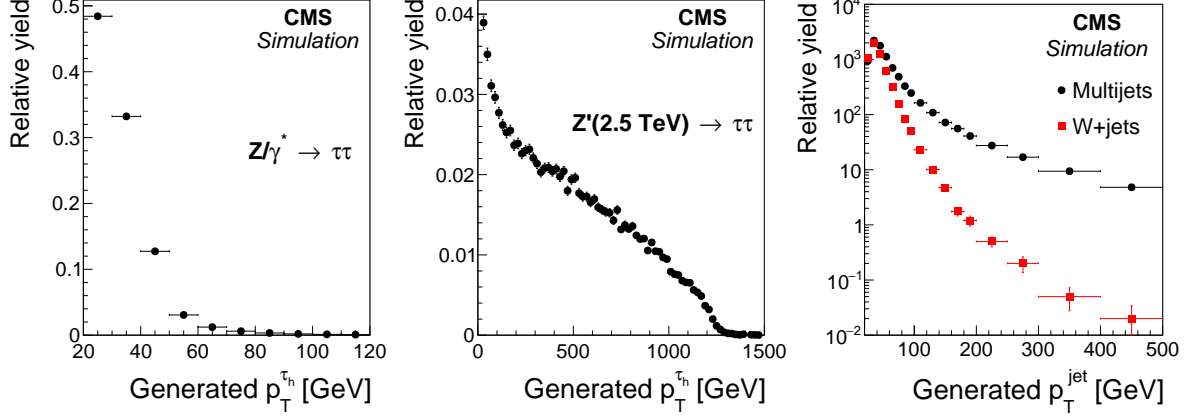


Figure 2: Transverse momentum distributions of the visible decay products of τ_h decays, in (left) simulated $Z/\gamma^* \rightarrow \tau\tau$ events, (middle) $Z'(2.5 \text{ TeV}) \rightarrow \tau\tau$ events, and (right) of quark and gluon jets in simulated W+jets and multijet events, at the generator level.

The transverse momentum distribution of the visible τ decay products in simulated $Z/\gamma^* \rightarrow \tau\tau$ and $Z' \rightarrow \tau\tau$ events is shown in Fig. 2. The Z' sample is generated for a mass of $m_{Z'} = 2.5 \text{ TeV}$, and used to study the efficiency to identify τ_h decays at high p_T . The p_T distribution of generator level quark and gluon jets in simulated W+jets and QCD multijet events is also shown in the figure. The jets are constructed using the anti- k_T algorithm [35] with a distance parameter of 0.5.

On average, 21 inelastic pp interactions occur per LHC bunch crossing. Minimum bias events generated with PYTHIA are overlaid on all simulated events, according to the luminosity profile of the analyzed data.

All generated events are passed through a detailed simulation of the CMS apparatus, based on GEANT4 [36], and are reconstructed using the same version of the CMS event reconstruction software as used for data.

Small differences between data and MC simulation are observed in selection efficiencies and in energy and momentum measurements of electrons and muons, as well as in the efficiencies for electron, muon, and τ_h final states to pass the trigger requirements. These differences are corrected by applying suitably-chosen weights to simulated events. The corrections are determined by comparing $Z/\gamma^* \rightarrow \ell\ell$ events in simulation and data. Differences in response and resolution of the missing transverse momentum in data and simulation are corrected as described in Ref. [37].

4 Event reconstruction

The information available from all CMS subdetectors is employed in the particle-flow (PF) algorithm [38–41] to identify and reconstruct individual particles in the event, namely muons, electrons, photons, and charged and neutral hadrons. These particles are used to reconstruct jets, τ_h candidates, and the vector imbalance in transverse momentum in the event, referred to as \vec{p}_T^{miss} , as well as to quantify the isolation of leptons.

Electrons are reconstructed by matching tracks in the inner detector with energy depositions

in the ECAL [38, 42]. The tracks of electron candidates are reconstructed using a Gaussian-sum filter (GSF) [43] algorithm, which accounts for the emission of bremsstrahlung photons along the electron trajectory. Energy loss in bremsstrahlung is reconstructed by searching for energy depositions in the ECAL located in directions tangential to the electron track. A multivariate approach based on boosted decision trees (BDT) [44] is employed for electron identification [45]. Observables that quantify the quality of the electron track, the compactness of the electron cluster in directions transverse and longitudinal to the electron track, and the compatibility between the track momentum and the energy depositions in the ECAL are used as inputs to the BDT. Additional requirements are applied to reject electrons originating from photon conversions to e^+e^- pairs in detector material.

The identification of muons is based on linking track segments reconstructed in the silicon tracking detector and in the muon system [46]. The matching between track segments is done outside-in, starting from a track in the muon system, and inside-out, starting from a track reconstructed in the inner detector. In case a link can be established, the track parameters are refitted using the combined hits in the inner and outer detectors, with the resulting track referred to as a global muon track. Quality criteria are applied on the multiplicity of hits, on the number of matched segments, and on the fit quality of the global muon track, quantified through a χ^2 .

Electrons and muons originating from decays of W and Z bosons are expected to be isolated, while leptons from heavy flavour (charm and bottom quark) decays, as well as from in-flight decays of pions and kaons, are often reconstructed within jets. The signal is distinguished from multijet background through the sum of scalar p_T values of charged particles, neutral hadrons, and photons, reconstructed within a cone of size $\Delta R = \sqrt{(\Delta\eta)^2 + (\Delta\phi)^2}$ of 0.4, centred around the lepton direction, using the PF algorithm. Neutral hadrons and photons within the innermost region of the cone are excluded from the sum, to prevent the footprint of the lepton in ECAL and HCAL from causing the lepton to fail isolation criteria. Charged particles close to the direction of electrons are also excluded from the computation, to avoid counting tracks from converted photons emitted by bremsstrahlung. Efficiency loss due to pileup is kept minimal by considering only charged particles originating from the lepton production vertex in the isolation sum. The contribution of the neutral component of pileup to the isolation of the lepton is taken into account by means of so-called $\Delta\beta$ corrections:

$$I_\ell = \sum_{\text{charged}} p_T + \max \left\{ 0, \sum_{\text{neutrals}} p_T - \Delta\beta \right\}, \quad (1)$$

where ℓ corresponds to either e or μ , and the sums extend over, respectively, the charged particles that originate from the lepton production vertex and the neutral particles. Charged and neutral particles are required to be within a cone of size $\Delta R = 0.4$ around the lepton direction. The $\Delta\beta$ corrections are computed by summing the scalar p_T of charged particles that are within a cone of size $\Delta R = 0.4$ around the lepton direction and do not originate from the lepton production vertex, and scaling this sum down by a factor of two:

$$\Delta\beta = 0.5 \sum_{\text{charged, pileup}} p_T. \quad (2)$$

The factor of 0.5 approximates the phenomenological ratio of neutral-to-charged hadron production in the hadronization of inelastic pp collisions.

Collision vertices are reconstructed using a deterministic annealing algorithm [47, 48]. The reconstructed vertex position is required to be compatible with the location of the LHC beam

in the x - y plane. The primary collision vertex (PV) is taken to be the vertex that maximizes $\sum_{\text{tracks}} p_T^2$. The sum extends over all tracks associated with a given vertex.

Jets within the range $|\eta| < 4.7$ are reconstructed using the anti- k_T algorithm [35] with a distance parameter of 0.5. As mentioned previously, the particles reconstructed by the PF algorithm are used as input to the jet reconstruction. Reconstructed jets are required not to overlap with identified electrons, muons, or τ_h within $\Delta R < 0.5$, and to pass two levels of jet identification criteria: (i) misidentified jets, mainly arising from calorimeter noise, are rejected by requiring reconstructed jets to pass a set of loose jet identification criteria [49] and (ii) jets originating from pileup interactions are rejected through an MVA-based jet identification discriminant, relying on information about the vertex and energy distribution within the jet [50]. The energy of reconstructed jets is calibrated as a function of jet p_T and η [51]. The contribution of pileup to the energy of jets originating from the hard scattering is compensated by determining a median transverse momentum density (ρ) for each event, and subtracting the product of ρ times the area of the jet, computed in the $\eta - \phi$ plane, from the reconstructed jet p_T [52, 53]. Jets originating from the hadronization of b quarks are identified through the combined secondary vertex (CSV) algorithm [54], which exploits observables related to the long lifetime of b hadrons and the higher particle multiplicity and mass of b jets compared to light-quark and gluon jets.

Two algorithms are used to reconstruct \vec{p}_T^{miss} , the imbalance in transverse momentum in the event, whose magnitude is referred to as E_T^{miss} . The standard algorithm computes the negative vectorial sum of all particle momenta reconstructed using the PF algorithm. In addition, a multivariate regression algorithm [37] has been developed to reduce the effect of pileup on the resolution in E_T^{miss} . The algorithm utilizes the fact that pileup predominantly produces jets of low p_T , while leptons and high- p_T jets are produced almost exclusively in the hard-scatter.

The transverse mass, m_T , of the system constituted by an electron or a muon and E_T^{miss} is used to either select or remove events that are due to W +jets and $t\bar{t}$ production. It is defined by:

$$m_T = \sqrt{2p_T^\ell E_T^{\text{miss}} (1 - \cos \Delta\phi)}, \quad (3)$$

where the symbol ℓ refers to electron or muon and $\Delta\phi$ denotes the difference in azimuthal angle between the lepton momentum and the \vec{p}_T^{miss} vector.

5 Algorithm for τ_h reconstruction and identification

The τ_h decays are reconstructed and identified using the hadrons-plus-strips (HPS) algorithm [20]. The algorithm is designed to reconstruct individual decay modes of the τ lepton, taking advantage of the excellent performance of the PF algorithm in reconstructing individual charged and neutral particles.

The reconstruction and identification of τ_h decays in the HPS algorithm is performed in two steps:

1. **Reconstruction:** combinations of charged and neutral particles reconstructed by the PF algorithm that are compatible with specific τ_h decays are constructed, and the four-momentum, expressed in terms of (p_T , η , ϕ , and mass) of τ_h candidates, is computed.
2. **Identification:** discriminators that separate τ_h decays from quark and gluon jets, and from electrons and muons, are computed. This provides a reduction in the jet $\rightarrow \tau_h$, $e \rightarrow \tau_h$, and $\mu \rightarrow \tau_h$ misidentification rates.

The HPS algorithm is seeded by jets of $p_T > 14 \text{ GeV}$ and $|\eta| < 2.5$, reconstructed using the anti- k_T algorithm [35] with a distance parameter of 0.5. The p_T criterion is applied on the jet momentum given by the vectorial sum of all particle constituents of the jet, before the jet energy calibration and pileup corrections described in Section 4 are taken into account.

5.1 Identification of decay modes

Reconstruction of specific τ_h decay modes requires reconstruction of neutral pions that are present in most of the hadronic τ decays. The high probability for photons originating from $\pi^0 \rightarrow \gamma\gamma$ decays to convert to e^+e^- pairs within the volume of the CMS tracking detector is taken into account by clustering the photon and electron constituents of the τ -seeding jet into “strips” in the $\eta - \phi$ plane. The clustering of electrons and photons of $p_T > 0.5 \text{ GeV}$ into strips proceeds via an iterative procedure. The electron or photon of highest p_T not yet included into any strip is used to seed a new strip. The initial position of the strip in the $\eta - \phi$ plane is set according to the η and ϕ of the seed e or γ . The e or γ of next-highest p_T that is within an $\eta \times \phi$ window centred on the strip location is merged into the strip. The strip position is then recomputed as an energy-weighted average of all electrons and photons contained in the strip:

$$\eta_{\text{strip}} = \frac{1}{p_T^{\text{strip}}} \sum p_T^{\gamma} \eta_{\gamma}$$

$$\phi_{\text{strip}} = \frac{1}{p_T^{\text{strip}}} \sum p_T^{\gamma} \phi_{\gamma},$$

with $p_T^{\text{strip}} = \sum p_T^{\gamma}$. The construction of the strip ends when no additional electrons or photons are found within an $\eta \times \phi$ window of size 0.05×0.20 . In which case the clustering proceeds by constructing a new strip, which is seeded by the e or γ with next highest p_T . The size of the window is enlarged in the ϕ direction to account for the bending of e^+ and e^- from photon conversions in the 3.8 T magnetic field. Strips with p_T sums of electrons and photons in the strip of $> 2.5 \text{ GeV}$ are kept as π^0 candidates.

Hadronic τ candidates are formed by combining the strips with the charged-particle constituents of the jet. The charged particles are required to satisfy the condition $p_T > 0.5 \text{ GeV}$. The distance of closest approach between their tracks and the hypothetical production vertex of the τ_h candidate, taken to be the vertex closest to the charged particle of highest p_T within the jet, is required to be less than 0.4 cm in the z direction and $< 0.03 \text{ cm}$ in the transverse plane. The requirements for tracks to be compatible with the production vertex of the τ removes spurious tracks and significantly reduces the effect of pileup, while being sufficiently loose so as not to lose efficiency because of the small distances that τ leptons traverse between their production and decay.

A combinatorial approach is taken for constructing hadronic τ candidates. Multiple τ_h hypotheses, corresponding to combinations of either one or three charged particles and up to two strips, are constructed for each jet. To reduce computing time, the set of input objects is restricted to the 6 charged particles and the 6 strips with highest p_T .

The four-momentum of each τ_h candidate hypothesis (p_T , η , ϕ , and mass) is given by the four-momentum sum of the charged particles and strips. In a few per cent of the cases, the charged particles included in the τ_h candidates are identified as electrons or muons, and are assigned their respective electron or muon masses by the PF algorithm. The HPS algorithm sets the mass of all charged particles included in τ_h candidates to that of the charged pion, except for electron constituents of strips, which are treated as massless. The charge of τ_h candidates is

reconstructed by summing the charges of all particles included in the construction of the τ_h candidate, except for the electrons contained in strips. The probability for misreconstructing the τ_h charge is $\approx 1\%$, with a moderate dependence on p_T and η , for taus from Z decays.

The following criteria are applied to assure the compatibility of each hypothesis with the signatures expected for the different τ_h decays in Table 1:

1. $h^\pm h^\mp h^\pm$: Combination of three charged particles with mass $0.8 < m_{\tau_h} < 1.5 \text{ GeV}$. The tracks are required to originate within $\Delta z < 0.4 \text{ cm}$ of the same event vertex, and to have a total charge of one.
2. $h^\pm \pi^0 \pi^0$: Combination of a single charged particle with two strips. The mass of the τ_h candidate is required to satisfy the condition $0.4 < m_{\tau_h} < 1.2 \sqrt{p_T [\text{GeV}]/100 \text{ GeV}}$. The size of the mass window is enlarged for τ_h candidates of high p_T to account for resolution effects. The upper limit on the mass window is constrained to be at least 1.2 and at most 4.0 GeV.
3. $h^\pm \pi^0$: Combination of one charged particle and one strip with mass $0.3 < m_{\tau_h} < 1.3 \sqrt{p_T [\text{GeV}]/100 \text{ GeV}}$. The upper limit on the mass window is constrained to be at least 1.3 and at most 4.2 GeV.
4. h^\pm : A single charged particle without any strips.

The combinations of charged particles and strips considered by the HPS algorithm represent all hadronic τ decay modes in Table 1, except $\tau^- \rightarrow h^- h^+ h^- \pi^0 \nu_\tau$. The latter corresponds to a branching fraction of 4.8%, and is not considered in the present version of the algorithm, because of its contamination by jets. The $h^\pm \pi^0$ and $h^\pm \pi^0 \pi^0$ decays are analyzed together, and referred to as $h^\pm \pi^0 s$.

Hypotheses that fail the mass window selection for the corresponding decay mode are discarded, as are hypotheses that have a charge different from unity, or hypotheses that include any charged hadron or strip outside of a signal cone of $\Delta R = 3.0/p_T [\text{GeV}]$ of the axis given by the momentum vector of the τ_h candidate. The size of the cone takes into account the fact that decay products of energetic τ leptons are more collimated. When ΔR is smaller than 0.05 or exceeds 0.10, a cone of size $\Delta R = 0.05$ or $\Delta R = 0.10$ is used as the limit, respectively.

When multiple combinations of charged hadrons and strips pass the mass window and the signal cone requirements, the hypothesis for the candidate with largest p_T is retained. All other combinations are discarded, resulting in a unique τ_h candidate to be associated to each jet.

The distributions in the decay modes and in the mass of τ_h candidates in $Z/\gamma^* \rightarrow \tau\tau$ events are shown in Fig. 3. The contribution of the $Z/\gamma^* \rightarrow \tau\tau$ signal is split according to the reconstructed τ_h mode, as shown in the legend. For τ_h candidates reconstructed in the $h^\pm \pi^0 s$ and $h^\pm h^\mp h^\pm$ modes, the m_{τ_h} distribution peaks near the intermediate $\rho(770)$ and $a_1(1260)$ meson resonances (cf. Table 1), as expected. The narrow peak at the charged pion mass is due to τ_h candidates reconstructed in the h^\pm mode.

5.2 Tau-isolation discriminants

Requiring reconstructed τ_h candidates to pass strict isolation requirements constitutes the main handle for reducing the large multijet background. Tau leptons are usually isolated relative to other particles in the event, and so are their decay products, in contrast to quark and gluon jets. Two types of τ_h isolation discriminants have been developed, using simple cutoff-based

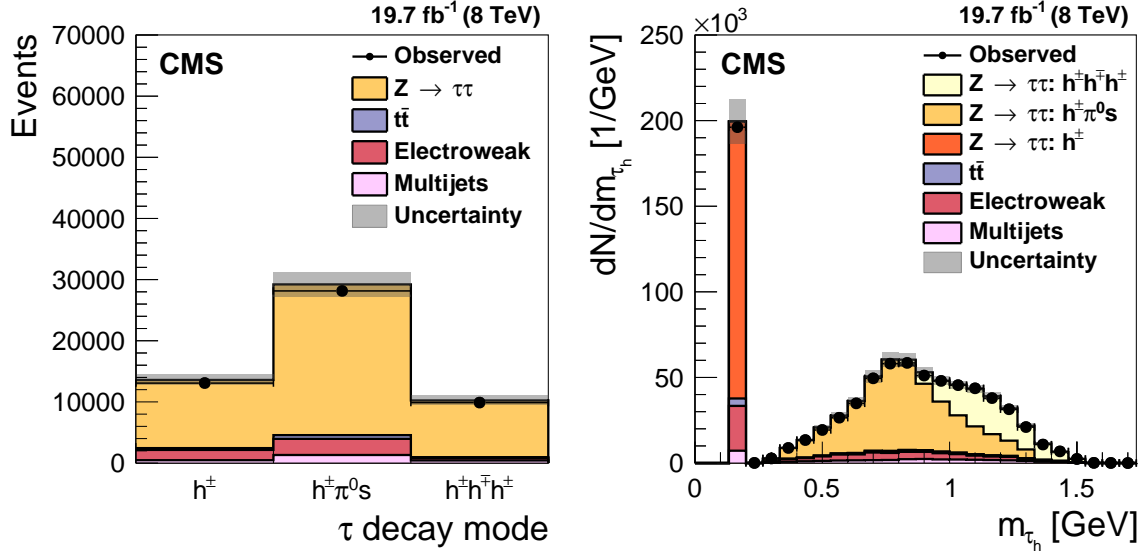


Figure 3: Distributions in (left) reconstructed τ_h decay modes and (right) τ_h candidate masses in $Z/\gamma^* \rightarrow \tau\tau$ events selected in data, compared to MC expectations. The $Z/\gamma^* \rightarrow \tau\tau$ events are selected in the decay channel of muon and τ_h , as described in Section 7.1.1. The τ_h are required to pass the medium working point of the MVA-based τ_h isolation discriminant. The mass of τ_h candidates reconstructed in simulated $Z/\gamma^* \rightarrow \tau\tau$ events is corrected for small data/MC differences in the τ_h energy scale, discussed in Section 9. The electroweak background is dominated by W +jets production, with minor contributions arising from single top quark and diboson production. The shaded uncertainty band represents the sum of systematic and statistical uncertainties on the MC simulation.

selections and an MVA approach. An overview of the discriminants, with their respective efficiencies and misidentification rates, is given in Table 2.

5.2.1 Cutoff-based discriminants

The isolation of τ_h candidates is computed by summing the scalar values of p_T of charged particles and photons with $p_T > 0.5$ GeV, reconstructed with the PF algorithm, within an isolation cone of size $\Delta R = 0.5$, centred on the τ_h direction. The effect of pileup is reduced by requiring the tracks associated to charged particles considered in the isolation sum to be compatible with originating from the production vertex of the τ_h candidate within a distance of $\Delta z < 0.2$ cm and $\Delta r < 0.03$ cm. Charged hadrons used to form the τ_h candidate are excluded from the isolation sum, as are electrons and photons used to construct any of the strips. The effect of pileup on photon isolation is compensated on a statistical basis through the modified $\Delta\beta$ corrections:

$$I_\tau = \sum_{\text{charged}, \Delta z < 0.2 \text{ cm}} p_T + \max \left\{ 0, \sum_{\gamma} p_T - \Delta\beta \right\}, \quad (4)$$

where the $\Delta\beta$ are computed by summing the p_T of charged particles that are within a cone of size $\Delta R = 0.8$ around the τ_h direction, and are associated to tracks that have a distance to the τ_h production vertex of more than 0.2 cm in z . The sum is scaled by a factor 0.46, chosen to make the τ_h identification efficiency insensitive to pileup:

$$\Delta\beta = 0.46 \sum_{\text{charged}, \Delta z > 0.2 \text{ cm}} p_T. \quad (5)$$

Loose, medium, and tight working points (WP) are defined for the cutoff-based τ_h isolation discriminants by requiring the p_T sum defined by Eq. (4) not to exceed thresholds of 2.0, 1.0, and 0.8 GeV, respectively.

5.2.2 MVA-based discriminants

In order to minimize the jet $\rightarrow \tau_h$ background, the MVA-based τ_h identification discriminant utilizes the transverse impact parameter of the “leading” (highest p_T) track of the τ_h candidate, defined as the distance of closest approach in the transverse plane of the track to the τ_h production vertex. It also uses, for τ_h candidates reconstructed in the $h^\pm h^\mp h^\pm$ decay mode, the distance between the τ production point and the decay vertex. A BDT is used to discriminate τ_h decays (“signal”) from quark and gluon jets (“background”). The variables used as inputs to the BDT are:

1. The charged- and neutral-particle isolation sums defined in Eq. (4) as separate inputs.
2. The reconstructed τ_h decay mode, represented by an integer that takes the value of 0 for τ_h candidates reconstructed in the h^\pm decay mode, as 1 and 2 for candidates reconstructed in the $h^\pm \pi^0$ and $h^\pm \pi^0 \pi^0$ decay modes, respectively, and 10 for candidates reconstructed in the $h^\pm h^\mp h^\pm$ decay mode.
3. The transverse impact parameter d_0 of the leading track of the τ_h candidate, and its value divided by its uncertainty, which corresponds to its significance d_0/σ_{d_0} .
4. The distance between the τ production and decay vertices, $|\vec{r}_{SV} - \vec{r}_{PV}|$, and its significance, $|\vec{r}_{SV} - \vec{r}_{PV}|/\sigma_{|\vec{r}_{SV} - \vec{r}_{PV}|}$, and a flag indicating whether a decay vertex has successfully been reconstructed for a given τ_h candidate. The positions of the vertices, \vec{r}_{SV} and \vec{r}_{PV} , are reconstructed using the adaptive vertex fitter algorithm [48].

The position of the primary event vertex is refitted after excluding the tracks associated with the τ_h candidate. The discrimination power of individual input variables is illustrated in Fig. 4.

The inputs are complemented by the p_T and η of the τ_h candidate and by the $\Delta\beta$ correction defined in Eqs. (4) and (5). The purpose of the p_T and η variables is to parameterize possible dependences of the other input variables on p_T and η . The events used for the training of the BDT are reweighted such that the two-dimensional p_T and η distribution of the τ_h candidates for signal and background are identical, which makes the MVA result independent of event kinematics. The $\Delta\beta$ correction parameterizes the dependence on pileup, in particular, the p_T sum of the neutral particles.

The BDT is trained on event samples produced using MC simulation. Samples of $Z/\gamma^* \rightarrow \tau\tau$, $H \rightarrow \tau\tau$, $Z' \rightarrow \tau\tau$, and $W' \rightarrow \tau\bar{\nu}_\tau$ events are used for the “signal” category. Reconstructed τ_h candidates are required to match τ_h decays within $\Delta R < 0.3$ at the generator level. Multi-jet and W +jets events are used for the “background” category. The τ_h candidates that match leptons originating from the W boson decays are excluded from the training. The samples contain $\approx 10^7$ events in total, and cover the range 20–2000 GeV in τ_h candidate p_T . Half of the available events are used for training, the other half for evaluating the MVA performance, and conducting overtraining checks. The distribution in MVA output is shown in Fig. 5.

Different working points, corresponding to different τ_h identification efficiencies and jet $\rightarrow \tau_h$ misidentification rates, are defined by changing the selections on the MVA output. The thresholds are adjusted as function of the p_T of the τ_h candidate, such that the τ_h identification efficiency for each WP is constant as function of p_T .

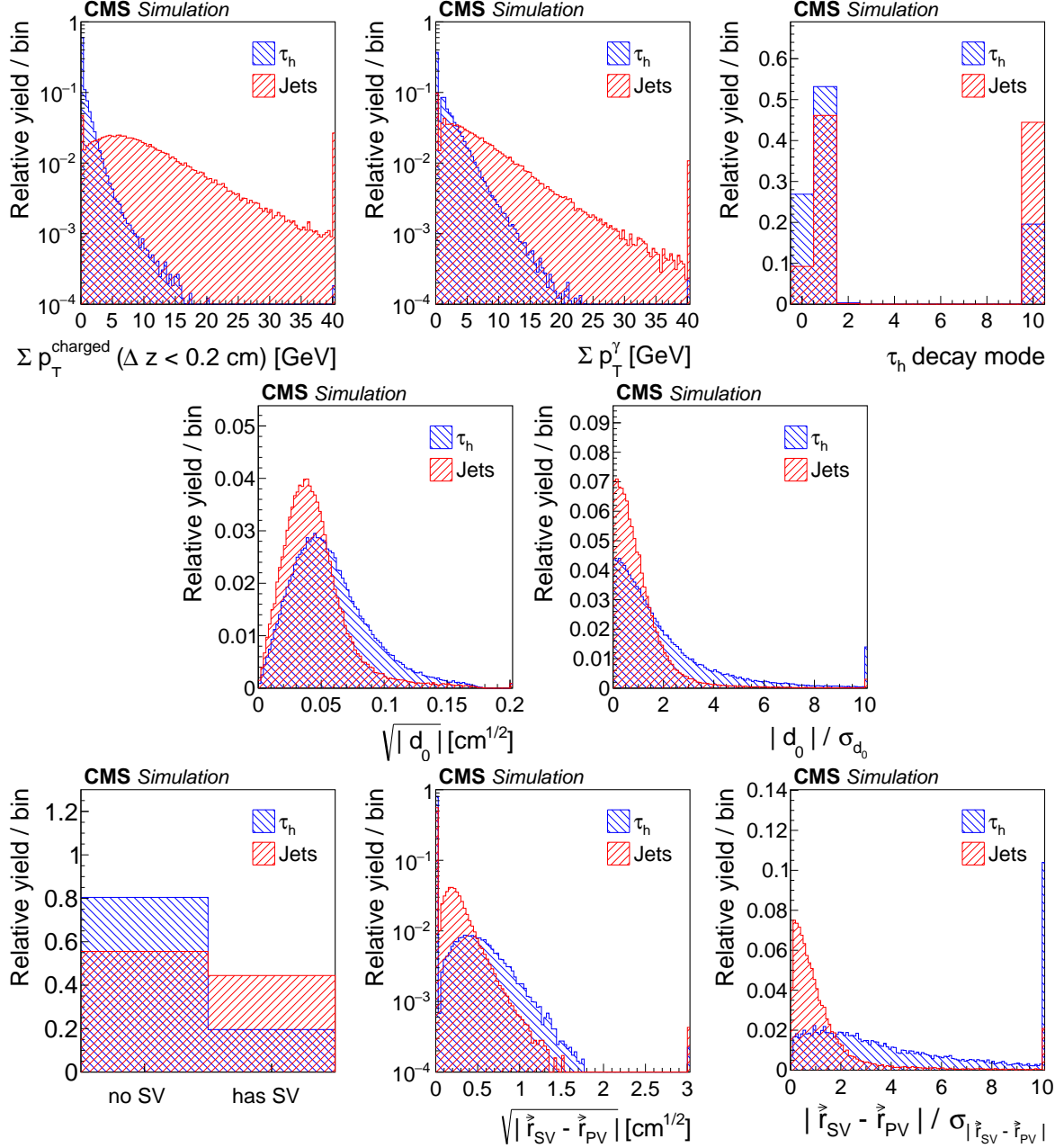


Figure 4: Distributions, normalized to unity, in observables used as input variables to the MVA-based isolation discriminant, for hadronic τ decays in simulated $Z/\gamma^* \rightarrow \tau\tau$ (blue), and jets in simulated W +jets (red) events. The τ_h candidates must have $p_T > 20$ GeV and $|\eta| < 2.3$, and be reconstructed in one of the decay modes h^\pm , $h^\pm\pi^0$, $h^\pm\pi^0\pi^0$, or $h^\pm h^\mp h^\pm$. In the plot of the τ_h decay mode on the upper right, an entry at 0 represents the decay mode h^\pm , 1 and 2 represent the decay modes $h^\pm\pi^0$ and $h^\pm\pi^0\pi^0$, respectively, and entry 10 represents the $h^\pm h^\mp h^\pm$ decay mode.

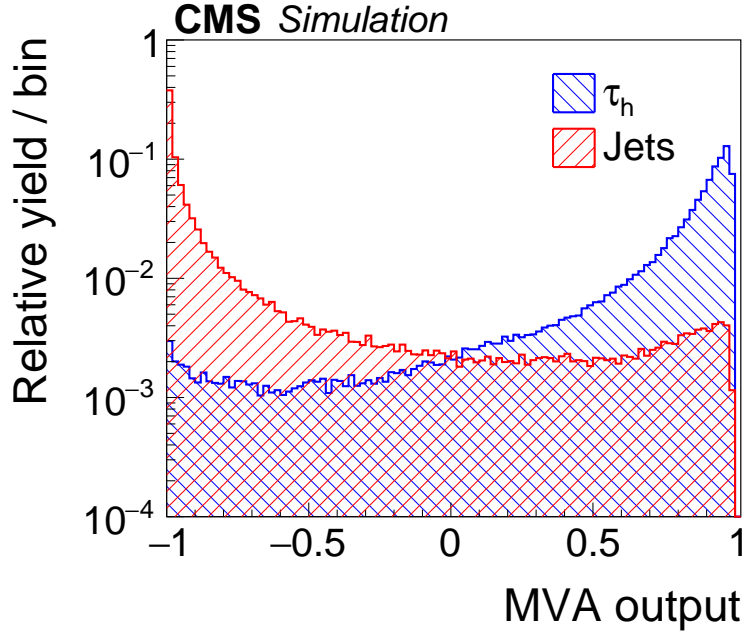


Figure 5: Distribution of MVA output for the τ_h identification discriminant that includes life-time information for hadronic τ decays in simulated $Z/\gamma^* \rightarrow \tau\tau$ (blue), and jets in simulated W +jets (red) events.

5.3 Discriminants against electrons and muons

Electrons and muons have a sizeable probability to get reconstructed in the h^\pm decay mode. Electrons radiating a bremsstrahlung photon that subsequently converts may also get reconstructed in the $h^\pm\pi^0$ decay mode. In particular, electrons and muons originating from decays of W and Z bosons, which are produced with cross sections of ≈ 100 nb at the LHC at $\sqrt{s} = 8$ TeV, have a high chance to pass isolation-based τ_h identification criteria. Dedicated discriminants have been developed to separate τ_h from electrons and muons. The separation of τ_h from electrons is based on an MVA approach. A cutoff-based and an MVA based discriminant are used to separate τ_h from muons.

5.3.1 MVA-based electron discriminant

A BDT discriminant is trained to separate τ_h decays from electrons. The algorithm utilizes observables that quantify the distribution in energy depositions in the ECAL, in combination with observables sensitive to the amount of bremsstrahlung emitted along the leading track, and observables sensitive to the overall particle multiplicity, to distinguish electromagnetic from hadronic showers. More specifically, the following variables are used as inputs to the BDT:

1. Electromagnetic energy fraction, $E_{\text{ECAL}}/(E_{\text{ECAL}} + E_{\text{HCAL}})$, defined as the ratio of energy depositions in the ECAL to the sum of energy in the ECAL and HCAL, associated with the charged particles and photons that constitute the τ_h candidate.
2. E_{ECAL}/p and E_{HCAL}/p , defined as ratios of ECAL and HCAL energies relative to the momentum of the leading charged-particle track of the τ_h candidate.
3. $\sqrt{\sum(\Delta\eta)^2 p_T^\gamma}$ and $\sqrt{\sum(\Delta\phi)^2 p_T^\gamma}$, the respective p_T -weighted (in GeV) root-mean-square distances in η and ϕ between the photons in any strip and the leading charged particle.

4. $\sum E_\gamma / E_\tau$, the fraction of τ_h energy carried by photons.
5. $F_{\text{brem}} = (p_{\text{in}} - p_{\text{out}}) / p_{\text{in}}$, where p_{in} and p_{out} are measured by the curvature of the leading track, reconstructed using the GSF algorithm, at the innermost and outermost positions of the tracker.
6. $(E_e + \sum E_\gamma) / p_{\text{in}}$, the ratio between the total ECAL energy and the inner track momentum. The quantities E_e and $\sum E_\gamma$ represent the energies of the electron cluster and of bremsstrahlung photons, respectively. $\sum E_\gamma$ is reconstructed by summing the energy depositions in ECAL clusters located along the tangent to the GSF track.
7. $\sum E_\gamma / (p_{\text{in}} - p_{\text{out}})$, the ratio of energies of the bremsstrahlung photons measured in the ECAL and in the tracker.
8. m_{τ_h} , the mass of the τ_h candidate.
9. $(N_{\text{hits}}^{\text{GSF}} - N_{\text{hits}}^{\text{KF}}) / (N_{\text{hits}}^{\text{GSF}} + N_{\text{hits}}^{\text{KF}})$, with $N_{\text{hits}}^{\text{GSF}}$ and $N_{\text{hits}}^{\text{KF}}$ representing, respectively, the number of hits in the silicon pixel and strip tracking detector associated with the track reconstructed using, respectively, the GSF and Kalman filter (KF) track reconstruction algorithms. The KF algorithm is the standard algorithm for track reconstruction at CMS [21]. The number of hits associated with GSF and KF track is sensitive to the emission of hard bremsstrahlung photons.
10. χ^2 per degree-of-freedom (DoF) of the GSF track.

The discriminating power of these variables is illustrated in Fig. 6.

The inputs are complemented by the p_T and η of the τ_h candidate, the p_T , σ_{p_T} / p_T , and η of the GSF track, and by the distances in η and in ϕ of the GSF track to the nearest boundary between ECAL modules. These variables are used to parameterize the dependence of the other input variables. Electrons entering the boundaries between ECAL modules are more difficult to discriminate from τ_h decays, as their electromagnetic showers are often not well reconstructed, and the probability to reach the hadron calorimeter increases in these regions.

Samples of simulated $Z/\gamma^* \rightarrow \tau\tau$, $Z/\gamma^* \rightarrow ee$, $W \rightarrow \tau\bar{\nu}_\tau$, $W \rightarrow e\bar{\nu}_e$, $t\bar{t}$, $H \rightarrow \tau\tau$, $Z' \rightarrow \tau\tau$, $Z' \rightarrow ee$, $W' \rightarrow \tau\bar{\nu}_\tau$, and $W' \rightarrow e\bar{\nu}_e$ events have been used to train the BDT. Reconstructed τ_h candidates are considered as signal or background when they are matched, respectively, within $\Delta R < 0.3$ to a hadronic τ decay or to an electron at the generator level.

Different WP are defined by changing the cutoff on the BDT output. The τ_h candidates reconstructed in the uninstrumented region between ECAL barrel and endcap, $1.45 < \eta < 1.56$, are rejected in all cases.

5.3.2 Cutoff-based muon discriminant

The cutoff-based discriminant against muons vetoes τ_h candidates when signals in the muon system are found near the τ_h direction. Two working points are provided:

1. **Loose:** τ_h candidates pass the cutoff on this discriminant, except when track segments are found in at least two muon stations within a cone of size $\Delta R = 0.3$ centred on the τ_h direction, or when the sum of the energies in the ECAL and HCAL corresponds to < 0.2 of the momentum of the leading track of the τ_h candidate.

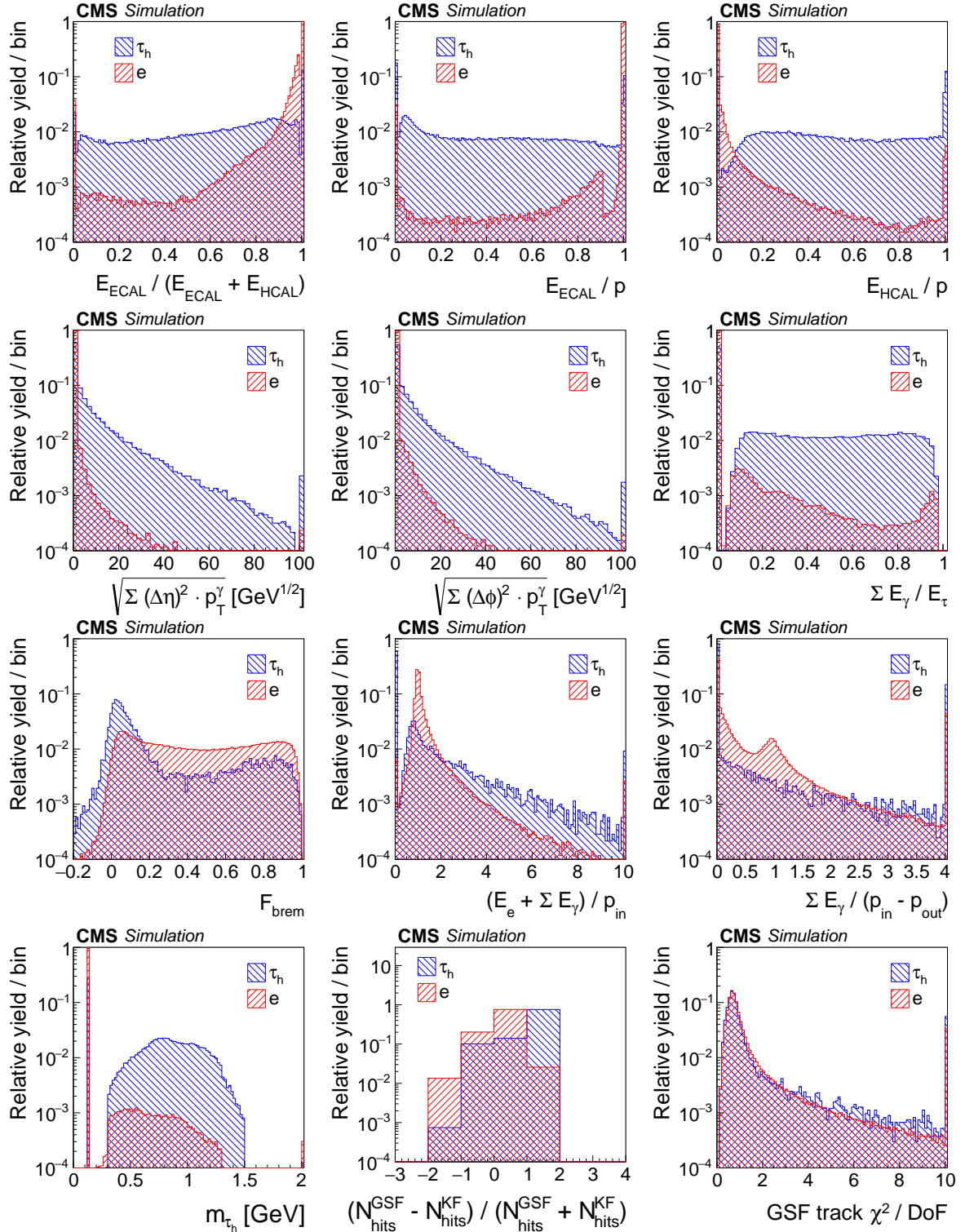


Figure 6: Distributions, normalized to unity, in observables that are used as inputs to the MVA-based electron discriminant, for hadronic τ decays in simulated $Z/\gamma^* \rightarrow \tau\tau$ (blue), and electrons in simulated $Z/\gamma^* \rightarrow ee$ (red) events. The τ_h candidates must have $p_T > 20 \text{ GeV}$ and $|\eta| < 2.3$, and be reconstructed in one of the decay modes h^\pm , $h^\pm\pi^0$, $h^\pm\pi^0\pi^0$, or $h^\pm h^\mp h^\pm$. The rightmost bin of the distributions is used as overflow bin.

2. **Tight:** τ_h candidates pass this discriminant restriction when they pass the loose WP, and no hits are present within a cone of $\Delta R = 0.3$ around the τ_h direction in the CSC, DT, and RPC detectors located in the two outermost muon stations.

5.3.3 MVA-based muon discriminant

A multivariate BDT discriminant has also been trained to separate τ_h decays from muons. The following variables are used as BDT inputs:

1. The calorimeter energy associated with the leading charged particle of the τ_h candidate, with separate energy sums computed for ECAL and HCAL.
2. The calorimeter energy associated in the PF algorithm with any charged particle or photon constituting the τ_h candidate, again, with separate energy sums computed for ECAL and HCAL.
3. The fraction of p_T carried by the charged particle with highest p_T .
4. The number of track segments in the muon system reconstructed within a cone of size $\Delta R = 0.5$ around the τ_h direction.
5. The number of muon stations with at least one hit detected within a cone of size $\Delta R = 0.5$ centred on the τ_h direction, computed separately for DT, CSC, and RPC detectors.

The inputs are complemented by the η of the τ_h candidate, to parameterize the dependence of the input variables on the DT, CSC, and RPC muon acceptance, and on the path length of muons traversed in the ECAL and HCAL.

The BDT is trained using samples of simulated $Z/\gamma^* \rightarrow \tau\tau$, $Z/\gamma^* \rightarrow \mu\mu$, $W \rightarrow \tau\bar{\nu}_\tau$, $W \rightarrow \mu\bar{\nu}_\mu$, $t\bar{t}$, $H \rightarrow \tau\tau$, $Z' \rightarrow \tau\tau$, $Z' \rightarrow \mu\mu$, $W' \rightarrow \tau\bar{\nu}_\tau$, and $W' \rightarrow \mu\bar{\nu}_\mu$ events. Reconstructed τ_h candidates are considered as signal or background when they are matched, respectively, to generator-level hadronic tau decays or muons within $\Delta R < 0.3$.

Different WP are defined by changing the cutoff on the MVA output.

6 Expected performance

The expected performance of the HPS τ_h identification algorithm is studied in terms of decay modes and energy reconstruction, τ_h identification efficiency, and misidentification rates for jets, electrons, and muons using simulated samples of $Z/\gamma^* \rightarrow \ell\ell$ ($\ell = e, \mu, \tau$), $Z' \rightarrow \tau\tau$, W +jets, and multijet events.

Tau identification efficiencies and misidentification rates in MC simulated events, averaged over p_T and η , for pileup conditions characteristic of the data-taking period, are given in Table 2.

6.1 Decay modes and energy reconstruction

The τ_h decay mode reconstruction is studied in simulated $Z/\gamma^* \rightarrow \tau\tau$ events. The performance is quantified by the correlation between reconstructed and generator-level τ_h decay modes. Figure 7 demonstrates that the true τ decay mode is reconstructed in about 90% of the cases, irrespective of pileup conditions, represented by the number of reconstructed vertices (N_{vtx}). The few per cent decrease in the fraction of τ leptons decaying to a single charged hadron that

Table 2: Expected efficiencies and misidentification rates of various τ_h identification discriminants, averaged over p_T and η , for pileup conditions characteristic of the LHC Run 1 data-taking period. The DM-finding criterion refers to the requirement that the τ_h candidate be reconstructed in one of the decay modes h^\pm , $h^\pm\pi^0$, $h^\pm\pi^0\pi^0$, or $h^\pm h^\mp h^\pm$ (cf. Section 5.1).

DM-finding and τ_h isolation discriminants				
WP	Efficiency		Jet $\rightarrow \tau_h$ misidentification rate	
	$Z/\gamma^* \rightarrow \tau\tau$	$Z'(2.5\text{ TeV}) \rightarrow \tau\tau$	W+jets	Multijet
Cutoff-based				
Loose	49.0%	58.9%	9.09×10^{-3}	3.86×10^{-3}
Medium	40.8%	50.8%	5.13×10^{-3}	2.06×10^{-3}
Tight	38.1%	48.1%	4.38×10^{-3}	1.75×10^{-3}
MVA-based				
Very loose	55.9%	71.2%	1.29×10^{-2}	6.21×10^{-3}
Loose	50.7%	64.3%	7.38×10^{-3}	3.21×10^{-3}
Medium	39.6%	50.7%	3.32×10^{-3}	1.30×10^{-3}
Tight	27.3%	36.4%	1.56×10^{-3}	4.43×10^{-4}
Discriminant against electrons				
WP	Efficiency		$e \rightarrow \tau_h$ misidentification rate	
	$Z/\gamma^* \rightarrow \tau\tau$	$Z'(2.5\text{ TeV}) \rightarrow \tau\tau$	$Z/\gamma^* \rightarrow ee$	
Very loose	94.3%	89.6%	2.38×10^{-2}	
Loose	90.6%	81.5%	4.43×10^{-3}	
Medium	84.8%	73.2%	1.38×10^{-3}	
Tight	78.3%	65.1%	6.21×10^{-4}	
Very tight	72.1%	60.0%	3.54×10^{-4}	
Discriminant against muons				
WP	Efficiency		$\mu \rightarrow \tau_h$ misidentification rate	
	$Z/\gamma^* \rightarrow \tau\tau$	$Z'(2.5\text{ TeV}) \rightarrow \tau\tau$	$Z/\gamma^* \rightarrow \mu\mu$	
Cutoff-based				
Loose	99.3%	96.4%	1.77×10^{-3}	
Tight	99.1%	95.0%	7.74×10^{-4}	
MVA-based				
Loose	99.5%	99.4%	5.20×10^{-4}	
Medium	99.0%	98.8%	3.67×10^{-4}	
Tight	98.0%	97.7%	3.18×10^{-4}	

are reconstructed in the true decay mode is due to events in which particles from pileup deposit energy in the ECAL near the τ , causing the τ to be reconstructed in the $h^\pm\pi^0$ or $h^\pm\pi^0\pi^0$ decay modes.

The performance of energy reconstruction is studied in simulated $Z/\gamma^* \rightarrow \tau\tau$ and $Z' \rightarrow \tau\tau$ events, and quantified in terms of response and resolution, defined as the mean and standard deviation of the reconstructed momentum distribution relative to the generator-level momentum of the visible τ decay products. The distributions for τ_h decays in simulated $Z/\gamma^* \rightarrow \tau\tau$ and $Z' \rightarrow \tau\tau$ events are shown in Fig. 8. The average response is below 1.0, because of an asymmetry of the $\langle p_T^{\text{rec}}/p_T^{\text{gen}} \rangle$ distribution, where p_T^{rec} and p_T^{gen} refer, respectively, to the p_T of the reconstructed τ_h candidate and to the p_T of the vectorial momentum sum of the visible τ decay products at the generator level. The most probable value of the ratio $\langle p_T^{\text{rec}}/p_T^{\text{gen}} \rangle$ is close to 1.0. The effect of pileup on τ reconstruction is small.

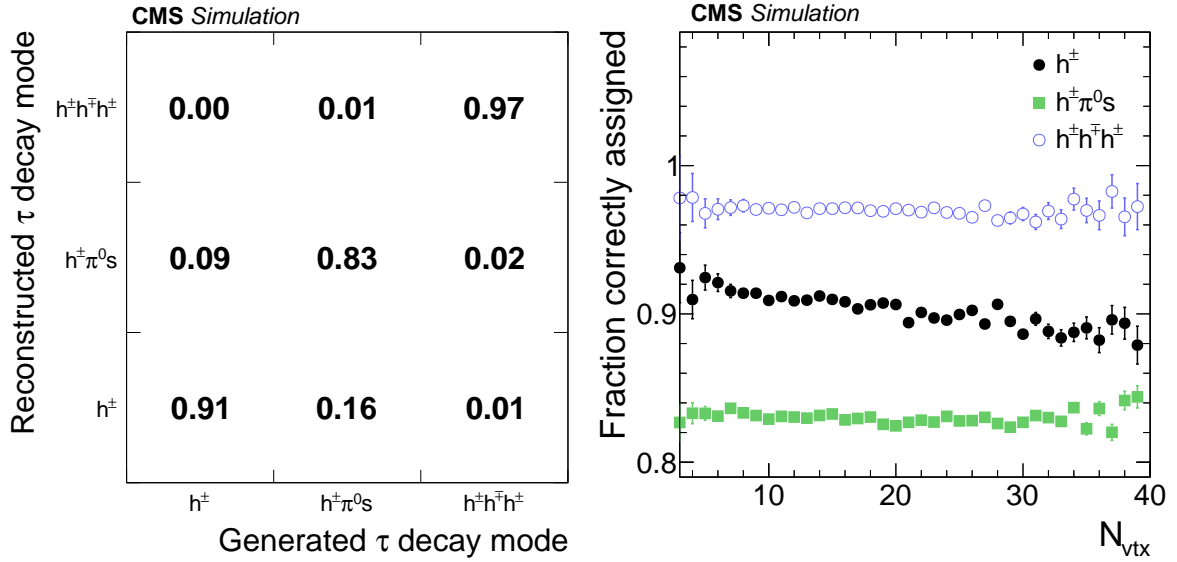


Figure 7: Left: Correlation between generated and reconstructed τ_h decay modes for τ_h decays in $Z/\gamma^* \rightarrow \tau\tau$ events, simulated for pileup conditions characteristic of the LHC Run 1 data-taking period. Right: Fraction of generated τ_h reconstructed in the correct decay mode as function of N_{vtx} . Reconstructed τ_h candidates are required to be matched to hadronic τ decays at the generator-level within $\Delta R < 0.3$, to be reconstructed in one of the decay modes h^\pm , $h^\pm\pi^0$, $h^\pm\pi^0\pi^0$, or $h^\pm h^\mp h^\pm$, and pass $p_T > 20$ GeV, $|\eta| < 2.3$, and the loose WP of the cutoff-based τ_h isolation discriminant.

6.2 The τ_h identification efficiency

The efficiency to pass the decay mode reconstruction and the different τ_h identification discriminants is determined for hadronic τ decays with visible decay products that satisfy the conditions $p_T > 20$ GeV and $|\eta| < 2.3$ at the generator level. More specifically, the efficiency is defined by the percentage of τ_h candidates that satisfy:

$$\varepsilon_\tau = \frac{p_T^{\text{rec}} > 20 \text{ GeV}, |\eta_{\text{rec}}| < 2.3, \text{ DM-finding, } \tau_h \text{ ID discriminant}}{p_T^{\text{gen}} > 20 \text{ GeV}, |\eta_{\text{gen}}| < 2.3}, \quad (6)$$

where η_{rec} and η_{gen} refer, respectively, to the η of the reconstructed τ_h candidate and to the η of the vectorial momentum sum of the visible τ decay products at the generator level. The DM-finding criterion refers to the requirement that the τ_h candidate be reconstructed in one

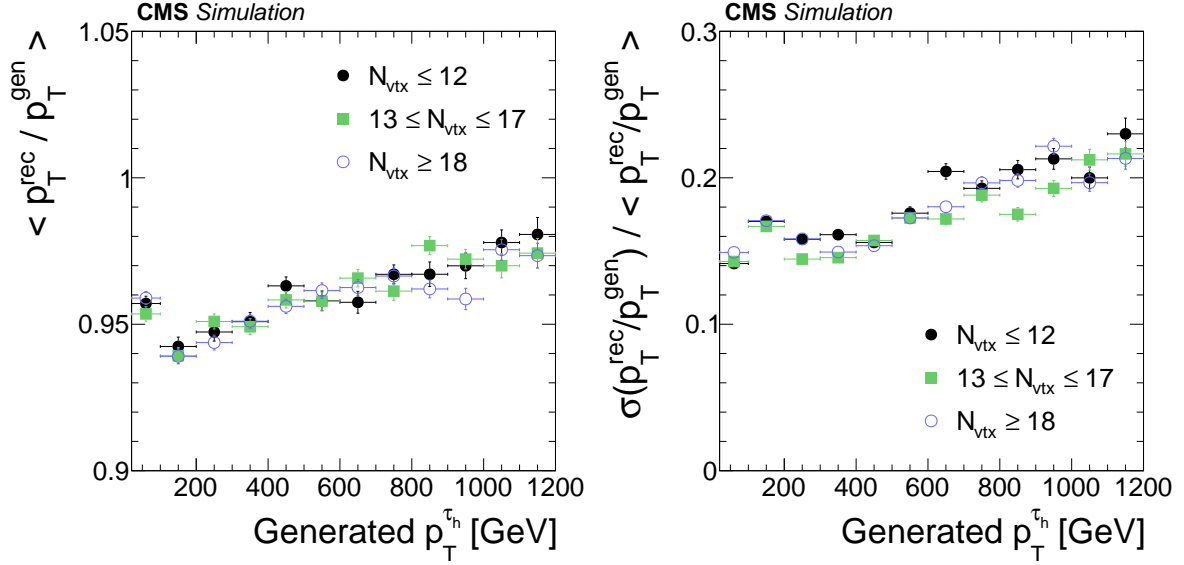


Figure 8: The τ_h energy response (left) and relative resolution (right) as function of generator-level visible τ p_T in simulated $Z' \rightarrow \tau\tau$ events for different pileup conditions: $N_{\text{vtx}} \leq 12$, $13 \leq N_{\text{vtx}} \leq 17$, and $N_{\text{vtx}} \geq 18$. Reconstructed τ_h candidates are required to be matched to hadronic τ decays at the generator-level within $\Delta R < 0.3$, to be reconstructed in one of the decay modes h^\pm , $h^\pm\pi^0$, $h^\pm\pi^0\pi^0$ or $h^\pm h^\mp h^\pm$, and to pass $p_T > 20$ GeV, $|\eta| < 2.3$, and the loose WP of the cutoff-based τ_h isolation discriminant.

of the decay modes h^\pm , $h^\pm\pi^0$, $h^\pm\pi^0\pi^0$, or $h^\pm h^\mp h^\pm$ (cf. Section 5.1), and τ_h ID refers to the τ_h identification discriminant used in the analysis. The p_T^{gen} and η_{gen} selection criteria in the denominator are also applied in the numerator. Only those τ_h candidates matched to generator-level hadronic τ decays within $\Delta R < 0.3$ are considered in the numerator.

The efficiencies of the discriminants against electrons and muons are determined for τ_h candidates matched to generator-level τ_h decays within $\Delta R < 0.3$, passing $p_T^{\text{rec}} > 20$ GeV, $|\eta_{\text{rec}}| < 2.3$, reconstructed in one of the decay modes h^\pm , $h^\pm\pi^0$, $h^\pm\pi^0\pi^0$, or $h^\pm h^\mp h^\pm$, and satisfying the loose WP of the cutoff-based τ_h isolation discriminant:

$$\varepsilon_\tau = \frac{\text{lepton discriminant}}{p_T^{\text{rec}} > 20 \text{ GeV}, |\eta_{\text{rec}}| < 2.3, \text{ DM-finding, loose cutoff-based isolation}}. \quad (7)$$

The selection criteria in the denominators of Eqs. (6) and (7) are also applied in the numerators.

The efficiency for τ_h decays to pass the cutoff-based and MVA-based τ_h identification discriminants are shown for simulated $Z/\gamma^* \rightarrow \tau\tau$ and $Z' \rightarrow \tau\tau$ events in Fig. 9.

The efficiencies are higher in $Z' \rightarrow \tau\tau$ than in SM $Z/\gamma^* \rightarrow \tau\tau$ events, as the τ leptons have larger p_T in the former case. The expected efficiencies of the isolation discriminants range between 40% and 70%, depending on whether tight or loose criteria are applied. The discrimination against electrons and against muons have respective efficiencies between 60% and 95%, and between 95% and 99%.

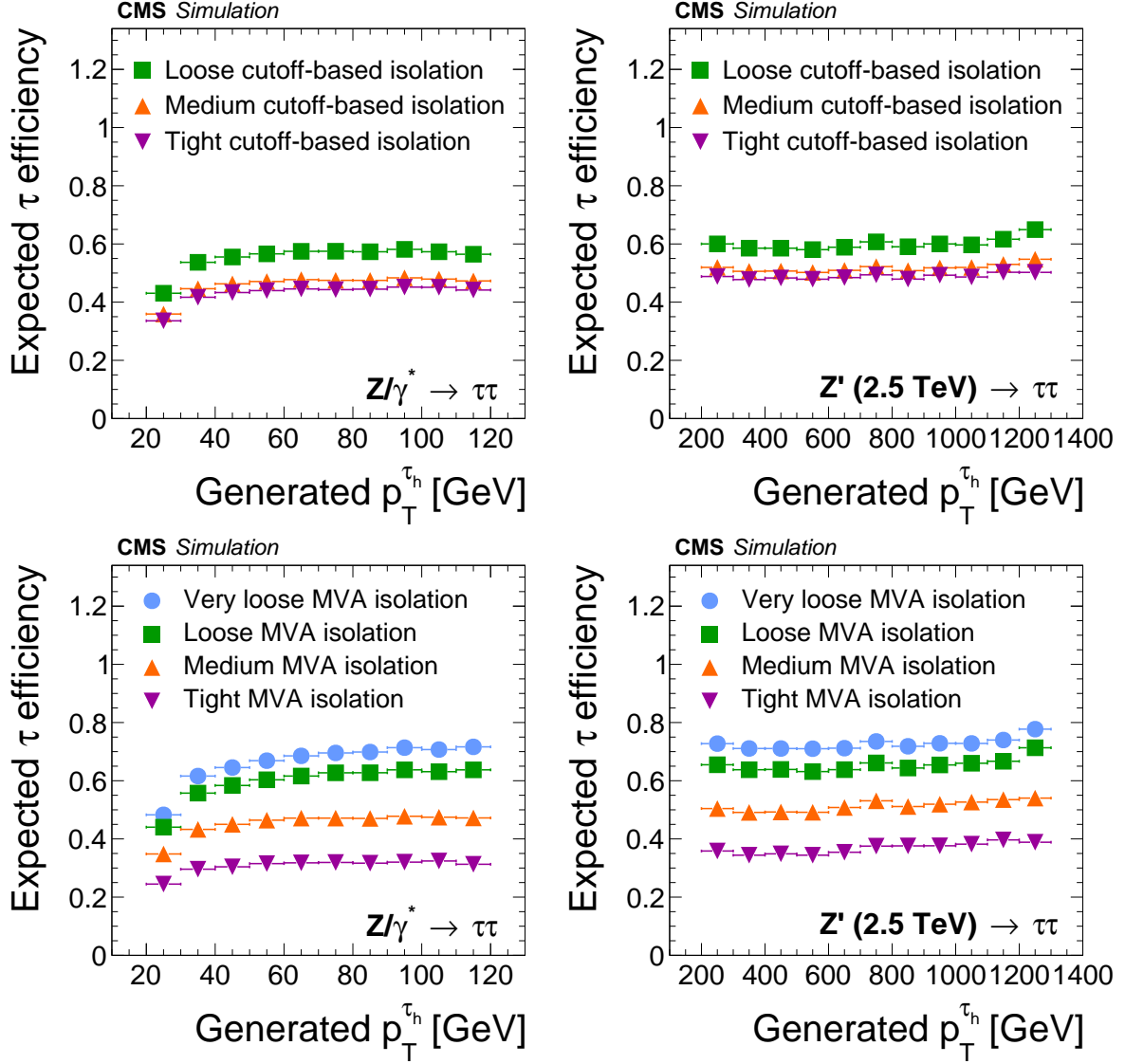


Figure 9: Efficiency for τ_h decays in simulated $Z/\gamma^* \rightarrow \tau\tau$ (left) and $Z' \rightarrow \tau\tau$ (right) events to be reconstructed in one of the decay modes h^\pm , $h^\pm\pi^0$, $h^\pm\pi^0\pi^0$, or $h^\pm h^\mp h^\pm$, to satisfy the conditions $p_T > 20 \text{ GeV}$ and $|\eta| < 2.3$, and to pass: the loose, medium and tight WP of the cutoff-based τ_h isolation discriminant (top) and the very loose, loose, medium and tight WP of the MVA-based tau isolation discriminant (bottom). The efficiency is shown as a function of the generator-level p_T of the visible τ decay products in τ_h decays that are within $|\eta| < 2.3$.

6.3 Misidentification rate for jets

The rate at which quark and gluon jets are reconstructed as τ_h candidates passing τ identification is computed for jets with $p_T^{\text{jet}} > 20 \text{ GeV}$ and $|\eta_{\text{jet}}| < 2.3$ as follows:

$$P_{\text{misid}} = \frac{p_T^{\tau_h} > 20 \text{ GeV}, |\eta_{\tau_h}| < 2.3, \text{ DM-finding, } \tau_h \text{ ID discriminant}}{p_T^{\text{jet}} > 20 \text{ GeV}, |\eta_{\text{jet}}| < 2.3}. \quad (8)$$

The p_T^{jet} and η_{jet} selection criteria of the denominator are also applied in the numerator. Note that p_T and η are different in the numerator and denominator, because p_T^{jet} and η_{jet} are computed by summing the momenta of all the particle constituents of the jet, while $p_T^{\tau_h}$ and η_{τ_h} refer to only the charged particles and photons included in the decay mode reconstruction of the τ_h candidate. Besides, jet energies are calibrated [51] and corrected for pileup effects [52, 53], whereas no energy calibration or pileup correction is applied to τ_h candidates.

The rates of $\text{jet} \rightarrow \tau_h$ misidentification range from a few 10^{-4} to 10^{-2} . They differ for W +jets and multijet events, because of the different fractions of quark and gluon jets in the two samples, and because of differences in jet p_T spectra, which are relevant due to the dependence of the $\text{jet} \rightarrow \tau_h$ misidentification rates on jet p_T (cf. Section 10).

The MVA-based τ_h identification discriminants that include lifetime information reduce the $\text{jet} \rightarrow \tau_h$ misidentification rate by about 40% relative to cutoff-based discriminants, while the τ_h identification efficiencies are very similar.

6.4 Misidentification rate for electrons and muons

The misidentification rates for $e \rightarrow \tau_h$ and $\mu \rightarrow \tau_h$ are determined for electrons and muons with $p_T^\ell > 20 \text{ GeV}$ and $|\eta_\ell| < 2.3$, and can be written as follows:

$$P_{\text{misid}} = \frac{p_T^{\tau_h} > 20 \text{ GeV}, |\eta_{\tau_h}| < 2.3, \text{ DM-finding, loose cutoff-based isolation, lepton discriminant}}{p_T^\ell > 20 \text{ GeV}, |\eta_\ell| < 2.3}. \quad (9)$$

Only τ_h candidates reconstructed within $\Delta R < 0.3$ of a generator-level electron or muon trajectory are considered for the numerator. The p_T^ℓ and η_ℓ symbols refer to the generator-level p_T and η of the electron or muon.

Typical $e \rightarrow \tau_h$ misidentification rates range from a few per mille to a few per cent. The rates for $\mu \rightarrow \tau_h$ misidentification are at or below the per mille level.

7 Validation with data

Different kinds of events are used to evaluate the τ_h reconstruction and identification in data. The τ_h identification efficiency and energy scale are validated using $Z/\gamma^* \rightarrow \tau\tau$ events. The efficiency to reconstruct and identify τ_h of higher p_T in more dense hadronic environments is measured using $t\bar{t}$ events. Samples of W +jets and multijet events are used to validate the rates with which quark and gluon jets are misidentified as τ_h candidates. The misidentification rates for electrons and muons are measured using $Z/\gamma^* \rightarrow ee$ and $Z/\gamma^* \rightarrow \mu\mu$ events.

The selection of event samples is described in Section 7.1. Systematic uncertainties relevant to the validation of the τ_h reconstruction and identification are detailed in Section 7.2. The measurement of τ_h identification efficiency, as well as of the rates at which electrons and muons are misidentified as τ_h candidates, is based on determining the yield of signal and background

processes, for which we use fits of simulated distributions (templates) to data, as described in Section 7.3.

7.1 Event selection

7.1.1 $Z/\gamma^* \rightarrow \tau\tau$ events

The sample of $Z/\gamma^* \rightarrow \tau\tau$ events is selected in decay channels of τ leptons to muon and τ_h final states. Except for extracting the τ_h identification efficiency, $Z/\gamma^* \rightarrow \tau\tau \rightarrow \mu\tau_h$ events are recorded using a trigger that demands the presence of a muon and τ_h [9]. The events used for the τ_h identification efficiency measurement are recorded using a single-muon trigger [46], to avoid potential bias that may arise from requiring a τ_h at the trigger level. The reconstructed muon is required to satisfy the conditions $p_T > 20$ GeV and $|\eta| < 2.1$, to pass tight identification criteria, and to be isolated relative to other particles in the event by $I_\mu < 0.10p_T^\mu$, computed according to Eq. (1). The τ_h candidates are required to be reconstructed in one of the decay modes described in Section 5.1, to satisfy the conditions $p_T > 20$ GeV and $|\eta| < 2.3$, and to pass the loose WP of the cutoff-based τ_h isolation discriminant, the tight WP of the cutoff-based discriminant against muons, and the loose WP of the discriminant against electrons. The muon and τ_h candidate are required to be compatible with originating from the primary collision vertex and be of opposite charge. In case multiple combinations of muon and τ_h exist in an event, the combination with the highest sum in scalar p_T is chosen. Background arising from W +jets production is removed by requiring the transverse mass computed in Eq. (3) to satisfy the condition $m_T < 40$ GeV. Events containing a second muon of $p_T > 15$ GeV and $|\eta_\mu| < 2.4$, passing loose identification and isolation criteria, are rejected to suppress $Z/\gamma^* \rightarrow \mu\mu$ Drell–Yan (DY) background.

The transverse impact parameter d_0 and the distance $|\vec{r}_{SV} - \vec{r}_{PV}|$ between the τ production and decay vertices in selected $Z/\gamma^* \rightarrow \tau\tau$ events are shown in Fig. 10. The normalization of the $Z/\gamma^* \rightarrow \tau\tau \rightarrow \mu\tau_h$ signal and of background processes is determined through a template fit to the data, as described in Section 7.3, using the visible mass of the muon and τ_h (m_{vis}) as observable in the fit. Separate fits are performed for events with τ_h candidates containing one and three charged particles. The fitted m_{vis} spectra are also shown in Fig. 10. The shaded areas represent the sum of statistical uncertainties of the MC samples and systematic uncertainties, added in quadrature, as discussed in Section 7.2. All distributions agree well with their respective MC simulations.

7.1.2 $t\bar{t}$ events

A sample of $t\bar{t}$ events is also selected in the $\mu\tau_h$ channel. The $t\bar{t} \rightarrow b\bar{b}\mu\tau_h$ events are required to pass a single-muon trigger and to contain a muon with $p_T > 25$ GeV and $|\eta| < 2.1$. The muon is required to pass tight identification criteria and to be isolated at the level of $I_\mu < 0.10p_T^\mu$. The τ_h candidate is required to be reconstructed in one of the decay modes described in Section 5.1, to satisfy the conditions $p_T > 20$ GeV and $|\eta| < 2.3$, to pass the loose WP of the cutoff-based τ_h isolation discriminant, and to be separated from the muon by $\Delta R > 0.5$. The event is also required to contain two jets of $p_T > 30$ GeV and $|\eta| < 2.5$, separated from the muon and the τ_h candidate by $\Delta R > 0.5$. At least one of the jets is required to meet the b tagging criteria [54, 55]. Background from $Z/\gamma^* \rightarrow \ell\ell$ ($\ell = e, \mu, \tau$) events is reduced by requiring $E_T^{\text{miss}} > 40$ GeV. Events containing an electron of $p_T > 15$ GeV and $|\eta| < 2.3$, or a second muon of $p_T > 10$ GeV and $|\eta| < 2.4$ that pass loose identification and isolation criteria are rejected.

The p_T distribution of τ_h candidates in the $t\bar{t}$ sample is compared to the $Z/\gamma^* \rightarrow \tau\tau$ sample in Fig. 11.

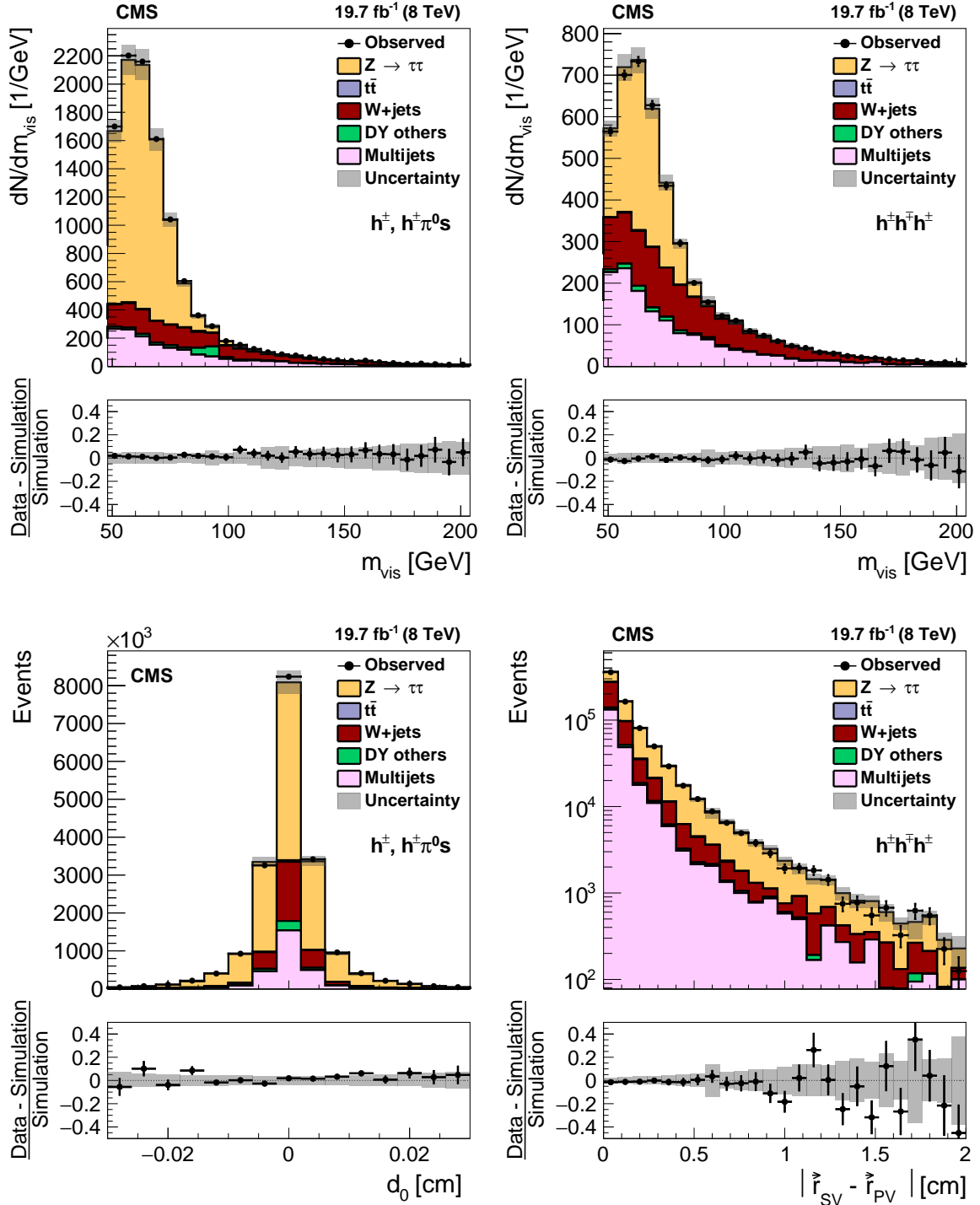


Figure 10: Top: Distribution in the visible mass of $Z/\gamma^* \rightarrow \tau\tau \rightarrow \mu\tau_h$ candidate events, in which the reconstructed τ_h candidate contains (upper left) a single or (upper right) three charged particles. Bottom: Distribution in (lower left) transverse impact parameter for events in which the τ_h candidate contains one charged particle and (lower right) in the distance between the τ production and decay vertex for events in which the τ_h candidate contains three charged particles. The $Z/\gamma^* \rightarrow \ell\ell$ ($\ell = e, \mu, \tau$) events, in which either the reconstructed muon or the reconstructed τ_h candidate are misidentified, are denoted by “DY others”.

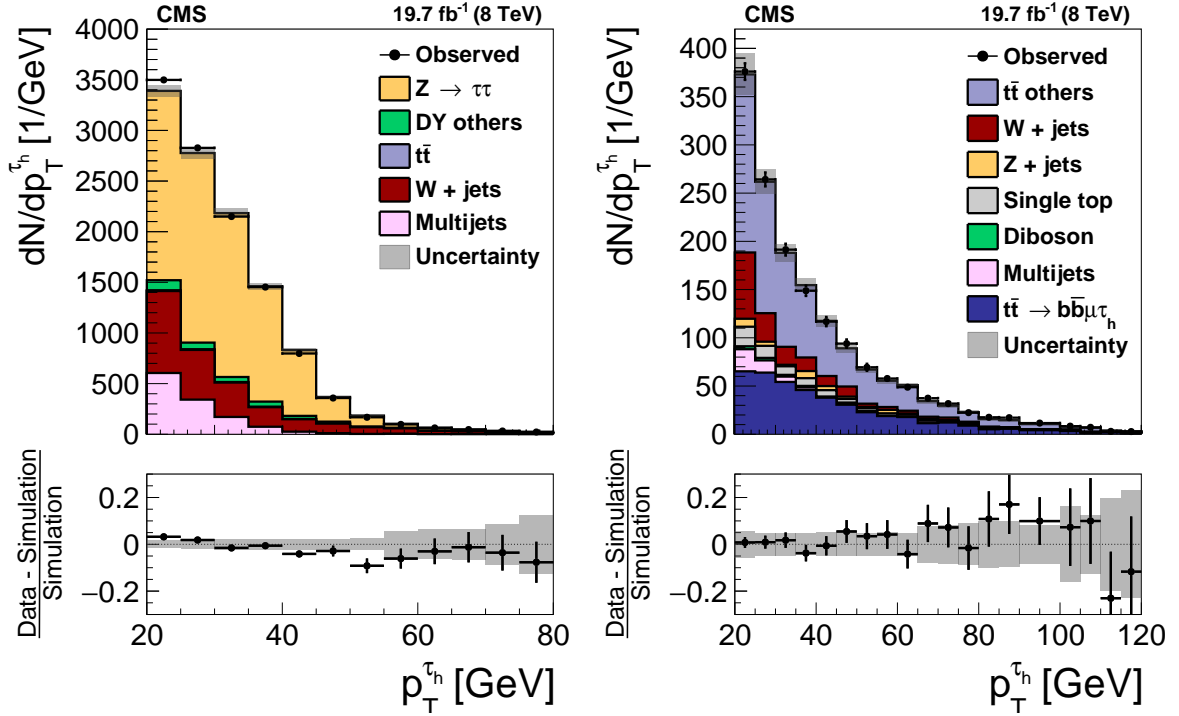


Figure 11: Distribution in the p_T of τ_h candidates in (left) $Z/\gamma^* \rightarrow \tau\tau$ and (right) $t\bar{t}$ events in data and in simulations. The $Z/\gamma^* \rightarrow \ell\ell$ ($\ell = e, \mu, \tau$) and $t\bar{t}$ events, in which either the reconstructed muon or the reconstructed τ_h candidate is misidentified, are denoted in the MC simulation by “DY others” and “ $t\bar{t}$ others”, respectively.

7.1.3 The W+jets sample

Events selected for the W+jets sample are required to pass the single-muon trigger and to contain a muon with $p_T > 25$ GeV and $|\eta| < 2.1$, passing tight identification and isolation criteria $I_\mu < 0.10p_T^\mu$. The muon and E_T^{miss} transverse mass, computed according to Eq. (3), is required to satisfy the condition $m_T > 50$ GeV. Selected W+jets candidate events are further required to contain at least one jet with $p_T > 20$ GeV and $|\eta| < 2.3$ that is separated from the muon by $\Delta R > 0.5$.

7.1.4 Multijet sample

The sample of multijet events is selected by requiring the events to pass a single-jet trigger with the p_T threshold of 320 GeV. The trigger was not prescaled during the whole data-taking period. The jet that passes the trigger is required to satisfy the conditions $p_T > 350$ GeV and $|\eta| < 2.5$. In order to measure the jet $\rightarrow \tau_h$ misidentification rate for jets unbiased by the trigger selection, the following procedure is used: If only one jet in the event passes the trigger requirement, that jet is excluded from the computation of the jet $\rightarrow \tau_h$ misidentification rate, and the other jets with $p_T > 20$ GeV and $|\eta| < 2.3$ in the event are used instead. When two or more jets in the event pass the trigger requirement, all jets with $p_T > 20$ GeV and $|\eta| < 2.3$ are included in the computation of the misidentification rate. Each jet is unbiased relative to the trigger selection, because the event would have been triggered by another jet regardless of the rest of the objects in the event.

The p_T distribution of jets considered for the computation of the jet $\rightarrow \tau_h$ misidentification rate is compared for W+jets and multijet samples in Fig. 12. The multijet sample provides more jets

with large p_T . Since the single-jet trigger used to select the multijet events requires at least one jet with p_T greater than 320 GeV, the sample is enriched with events containing high p_T jets that are likely recoiling against each other. This is the reason for the increase in the jet p_T spectrum in bin 300–400 GeV. The distributions observed in data agree with the MC expectation within uncertainties.

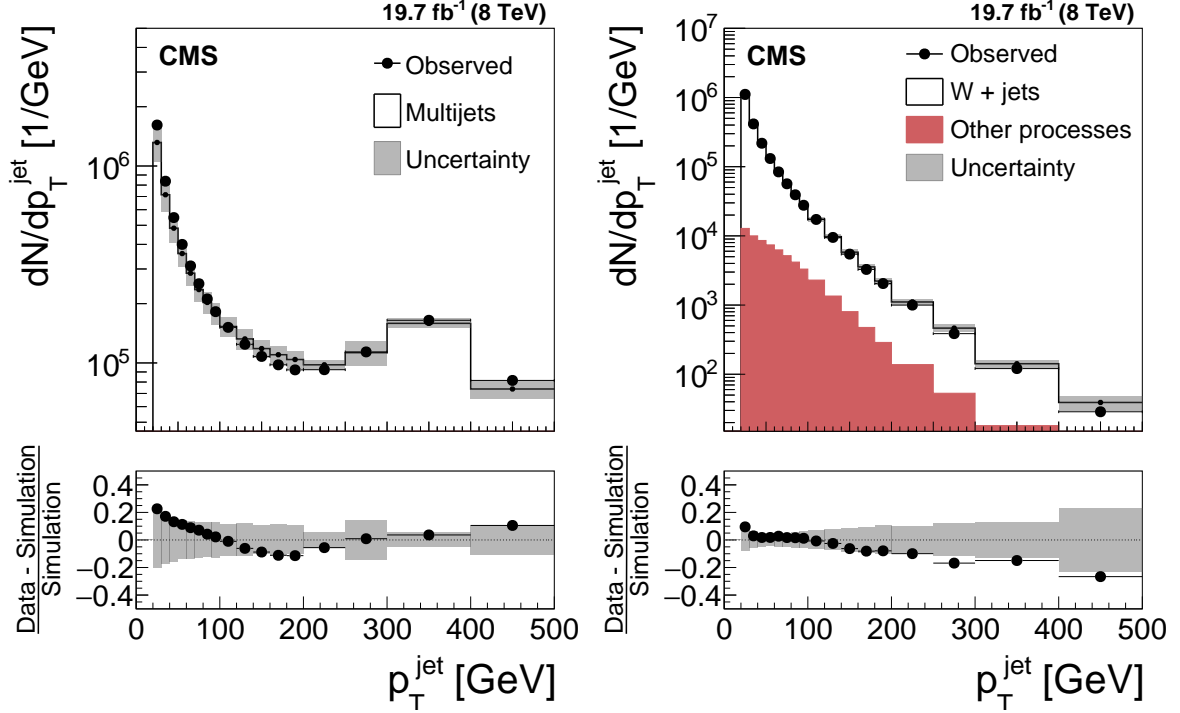


Figure 12: Jet p_T distribution in (left) multijet and (right) W+jets events observed in data, compared to the MC expectation. The uncertainty in the MC expectation is dominated by the uncertainty in the jet energy scale.

7.1.5 The $Z/\gamma^* \rightarrow ee$ and $Z/\gamma^* \rightarrow \mu\mu$ events

A high-purity sample of $Z/\gamma^* \rightarrow ee$ and $Z/\gamma^* \rightarrow \mu\mu$ events is selected by requiring candidate events to contain at least one well-identified and isolated electron or muon, referred to as the “tag”, and one τ_h candidate that passes loose preselection criteria, referred to as the “probe”. The $e \rightarrow \tau_h$ and $\mu \rightarrow \tau_h$ misidentification rates are given by the fraction of probes that pass the τ isolation criteria, as well as one of the dedicated discriminants for vetoing electrons or muons.

Tag electrons are required to pass a single-electron trigger, to satisfy the conditions $p_T > 30$ GeV and $|\eta| < 2.1$, pass tight electron identification criteria, and isolation, with $I_e < 0.10p_T^e$. Tag electrons reconstructed in the transition region between ECAL barrel and endcap, $1.46 < |\eta| < 1.56$, are discarded. Similarly, tag muons are required to pass a single-muon trigger, to satisfy the conditions $p_T > 25$ GeV and $|\eta| < 2.1$, pass tight muon identification criteria, and isolation, with $I_\mu < 0.10p_T^\mu$.

The probe is required to be reconstructed in one of the decay modes h^\pm , $h^\pm\pi^0$, $h^\pm\pi^0\pi^0$, or $h^\pm h^\mp h^\pm$, to satisfy the conditions $p_T > 20$ GeV and $|\eta| < 2.3$, and to be separated from the tag electron or muon by $\Delta R > 0.5$. The p_T and η requirements are applied on the values reconstructed using the HPS algorithm. When an event contains two electron or muon candidates that pass the tight selection criteria and qualify as tags, the event is selected if it contains at

least one combination of tag and probe leptons that are separated by $\Delta R > 0.5$. In this case, all combinations of tag and probe leptons separated by $\Delta R > 0.5$ are considered in the analysis.

The contribution of W +jets and $t\bar{t}$ backgrounds is reduced by requiring selected events to pass a requirement on the transverse mass of a tag electron or muon and E_T^{miss} , computed according to Eq. (3), respectively, of $m_T < 25 \text{ GeV}$ or $< 40 \text{ GeV}$. The contribution of the W +jets and $t\bar{t}$ background to the $Z/\gamma^* \rightarrow ee$ event sample is further suppressed by requiring $E_T^{\text{miss}} < 25 \text{ GeV}$.

7.2 Systematic uncertainties

Various imprecisely known or simulated effects can affect the level of agreement between data and simulation, irrespective of τ_h reconstruction and identification.

Electron and muon trigger, identification, and isolation efficiencies are measured using $Z/\gamma^* \rightarrow ee$ and $Z/\gamma^* \rightarrow \mu\mu$ events via the “tag-and-probe” method [56] with a precision of 2% [45, 46]. The uncertainty on the τ_h trigger efficiency is $\approx 3\%$.

The jet energy scale (JES) is validated using γ +jets, Z +jets, and dijet events [51]. The uncertainty in JES ranges from 1% to 10%, depending on p_T and η of the jet. The effect of uncertainty in energy resolution is found to be small and is not considered in this analysis. The efficiency for b jets to pass the medium WP of the CSV b tagging algorithm, and the mistag rates for light-quark and gluon jets are measured using $t\bar{t}$ and multijet events, and are in the ranges of 2–7% and 10–20%, respectively [54, 55].

The uncertainty in the integrated luminosity is 2.6% [57].

The theoretical uncertainties on the production cross sections are 5% for $Z/\gamma^* \rightarrow \ell\ell$ ($\ell = e, \mu, \tau$) DY production, and 15% for the $t\bar{t}$, diboson, and single top quark backgrounds. These include the uncertainties in PDF, estimated following the recommendation in Refs. [58, 59], and on the modelling of parton showers and of the underlying event.

The uncertainty in reweighting of simulated $t\bar{t}$ MC events, described in Section 3, is estimated by changing the weights from their nominal values to the square of the nominal values and to no reweighting.

The energy scale of electrons and muons is calibrated using $J/\Psi \rightarrow \ell\ell$, $Y \rightarrow \ell\ell$, and $Z \rightarrow \ell\ell$ ($\ell = e, \mu$) events, and is known to an uncertainty of 1% [45, 46].

The E_T^{miss} scale and resolution is known to a few per cent uncertainty from studies performed in $Z/\gamma^* \rightarrow \mu\mu$, $Z/\gamma^* \rightarrow ee$, and γ +jets events [37].

7.3 Template fits

The measurements of the τ_h identification efficiency, of the τ_h energy scale, and of the misidentification rates for electrons and muons are based on fitting the distribution of some observable in data with templates representing signal and background processes.

The likelihood function \mathcal{L} used in the fit is given by the product of Poisson probabilities to observe n_i events in each bin i of the distribution, given a number v_i events expected from signal and background processes in that bin:

$$\mathcal{L}(\mu, \theta) = \mathcal{P}(\text{data}|\mu, \theta) p(\tilde{\theta}|\theta) = \prod_i \frac{v_i^{n_i}}{n_i!} \exp(-v_i) p(\tilde{\theta}|\theta). \quad (10)$$

The number of expected events depends on the parameter of interest (POI) μ that we wish to measure, such as the τ_h identification efficiency, the energy scale, or the misidentification

rates for electrons and muons, and on the values of “nuisance” parameters θ that represent the systematic uncertainties discussed in the previous section.

The function $p(\tilde{\theta}|\theta)$ represents the probability to observe a value $\tilde{\theta}$ in an auxiliary measurement of the nuisance parameter, given that the true value is θ . The nuisance parameters are treated via the frequentist paradigm, as described in Refs. [60, 61]. Constraints on nuisance parameters that affect the normalization, but not the shape of the distribution are represented by log-normal probability density functions. Systematic uncertainties that affect the distribution as well as the normalization are incorporated into the likelihood fit via the technique detailed in Ref. [62] and constrained by Gaussian probability density functions.

Statistical uncertainties on the templates are accounted for by introducing additional nuisance parameters into the likelihood fit that provide uncorrelated single-bin fluctuations of the background expectation, following the method described in Ref. [63].

The value of μ that maximizes the likelihood function \mathcal{L} in Eq. (10) is taken as the best-fit estimate for the parameter of interest, referred to as μ^{obs} . The uncertainty in the measured value μ^{obs} is obtained by determining lower and upper bounds, μ^{min} and μ^{max} , for which the negative logarithm of the likelihood function exceeds the maximum by half a unit:

$$-\ln \mathcal{L}(\mu^{\text{min}}, \hat{\theta}_{\mu^{\text{min}}}) = -\ln \mathcal{L}(\mu^{\text{obs}}, \hat{\theta}_{\mu^{\text{obs}}}) + 0.5, \quad (11)$$

and similarly for μ^{max} . The nuisance parameters are profiled, that is, the values $\hat{\theta}_{\mu^{\text{min}}}$ and $\hat{\theta}_{\mu^{\text{max}}}$ are chosen such that the likelihood function reaches its local maximum, subject to the constraint that the POI value equals μ^{min} and μ^{max} , respectively.

The best-fit value of the POI that we obtain from one measurement, e.g. of the τ_h identification efficiency, can depend on the POI of another measurement, e.g. of the τ_h energy scale. Correlations of this kind are taken into account in the template fits by using the other POI measurements as nuisance parameters in the fit, with an uncertainty of 6% for the τ_h identification efficiency, 3% for the τ_h energy scale, 20% for the jet $\rightarrow \tau_h$ misidentification rate, and 30% for the $e \rightarrow \tau_h$ and $\mu \rightarrow \tau_h$ misidentification rates. The rate for $e \rightarrow \tau_h$ and $\mu \rightarrow \tau_h$ instrumental background in the MC simulation is corrected by the data-to-MC ratios given in Tables 6 and 7.

8 Measurement of the τ_h identification efficiency

The efficiency to reconstruct and identify τ_h decays is measured in $Z/\gamma^* \rightarrow \tau\tau \rightarrow \mu\tau_h$ and $t\bar{t} \rightarrow b\bar{b}\mu\tau_h$ events.

8.1 Tau identification efficiency in $Z/\gamma^* \rightarrow \tau\tau$ events

The measurement of the τ_h identification efficiency in $Z/\gamma^* \rightarrow \tau\tau$ events is based on selecting a sample of $Z/\gamma^* \rightarrow \tau\tau \rightarrow \mu\tau_h$ events without applying any τ_h identification criteria and determining the number of τ_h decays passing and failing the τ_h identification discriminant.

Following the event selection criteria described in Section 7.1.1, candidate events are required to pass a single-muon trigger, a higher p_T threshold for the muon with $p_T > 25 \text{ GeV}$, and, instead of requiring the event to contain a τ_h candidate that passes the τ_h identification discriminants, a loose τ_h candidate selection is applied as follows. Reconstructed jets are required to satisfy the conditions $p_T^{\text{jet}} > 20 \text{ GeV}$ and $|\eta_{\text{jet}}| < 2.3$, to be separated from the muon by $\Delta R > 0.5$, and to contain at least one track with $p_T > 5 \text{ GeV}$. The track of highest p_T within the jet is required to have a charge opposite to that of the muon, and to be compatible with

originating from the same vertex. When more than one jet passes the τ_h candidate selection criteria, the jet with largest p_T is used for this check.

In addition, tight kinematic criteria are applied to reduce contributions from background processes. The m_T criterion described in Section 7.1.1 is complemented by a requirement on a topological discriminant. The topological discriminant [64] is based on the projections:

$$P_\zeta = (\vec{p}_T^\mu + \vec{p}_T^{\tau_h} + \vec{p}_T^{\text{miss}}) \cdot \frac{\vec{\zeta}}{|\vec{\zeta}|} \quad \text{and} \quad P_\zeta^{\text{vis}} = (\vec{p}_T^\mu + \vec{p}_T^{\tau_h}) \cdot \frac{\vec{\zeta}}{|\vec{\zeta}|} \quad (12)$$

on the axis $\vec{\zeta}$, given by the bisector of the momenta in the transverse plane of the visible decay products of the two τ leptons. The discriminant utilizes the fact that the angle between the neutrinos produced in τ decays and the visible τ decay products is typically small, forcing the \vec{p}_T^{miss} vector in $Z/\gamma^* \rightarrow \tau\tau$ events to point in the direction of $\vec{p}_T^\mu + \vec{p}_T^{\tau_h}$, which is often not the case in W +jets and $t\bar{t}$ events. Selected events are required to satisfy the condition $P_\zeta - 1.85P_\zeta^{\text{vis}} > -15 \text{ GeV}$. This reduces the sum of backgrounds passing the m_T criterion by about a factor two. Background from $t\bar{t}$ production is reduced by vetoing events that contain jets of $p_T > 20 \text{ GeV}$ and $|\eta| < 2.5$ that pass b tagging criteria. The background contributions arising from WW , WZ , and ZZ production are suppressed by rejecting events that contain an electron with $p_T > 15 \text{ GeV}$ and $|\eta| < 2.4$ or a second muon with $p_T > 5 \text{ GeV}$ and $|\eta| < 2.4$. The electrons and muons considered for this veto are required to pass loose identification and isolation criteria.

The τ_h identification efficiency, ϵ_τ , is obtained through a simultaneous fit of the number of $Z/\gamma^* \rightarrow \tau\tau$ events, N_{pass}^τ and N_{fail}^τ , with τ_h candidates passing (“pass” region) and failing (“fail” region) the τ_h identification discriminant. The fit is performed as described in Section 7.3. The τ_h identification efficiency is taken as the parameter of interest μ in the fit. The number of $Z/\gamma^* \rightarrow \tau\tau$ events in the pass and fail regions as a function of μ are given by $N_{\text{pass}}^\tau = \mu N^{Z/\gamma^* \rightarrow \tau\tau}$ and $N_{\text{fail}}^\tau = (1 - \mu) N^{Z/\gamma^* \rightarrow \tau\tau}$, respectively. The normalization of the $Z/\gamma^* \rightarrow \tau\tau$ signal in the sum of pass and fail regions, $N^{Z/\gamma^* \rightarrow \tau\tau}$, as well as the templates for signal in both regions are obtained from the MC simulation. The systematic uncertainties discussed in Section 7.2 are represented by nuisance parameters in the fit. An additional nuisance parameter with an uncertainty of 3% is included in the fit to account for the uncertainty in the energy scale of the τ_h decays.

Contributions from background processes, especially to the fail region, are sizeable. The distributions for $Z/\gamma^* \rightarrow \mu\mu$, W +jets, $t\bar{t}$, single top quark, and diboson backgrounds are obtained from MC simulation. The uncertainty in the yield of $Z/\gamma^* \rightarrow \mu\mu$ and diboson ($t\bar{t}$ and single top quark) backgrounds is increased to 30% (20%), to account for the uncertainty in the rate with which muons (light-quark and gluon jets) are misidentified as τ_h decays.

The normalization of the W +jets background that is used as input to the fit is determined from data, using a control region defined by inverting the $m_T < 40 \text{ GeV}$ selection and requiring $m_T > 70 \text{ GeV}$ instead. The contributions of other backgrounds to this control region, referred to as high- m_T sideband, are subtracted, based on MC predictions, before extrapolating the event yield observed in the control region into the signal region. The extrapolation factor from $m_T > 70 \text{ GeV}$ to $m_T < 40 \text{ GeV}$ is obtained from MC simulation. The uncertainty in the W +jets background in the signal region, arising from the statistical uncertainty in the event yield in the control region, and from the uncertainty in the extrapolation factor, amounts to 15%, and is represented by a nuisance parameter in the fit.

The normalization and distribution of the multijet background is estimated from data, using

events in which the muon and loose τ_h candidate have the same charge. The extrapolation factor from the same-sign (SS) to the opposite-sign (OS) region is measured in events in which the muon fails the isolation criterion. The contributions from DY, $t\bar{t}$, single top quark, and diboson backgrounds to the OS and SS event samples with non-isolated muons, and to the SS event sample with isolated muons, are subtracted according to MC expectation. The number of W +jets events subtracted is determined using a control region in which the muon and the τ_h candidate have the same charge, and $m_T > 70$ GeV. The procedure provides an estimate of the multijet background in the signal region with an uncertainty of 10%.

Two alternative observables are used to perform the fit: (i) m_{vis} , the visible mass of the muon and the τ_h candidate, and (ii) N_{tracks} , the multiplicity of tracks within a cone of size $\Delta R < 0.5$ centred on the τ_h direction. The main results are obtained using m_{vis} . Fits of the N_{tracks} distribution are used to measure the τ_h identification efficiency as function of p_T and η of the τ_h candidate, and also as function of N_{vtx} .

Two other uncertainties are considered when N_{tracks} is used in the fit. The track reconstruction efficiency is measured with an uncertainty of 3.9% [21], and an uncertainty of 10% is attributed to the multiplicity of tracks associated with the τ_h candidates that are from $\text{jet} \rightarrow \tau_h$ misidentifications. The 10% represents the uncertainty on the multiplicity of charged hadrons produced in the hadronization of quarks and gluons into jets. The uncertainties in track reconstruction efficiency and hadronization affect the N_{tracks} distributions obtained from the MC simulation. We account for these uncertainties by producing N_{tracks} distributions with means shifted by $\pm 3.9\%$ and $\pm 10\%$. The shifted distributions are produced as follows: for a given event, we set $N_{\text{tracks}}^{\text{shifted}} = N_{\text{tracks}}$. We then iterate over the collection of reconstructed tracks. For each track, we sample from a uniform distribution, and when the random number thus selected is below the magnitude of the shift (either 0.039 or 0.10) we reduce or increase $N_{\text{tracks}}^{\text{shifted}}$ by one unit, depending on whether we have, respectively, a downward- or upward-shifted template.

A closure test is performed using pseudo-data, given by the sum of MC simulated signal and background events and the multijet background obtained from data. Different pseudo-experiments are generated so as to be able to change signal yields and verify that the fit determines the τ_h identification efficiency without bias when the signal fraction differs from the nominal value.

An uncertainty of 3.9% is added in quadrature to the uncertainty in ϵ_τ determined in the fit. The value of 3.9% represents the uncertainty to pass the loose τ_h candidate selections, and in particular to reconstruct a track with $p_T > 5$ GeV.

The τ_h identification efficiencies measured in the data are quoted relative to the MC expectation. The results are given in Table 3. The data-to-MC ratios obtained using m_{vis} and N_{tracks} are compatible. All ratios are compatible with unity within the estimated uncertainties of $\approx 4.5\%$. Plots of the m_{vis} and N_{tracks} distributions in the pass and fail regions are presented in Figs. 13 and 14.

The fits of the N_{tracks} distribution are repeated for the pass and fail samples, split into bins of p_T and η , and into bins of N_{vtx} , to obtain the dependence of the tau identification efficiency on p_T and η of the τ_h candidate, and on pileup, respectively. The results are illustrated in Figs. 15 and 16. Within uncertainties, amounting to $\approx 5\%$, the scale factors are compatible with unity.

The efficiency for τ_h decays in $Z/\gamma^* \rightarrow \tau\tau$ events to pass the discriminants for vetoing electrons and muons, described in Section 5.3, are also measured, using a template fit to the m_{vis} distribution. Events passing the selection criteria described above, and containing a τ_h candidate with $p_T > 20$ GeV and $|\eta| < 2.3$ reconstructed in one of the decay modes $h^\pm, h^\pm\pi^0, h^\pm\pi^0\pi^0$, or

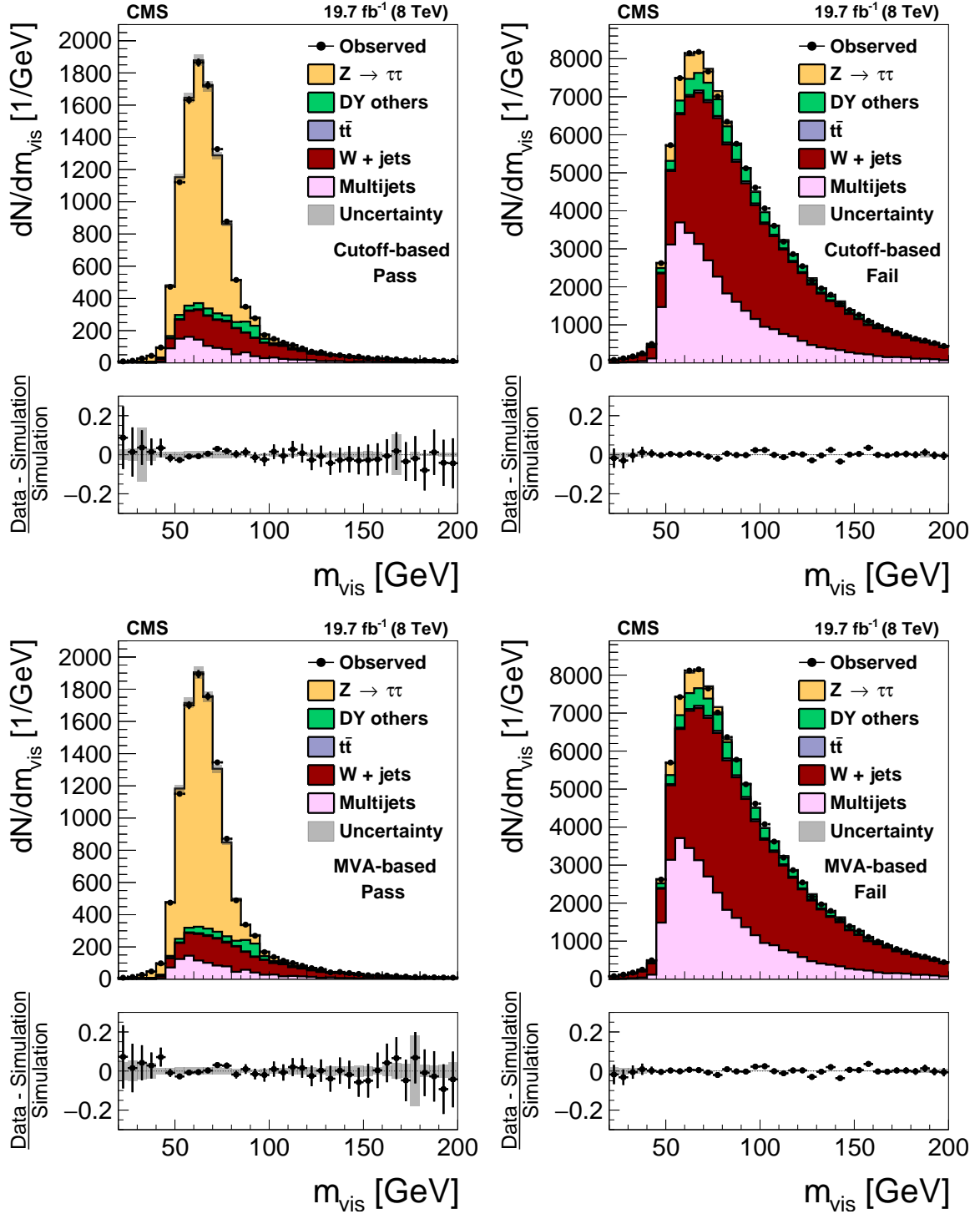


Figure 13: Distribution in m_{vis} observed in the pass (left) and fail (right) samples of $Z/\gamma^* \rightarrow \tau\tau$ candidate events used to measure the τ_h identification efficiency, compared to the MC expectation, for the loose WP of the cutoff-based (top) and MVA-based (bottom) τ_h isolation discriminants. $Z/\gamma^* \rightarrow \ell\ell$ ($\ell = e, \mu, \tau$) events in which either the reconstructed muon or the reconstructed τ_h candidate is due to a misidentification are denoted by “DY others”. The expected m_{vis} distribution is shown for the values of nuisance parameters obtained from the likelihood fit to the data, described in Section 7.3. The “Uncertainty” bands represent the statistical and systematic uncertainties added in quadrature.

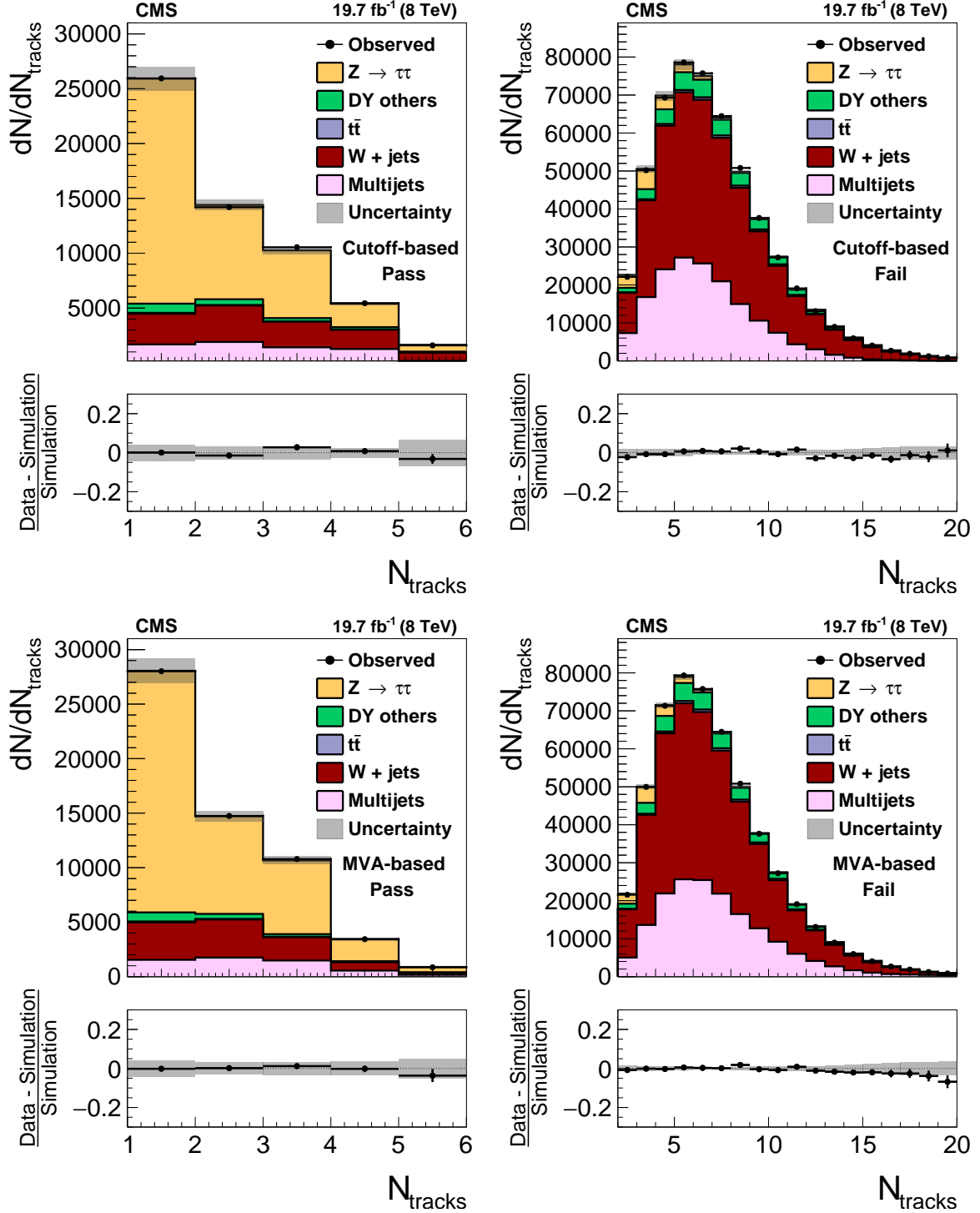


Figure 14: Distribution in N_{tracks} observed in the pass (left) and fail (right) samples of $Z/\gamma^* \rightarrow \tau\tau$ candidate events used to measure the τ_h identification efficiency, compared to the MC expectation, for the loose WP of the cutoff-based (top) and MVA-based (bottom) τ_h isolation discriminants. $Z/\gamma^* \rightarrow \ell\ell$ ($\ell = e, \mu, \tau$) events in which either the reconstructed muon or the reconstructed τ_h candidate is due to a misidentification are denoted by “DY others”. The expected N_{tracks} distribution is shown for the values of nuisance parameters obtained from the likelihood fit to the data, described in Section 7.3. The “Uncertainty” bands represent the statistical and systematic uncertainties added in quadrature.

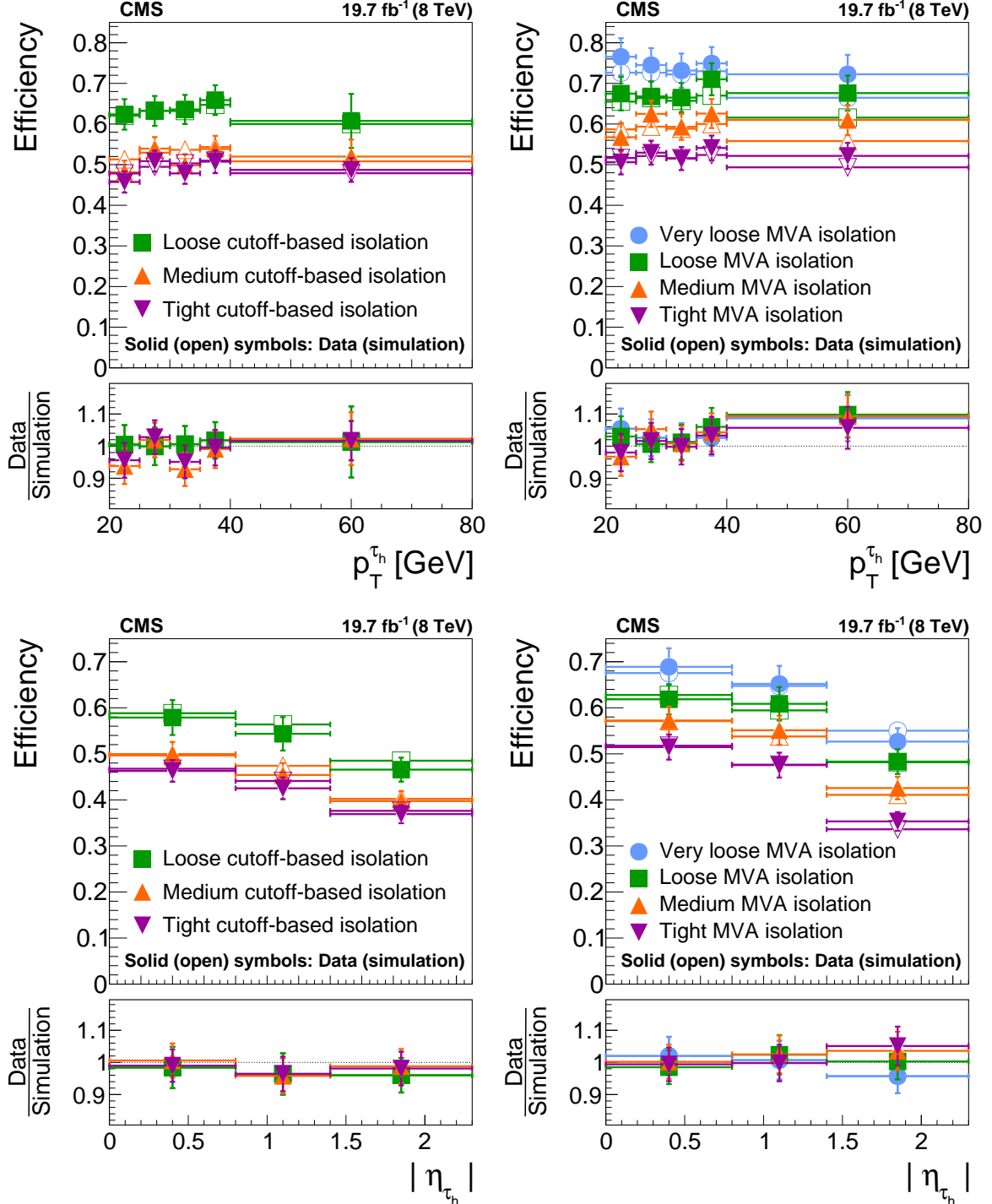


Figure 15: Tau identification efficiency measured in $Z/\gamma^* \rightarrow \tau\tau \rightarrow \mu\tau_h$ events as function of p_T and η , for the cutoff-based and MVA-based τ_h isolation discriminants, compared to the MC expectation. The efficiency is computed relative to τ_h candidates passing the loose τ_h candidate selection described in Section 8.1.

Table 3: Data-to-MC ratios of the efficiency for τ_h decays to pass different identification discriminants, measured in $Z/\gamma^* \rightarrow \tau\tau \rightarrow \mu\tau_h$ events. The results obtained using the observables m_{vis} and N_{tracks} are quoted in separate columns.

WP	Data/Simulation	
	m_{vis}	N_{tracks}
Cutoff-based		
Loose	1.006 ± 0.044	0.963 ± 0.051
Medium	0.984 ± 0.044	0.982 ± 0.048
Tight	0.982 ± 0.044	0.997 ± 0.052
MVA-based		
Very loose	1.034 ± 0.044	0.940 ± 0.086
Loose	1.017 ± 0.044	1.026 ± 0.054
Medium	1.014 ± 0.044	0.992 ± 0.057
Tight	1.015 ± 0.045	0.975 ± 0.052

$h^\pm h^\mp h^\pm$, and passing the loose WP of the cutoff-based tau isolation discriminant, are divided into pass and fail samples, depending on whether the τ_h candidate passes or fails the electron or muon discriminants of Section 5.3, respectively. The efficiencies measured in data are in agreement with the MC expectation within the uncertainty of the measurement, amounting to less than 1%.

8.2 Tau identification efficiency in $t\bar{t} \rightarrow b\bar{b}\mu\tau_h$ events

The sample of $t\bar{t} \rightarrow b\bar{b}\mu\tau_h$ candidate events is selected as described in Section 7.1.2. The high level of background contamination in the $t\bar{t} \rightarrow b\bar{b}\mu\tau_h$ event sample impedes the measurement of the τ_h identification efficiency using the number of τ_h decays that pass and fail τ identification criteria. Instead, we determine the τ_h identification efficiency ε_τ from the yield of $t\bar{t} \rightarrow b\bar{b}\mu\tau_h$ signal events passing τ_h identification criteria, using the relation:

$$\varepsilon_\tau = \frac{N_{\text{pass}}^\tau}{\varepsilon_{\text{non-}\tau} L \sigma_{t\bar{t}}}, \quad (13)$$

where N_{pass}^τ denotes the number of observed $t\bar{t} \rightarrow b\bar{b}\mu\tau_h$ signal events, and is obtained through a template fit that takes into account the contribution of background processes. The symbol L denotes the integrated luminosity of the analyzed data, and $\sigma_{t\bar{t}}$ the product of the $t\bar{t}$ production cross section and the branching fraction. The efficiency of the event selection criteria other than the identification efficiency of τ_h is denoted by $\varepsilon_{\text{non-}\tau}$, and is obtained from the MC simulation. The MC-to-data corrections are applied for the muon trigger, identification, and isolation efficiencies, and for the E_T^{miss} resolution. Residual differences between data and MC simulation that may affect $\varepsilon_{\text{non-}\tau}$ are considered as systematic uncertainties. We refer to this sample as the pass region.

The number of N_{pass}^τ events, as well as the contributions from background processes, are determined by fitting the distribution in m_T of Eq. (3) in the selected event sample, using templates for signal and background processes.

The templates for the $t\bar{t} \rightarrow b\bar{b}\mu\tau_h$ signal and for DY, W+jets, single top quark, and diboson backgrounds are obtained from the MC simulation. Due to the $t\bar{t}$ contribution in the high- m_T sideband, the normalization of the W+jets background cannot be determined from the data, and is taken from the MC simulation, with an uncertainty of 30%. A substantial background arises from $t\bar{t}$ events in which the reconstructed τ_h candidate corresponds to either a jet $\rightarrow \tau_h$,

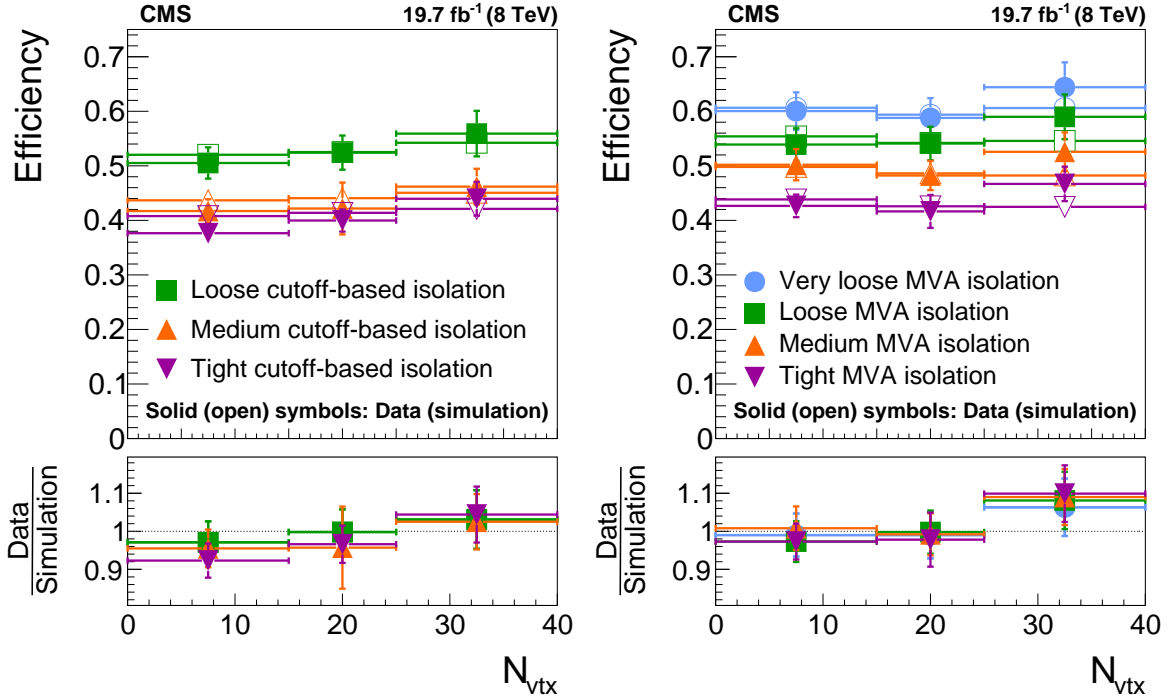


Figure 16: Tau identification efficiency measured in $Z/\gamma^* \rightarrow \tau\tau \rightarrow \mu\tau_h$ events as a function of the number of reconstructed vertices N_{vtx} , for the cutoff-based and MVA-based τ_h isolation discriminants, compared to the MC expectation. The efficiency is computed relative to τ_h candidates passing the loose τ_h candidate selection described in Section 8.1.

$e \rightarrow \tau_h$, or $\mu \rightarrow \tau_h$ misidentification. The $t\bar{t}$ background with such τ_h candidates is included in the fit as a separate contribution with an independent normalization. The template for the $t\bar{t}$ background is obtained from the MC simulation. The multijet template is obtained from a control region, by applying event selection criteria that are similar to the pass region, except that the muon isolation requirement is changed to $I_\mu > 0.10 p_T^\mu$ and the jets are not required to pass b tagging criteria. The contribution from $t\bar{t}$ and backgrounds from sources other than multijet events are subtracted according to MC predictions, using the samples and cross sections described in Section 3. Because of this subtraction, the template for the multijet background depends on systematic uncertainties that affect the $t\bar{t}$ signal and non-multijet backgrounds. The dependence is taken into account through suitable changes in the template as function of the corresponding nuisance parameters in the fit.

Systematic uncertainties that can affect the yield of $t\bar{t} \rightarrow b\bar{b}\mu\tau_h$ signal in the pass region, as well as the rate for background processes, are constrained using a control region dominated by $t\bar{t} \rightarrow b\bar{b}\mu\mu$ events, which we refer to as the dimuon region.

Events in the dimuon region are selected by requiring two muons with $p_T > 20 \text{ GeV}$ and $|\eta| < 2.4$, passing tight identification and isolation criteria. The muons are required to be of opposite charge, and to be compatible with originating from the same vertex. The mass of the muon pair is required to exceed $m_{\mu\mu} > 50 \text{ GeV}$, and not be within 10 GeV of the nominal Z boson mass, i.e. requiring $|m_{\mu\mu} - m_Z| > 10 \text{ GeV}$. The event is also required to pass the single-muon trigger. At least one of the muons is required to satisfy the conditions $p_T > 25 \text{ GeV}$ and $|\eta| < 2.1$, to ensure that the single-muon trigger is fully efficient. The event is further required to contain two jets with $p_T > 30 \text{ GeV}$ and $|\eta| < 2.5$, separated from each of the muons by $\Delta R > 0.5$. At least one of the jets is required to pass b tagging criteria. The E_T^{miss} in the event must be $> 40 \text{ GeV}$. Events

containing additional electrons with $p_T > 15 \text{ GeV}$ and $|\eta| < 2.3$, or muons with $p_T > 10 \text{ GeV}$ and $|\eta| < 2.4$ that pass loose identification and isolation criteria, are rejected.

The trigger and event selection criteria that are applied to select $t\bar{t} \rightarrow b\bar{b}\mu\tau_h$ and $t\bar{t} \rightarrow b\bar{b}\mu\mu$ events are chosen to be as similar as possible. This ensures that the systematic uncertainties affecting the yield of signal and background processes are the same in the pass and in the dimuon regions. The m_T distributions observed in the two regions are fitted simultaneously. In the dimuon control region, the transverse mass is computed by choosing one of the two muons at random.

The data-to-MC ratios of τ_h identification efficiencies measured in $t\bar{t} \rightarrow b\bar{b}\mu\tau_h$ events are given in Table 4. Within the uncertainty of the measurement of 9–11%, the efficiencies of all τ_h identification discriminators are compatible with the MC expectations. Plots of the distribution in m_T in the pass and dimuon control regions are shown in Fig. 17. Data and MC simulation agree within uncertainties after the fit.

Table 4: Data-to-MC ratios of the efficiency for τ_h decays in $t\bar{t} \rightarrow b\bar{b}\mu\tau_h$ events to pass different τ_h identification discriminants.

WP	Data/Simulation
Cutoff-based	
Loose	1.037 ± 0.097
Medium	1.050 ± 0.107
Tight	1.047 ± 0.108
MVA-based	
Very loose	0.927 ± 0.097
Loose	1.009 ± 0.097
Medium	0.956 ± 0.118
Tight	1.080 ± 0.117

9 Measurement of the τ_h energy scale

The energy scale for τ_h (referred to as τES), defined as the average reconstructed τ_h energy relative to the generator level energy of the visible τ decay products, is an important source of systematic uncertainty in many analyses with τ leptons in the final state. In particular, τES has a significant influence on the potential to discover a $H \rightarrow \tau\tau$ signal in the presence of the dominant irreducible background from $DY Z/\gamma^* \rightarrow \tau\tau$ production in the $\tau\tau$ mass distribution [1].

An MC-to-data τES correction is determined by fitting the distributions of observables sensitive to the energy scale, using a sample of $Z/\gamma^* \rightarrow \tau\tau \rightarrow \mu\tau_h$ events. The events are selected as described in Section 7.1.1, except that the τ_h candidates are required to pass the medium WP of the MVA-based τ_h isolation discriminant, instead of the loose WP of the cutoff-based discriminant.

The τES is measured separately for τ_h candidates reconstructed in the decay modes $h^\pm, h^\pm\pi^0\text{s}$, and $h^\pm h^\mp h^\pm$ in bins of $20 < p_T < 30 \text{ GeV}$, $30 < p_T < 45 \text{ GeV}$, and $p_T > 45 \text{ GeV}$.

Two alternative observables are used to perform the fit: the reconstructed mass of the τ_h candidate m_{τ_h} , and m_{vis} , the mass of muon and τ_h candidate. The m_{vis} and m_{τ_h} templates for the $Z/\gamma^* \rightarrow \tau\tau$ signal are computed by changing the τ_h four-momentum, reconstructed as described in Section 5.1, as a function of τES , and recomputing m_{vis} and m_{τ_h} after each such change. For τ_h candidates reconstructed in the $h^\pm\pi^0\text{s}$ and $h^\pm h^\mp h^\pm$ modes, all components of

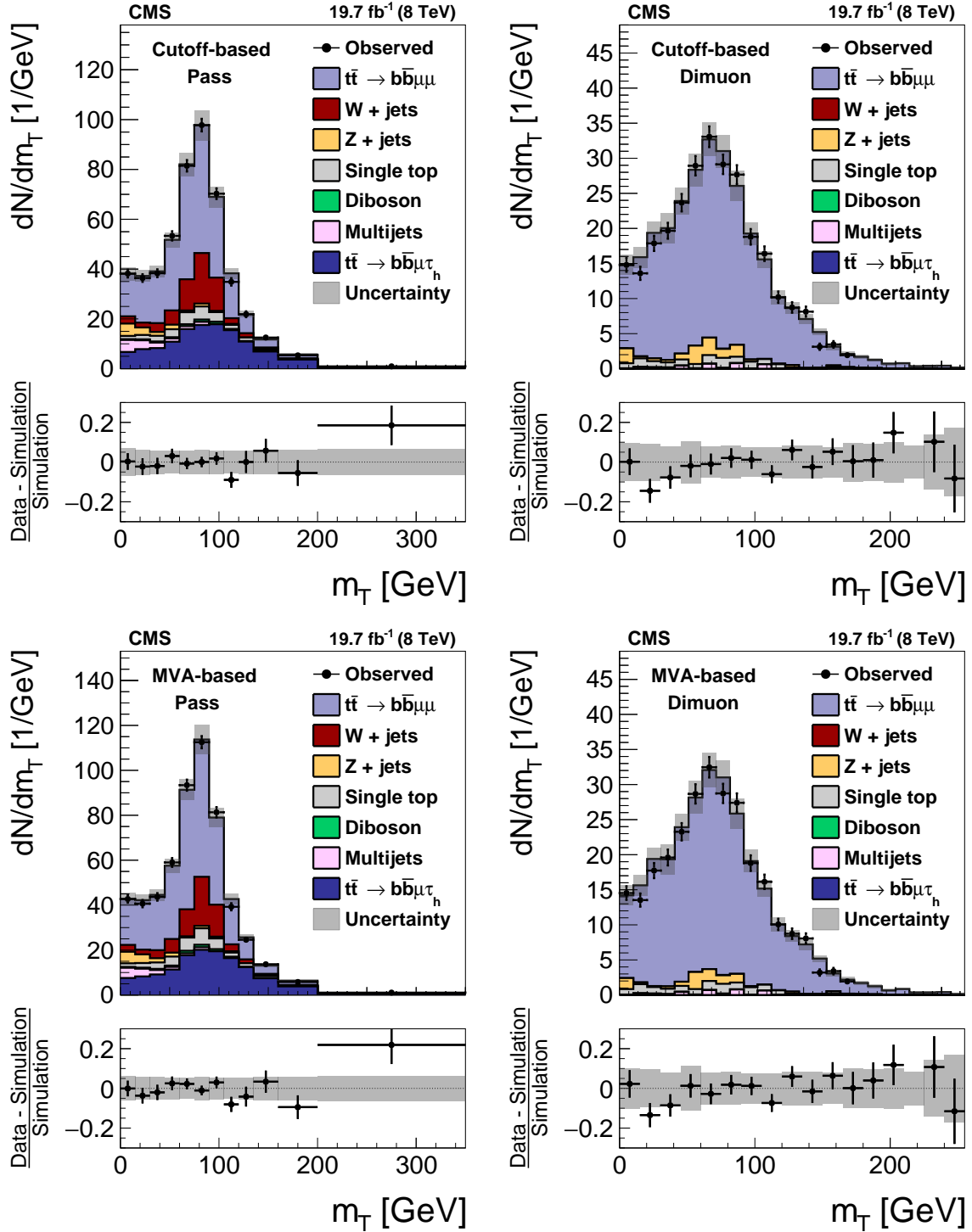


Figure 17: Distribution in the transverse mass of the muon and E_T^{miss} in the pass region (left) and in the dimuon region (right) in $t\bar{t}$ events used to measure the τ_h identification efficiency, for the loose WP of the cutoff-based (top) and MVA-based (bottom) τ_h isolation discriminants, respectively. The $t\bar{t}$ events in which either the reconstructed muon or the reconstructed τ_h candidate are misidentified are denoted by “ $t\bar{t}$ others”. The expected m_T distribution is shown for the values of nuisance parameters obtained from the likelihood fit to the data, as described in Section 7.3. The “Uncertainty” band represents the statistical and systematic uncertainties added in quadrature.

the τ_h four-vector are scaled by the given τ ES factor, while for τ_h candidates in the h^\pm decay mode we scale the energy and adjust the momentum such that η , ϕ and mass of the four-vector remain unchanged. The observable m_{τ_h} is defined only for τ_h candidates reconstructed in the $h^\pm\pi^0$ s and $h^\pm h^\mp h^\pm$ modes, and the energy scale of τ_h candidates reconstructed in the h^\pm decay mode is measured via m_{vis} .

The $Z/\gamma^* \rightarrow \tau\tau$ signal is modelled via the “embedding” technique [1]. The method is based on selecting $Z/\gamma^* \rightarrow \mu\mu$ events in data, and replacing the reconstructed muons by generator-level τ leptons. The τ decays are simulated using TAUOLA, and the GEANT4-based detector simulation is used to model the detector response to the τ decay products. The visible τ decay products are reconstructed with the PF algorithm, and mixed with the remaining particles of the $Z/\gamma^* \rightarrow \mu\mu$ event, after the two muons are removed. Finally, τ_h candidates, jets, and E_T^{miss} are reconstructed, the isolation of electrons and muons is computed, and the event is analyzed as if it were data. Embedded samples are produced for the entire data-taking period, covering the same run ranges as the data used to measure the τ ES correction.

The $Z/\gamma^* \rightarrow \ell\ell$ ($\ell = e, \mu$), W +jets, $t\bar{t}$, single top quark, and diboson backgrounds are modelled using MC simulation. The templates for background processes are kept unchanged as function of τ ES.

The multijet background is obtained directly from data, using events in which the muon is not isolated, and of the same charge as the τ_h candidate, as described in Section 8.1.

For illustration, the m_{τ_h} templates corresponding to τ ES shifts of 0, -6 , and $+6\%$ are shown for τ_h candidates of $20 < p_T < 30$ GeV in Fig. 18. The data are compared to the sum of $Z/\gamma^* \rightarrow \tau\tau$ and expected background distributions. A positive and negative slope in the data-to-MC ratio shown in the bottom parts of the figures indicates that the best-fit values of the τ ES correction are, respectively, larger and smaller than the shift shown in the figure.

The best-fit values for the τ ES correction are presented in Fig. 19. The variable m_{τ_h} is seen to be the more sensitive observable compared to m_{vis} , as indicated by smaller uncertainties.

Numerical values of the measured τ ES corrections are given in Table 5. The τ ES corrections obtained using the observables m_{vis} and m_{τ_h} agree within their uncertainties. For τ_h reconstructed in the decay modes h^\pm and $h^\pm h^\mp h^\pm$, the energy scale measured in data agrees with the simulation. The energy of τ_h candidates reconstructed in the decay mode $h^\pm\pi^0$ s is lower by about 1% in data than in simulation. We do not find any indication of a dependence of the measured τ ES corrections on $p_T^{\tau_h}$.

10 Measurement of the misidentification rate for jets

The rate for quark and gluon jets to be misidentified as τ_h decays is measured in W +jets and multijet events. The events are selected as described in Sections 7.1.3 and 7.1.4, respectively.

The jet $\rightarrow \tau_h$ misidentification rate is measured as a function of jet p_T and η , and as a function of N_{vtx} . The rate is computed according to Eq. (8). The jets considered in the denominator are required to pass a set of loose jet identification criteria [49], and to be compatible with originating from the primary collision vertex.

The misidentification rates measured in W +jets and in multijet events are shown in Figs. 20–22 and compared to MC expectation. The contributions from background processes, predominantly arising from $t\bar{t}$ and heavy-flavour jet production in the W +jets sample, and from $t\bar{t}$ in the multijet sample, are included in the comparison.

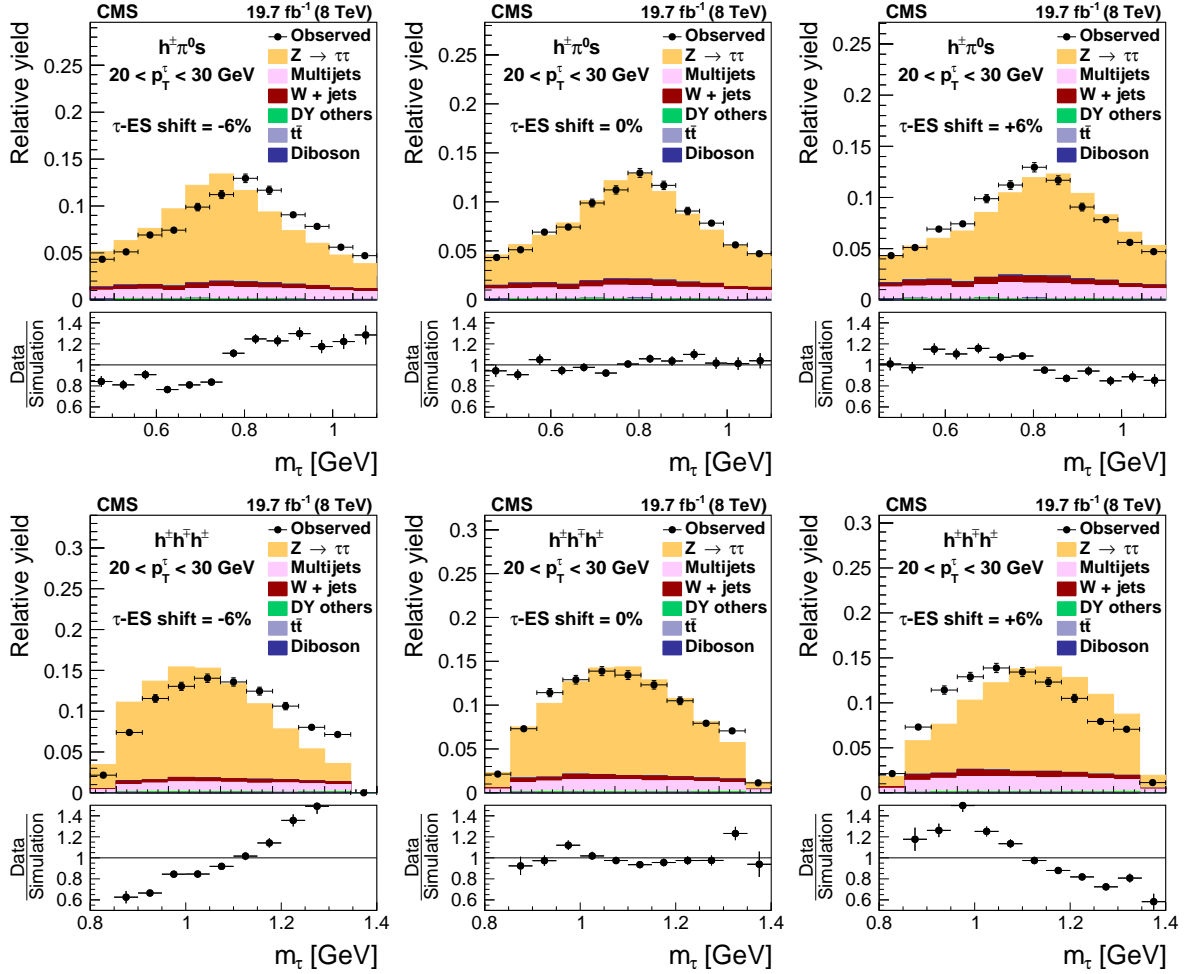


Figure 18: Distribution in m_{τ_h} , observed in events containing τ_h candidates of $20 < p_T < 30$ GeV, reconstructed in the decay modes $h^\pm \pi^0 s$ (top) and $h^\pm h^\mp h^\pm$ (bottom), compared to the sum of $Z/\gamma^* \rightarrow \tau\tau$ signal plus background expectation. The m_{τ_h} shape templates for the $Z/\gamma^* \rightarrow \tau\tau$ signal are shown for τ ES variations of -6% (left), 0% (centre) and $+6\%$ (right). For clarity, the symbols p_T^τ and m_τ are used instead of $p_T^{\tau_h}$ and m_{τ_h} in these plots.

In general, the misidentification rates are higher in W+jets than in multijet events. The difference is due to the higher fraction of quark jets in W+jets events. Quark jets typically have a lower particle multiplicity and are more collimated than gluon jets, thereby increasing their probability to be misidentified as τ_h decays. The jet $\rightarrow \tau_h$ misidentification rates for quark jets as well as gluon jets typically decrease as function of jet p_T , as particle multiplicities increase for jets with larger p_T .

Moderate increases in the rate of jet $\rightarrow \tau_h$ are observed at high pileup and at large $|\eta|$. The increase in the misidentification rate as a function of N_{vtx} is due to the $\Delta\beta$ correction described in Section 5.2.1, which, in events with high pileup, effectively relaxes the criteria on neutral-particle isolation, as is necessary to maintain a high τ_h identification efficiency. The effect is reduced for the MVA-based τ_h isolation discriminant. The increase of the misidentification rate at high $|\eta|$ results from a decrease in track reconstruction efficiency near the edge of the geometric acceptance of the tracking detectors, which reduces the effectiveness of the isolation criteria. The dependence of the misidentification rate on N_{vtx} and η increases with jet p_T , and is therefore more pronounced for multijet events compared to W+jets events. Overall, the jet

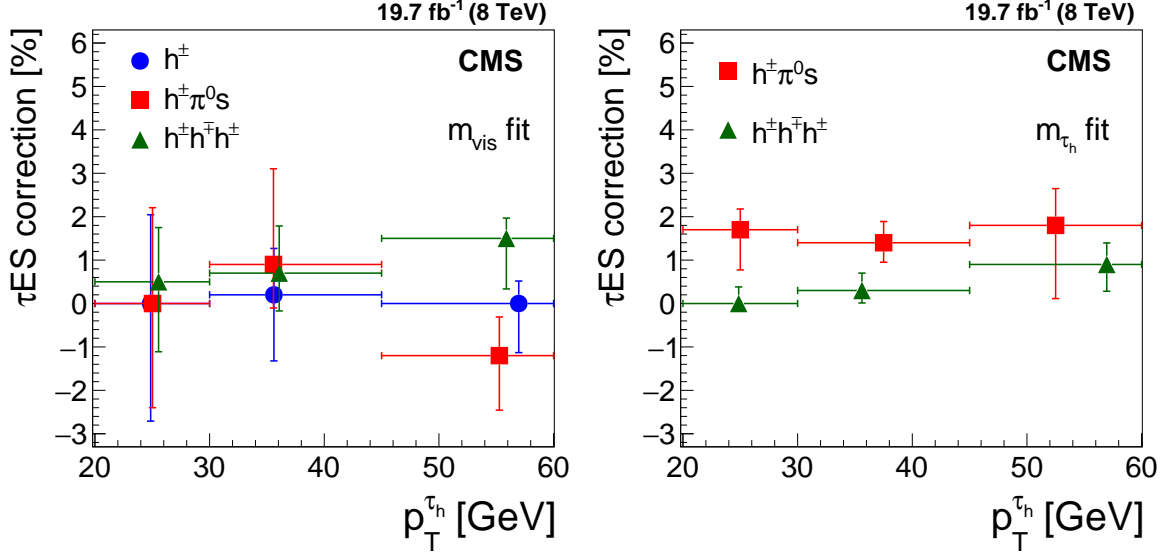


Figure 19: Energy scale corrections for τ_h measured in $Z/\gamma^* \rightarrow \tau\tau$ events, using the distribution in (left) visible mass of muon and τ_h and (right) of the τ_h candidate mass, for τ_h reconstructed in different decay modes and in different ranges of τ_h candidate p_T .

Table 5: Energy scale corrections for τ_h measured in $Z/\gamma^* \rightarrow \tau\tau$ events, using the distribution in m_{vis} and m_{τ_h} , for τ_h reconstructed in different decay modes and τ_h p_T bins. The τ ES corrections measured for the combination of all τ_h decay modes and p_T bins are also given in the table. It is obtained by means of an independent fit and hence may be different from the average of τ ES corrections measured for individual decay modes.

τ ES correction measured using m_{vis} [%]				
Decay mode	$20 < p_T < 30 \text{ GeV}$	$30 < p_T < 45 \text{ GeV}$	$p_T > 45 \text{ GeV}$	All p_T
h^\pm	0.0 ± 2.3	0.2 ± 1.3	0.0 ± 0.8	0.2 ± 0.5
$h^\pm \pi^0 s$	0.0 ± 2.3	0.9 ± 1.6	-1.2 ± 1.0	-0.3 ± 0.6
$h^\pm h^\mp h^\pm$	0.5 ± 1.4	0.7 ± 1.0	1.5 ± 0.8	0.9 ± 0.7
All decay modes	0.9 ± 1.7	0.7 ± 0.8	0.1 ± 0.7	0.5 ± 0.5

τ ES correction measured using m_{τ_h} [%]				
Decay mode	$20 < p_T < 30 \text{ GeV}$	$30 < p_T < 45 \text{ GeV}$	$p_T > 45 \text{ GeV}$	All p_T
h^\pm	—	—	—	—
$h^\pm \pi^0 s$	1.7 ± 0.6	1.4 ± 0.4	1.8 ± 1.0	1.5 ± 0.4
$h^\pm h^\mp h^\pm$	0.0 ± 0.3	0.3 ± 0.3	0.9 ± 0.6	0.3 ± 0.2

→ τ_h misidentification rates vary between $\approx 10^{-4}$ and $\approx 4 \times 10^{-2}$.

Notable differences are observed in the data/MC rate with which quark and gluon jets in W +jets and multijet events pass the cutoff-based and MVA-based isolation discriminants at high $|\eta|$. Comparison with the rates for τ_h identification discriminants based on charged-particle isolation demonstrate that the difference is due to imprecise modelling of neutral particle isolation in the high $|\eta|$ region in MC simulation. The effect is caused by a restriction in detector simulation to a time window of ± 50 ns around the nominal bunch crossing, while the ECAL electronics samples the signal amplitudes in 10 consecutive intervals of 25 ns within a time window of -75 ns to $+150$ ns in order to correct, on an event-by-event basis, the energy reconstructed in the crystals for out-of-time pileup [65]. The restriction in detector simulation to a time window of ± 50 ns leads to a moderate mismodelling of the effect of out-of-time pileup

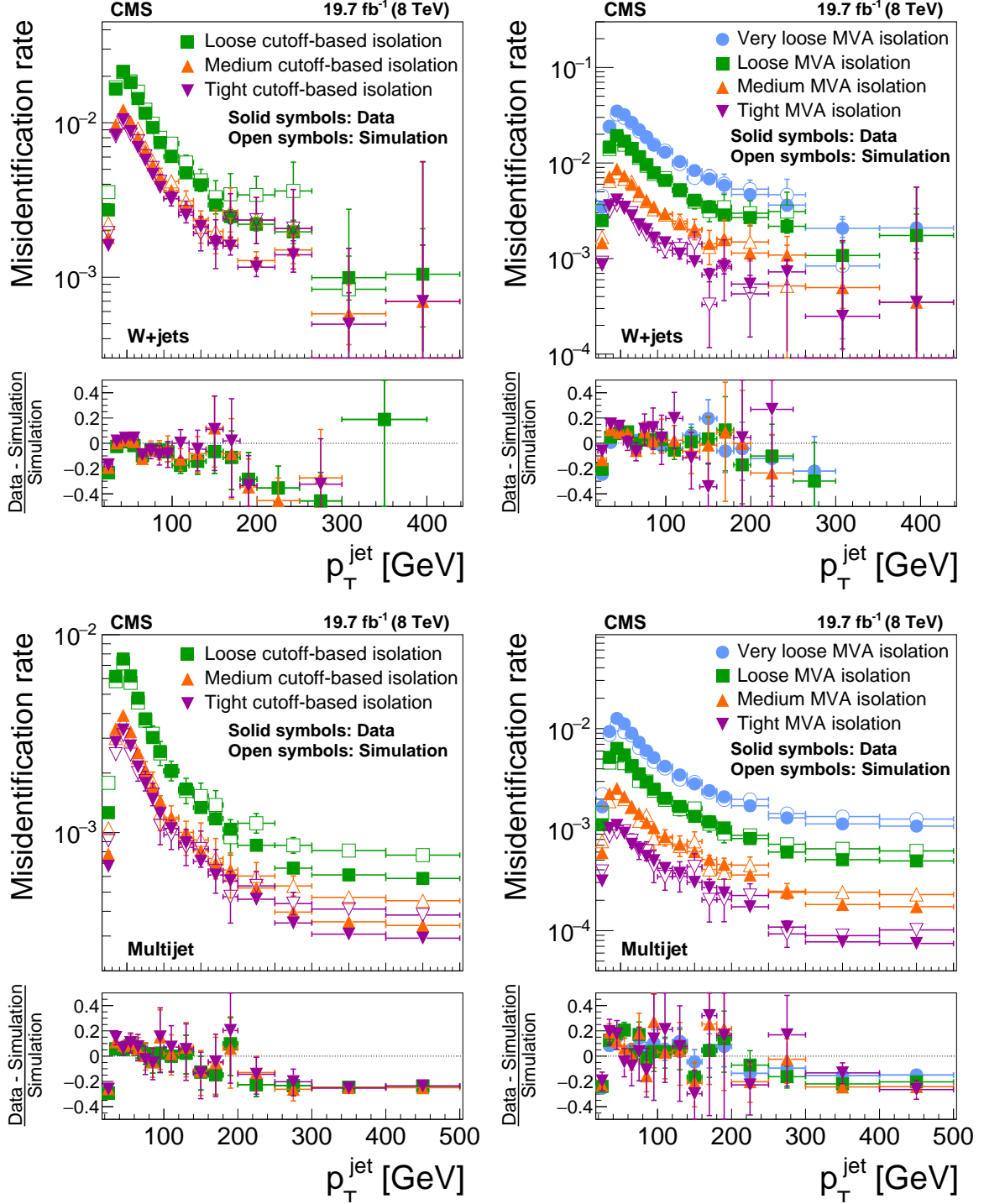


Figure 20: Probabilities for quark and gluon jets in W+jets (top) and multijet (bottom) events to pass the cutoff-based (left) and MVA-based (right) τ_h isolation discriminant, as a function of jet p_T . The misidentification rates measured in the data are compared to the MC expectation.

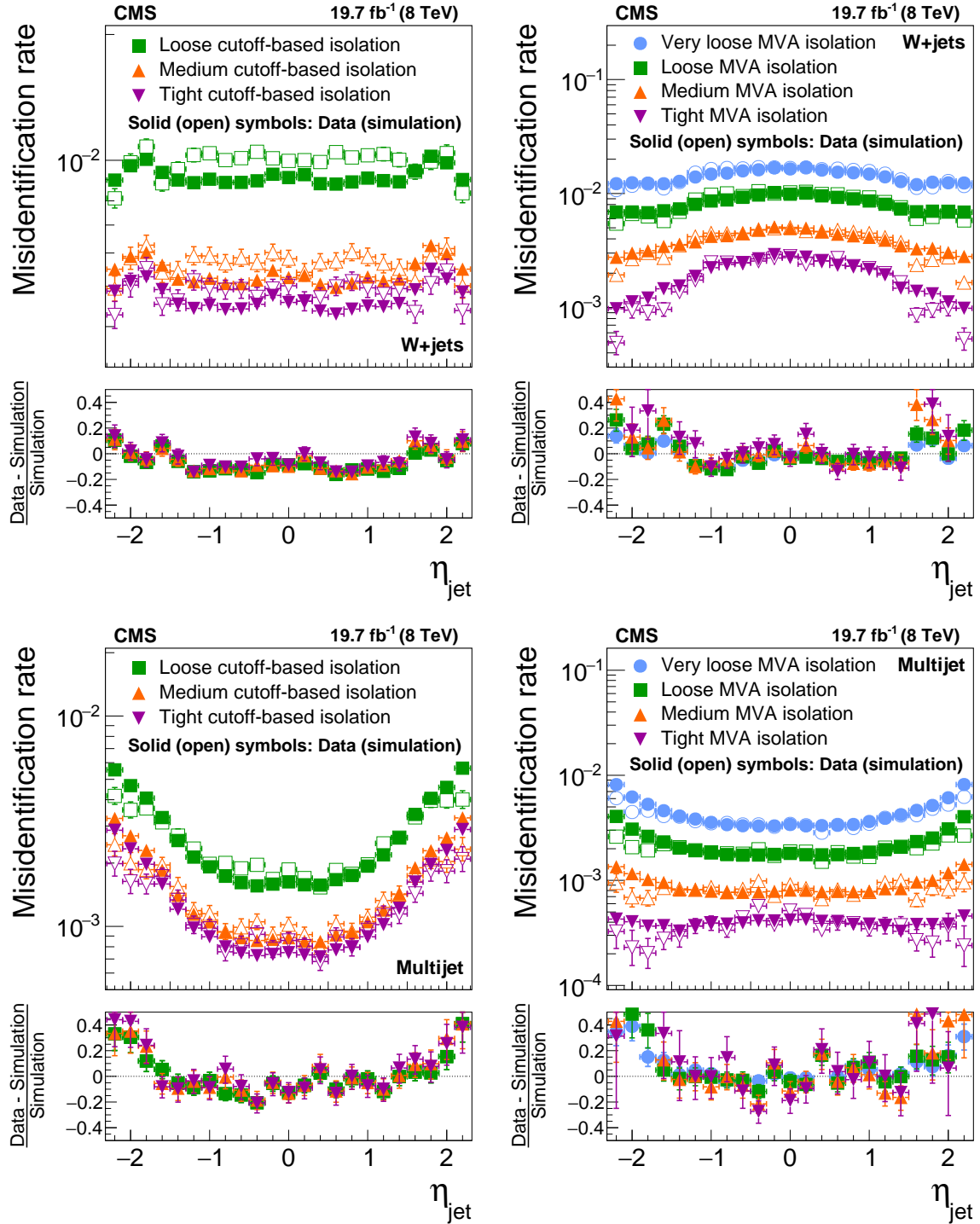


Figure 21: Probabilities for quark and gluon jets in W +jets (top) and multijet (bottom) events to pass the cutoff-based (left) and MVA-based (right) τ_h isolation discriminant, as a function of jet η . The misidentification rates measured in the data are compared to the MC expectation.

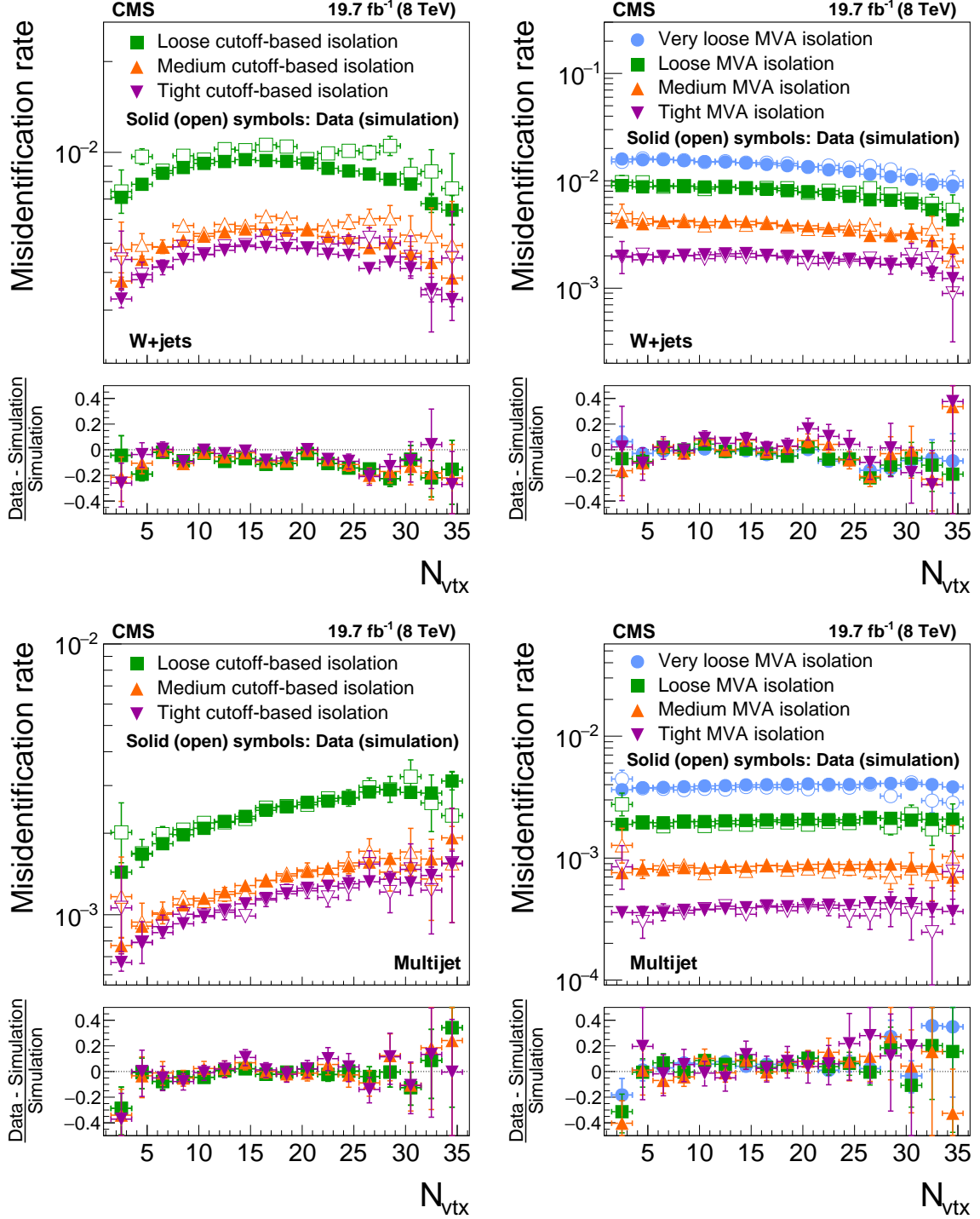


Figure 22: Probabilities for quark and gluon jets in W +jets (top) and multijet (bottom) events to pass the cutoff-based (left) and MVA-based (right) τ_h isolation discriminant, as a function of N_{vtx} . The misidentification rates measured in the data are compared to the MC expectation.

on the isolation of τ_h candidates reconstructed in the ECAL endcap with respect to neutral particles.

A trend is observed in the ratio of misidentification rates measured in multijet events relative to the MC simulation as a function of p_T . While the rates for $\text{jet} \rightarrow \tau_h$ measured in data exceed the MC expectation at low p_T , the rates measured at high p_T fall short of the simulation. The magnitude of the effect on the data/MC ratio is $\approx 20\%$. The trend is observed for the cutoff-based and for the MVA-based τ_h identification discriminants, and is of similar magnitude for jets in the central and forward regions.

11 Measurement of misidentification rates for electrons and muons

The probability for electrons or muons to pass the τ_h identification criteria, and in particular to pass the dedicated discriminants against electrons or muons described in Section 5.3 are measured through the tag-and-probe technique using $Z/\gamma^* \rightarrow ee$ or $Z/\gamma^* \rightarrow \mu\mu$ events [56].

The events are selected as described in Section 7.1.5. The probe is furthermore required to pass the loose WP of the cutoff-based τ_h isolation discriminant. Depending on whether the probe passes the lepton veto discriminator under study, the event enters either the pass or the fail region. When an event contains either two electron or two muon candidates that pass the tight selection criteria and qualify as tags, both combinations of the tag and probe leptons are considered.

The $e \rightarrow \tau_h$ and $\mu \rightarrow \tau_h$ misidentification rate, P_{misid} , is measured using a simultaneous fit of the number of $Z/\gamma^* \rightarrow ee$ or $Z/\gamma^* \rightarrow \mu\mu$ events in the pass and fail regions ($N_{\text{pass}}^{\text{probe}}$ and $N_{\text{fail}}^{\text{probe}}$). The visible mass of the tag and probe pair is fitted using templates for the $Z/\gamma^* \rightarrow ee$ or $Z/\gamma^* \rightarrow \mu\mu$ signal, and $Z/\gamma^* \rightarrow \tau\tau$, W +jets, $t\bar{t}$, single top quark, diboson, and multijet backgrounds. The templates for the $Z/\gamma^* \rightarrow ee$ and $Z/\gamma^* \rightarrow \mu\mu$ signal and for all background processes, except multijets, are obtained from simulation. The normalization is performed according to the cross sections detailed in Section 3, except for the W +jets background, the rate of which is determined from data, using the high- m_T sideband method described in Section 8.1. The distribution and normalization of the multijet background is determined from data, using events in which tag and probe have the same charge. Contributions from other backgrounds to the same-charge control region are subtracted, using the MC predictions. The fit is performed as described in Section 7.3, taking the $e \rightarrow \tau_h$ or $\mu \rightarrow \tau_h$ misidentification rate as the parameter of interest μ . The number of $Z/\gamma^* \rightarrow \ell\ell$ ($\ell = e, \mu$) events in the pass and fail regions are given, respectively, as a function of μ by $N_{\text{pass}}^{\text{probe}} = \mu N^{Z/\gamma^* \rightarrow \ell\ell}$ and $N_{\text{fail}}^{\text{probe}} = (1 - \mu) N^{Z/\gamma^* \rightarrow \ell\ell}$.

Systematic uncertainties are represented by nuisance parameters in the template fits. The uncertainties in the normalization of signal and background processes rescale the yield in the pass and fail region by the same factor. Uncertainties in the energy scale of the tag and probe leptons are represented by uncertainties in the fitted distributions. The energy scales of tag electrons and muons are known with an uncertainty of 1%. Larger uncertainties of 5% and 3% are assigned to the energy scale of probe electrons and muons.

A correction is applied to account for the fact that not all probes in $Z/\gamma^* \rightarrow ee$ or $Z/\gamma^* \rightarrow \mu\mu$ events are electrons or muons. In particular, in the pass region there is a few percent contamination from $\text{jet} \rightarrow \tau_h$. The contamination is corrected by subtracting from the number of $Z/\gamma^* \rightarrow ee$ or $Z/\gamma^* \rightarrow \mu\mu$ events in the fit the expected number of $\text{jet} \rightarrow \tau_h$ misidentifications, obtained from MC simulation. A 20% systematic uncertainty is assigned to the small number of $\text{jet} \rightarrow \tau_h$ events subtracted, motivated by the level of agreement of the $\text{jet} \rightarrow \tau_h$ misidentifi-

cation rates observed between data and simulation presented in Section 10.

11.1 Misidentification rate for electrons

In the measurement of the $e \rightarrow \tau_h$ misidentification rate, the distribution in m_{vis} is fitted within the range $60 < m_{\text{vis}} < 120$ GeV. Separate fits are performed for probes in the barrel ($|\eta| < 1.46$) and in the endcap ($|\eta| > 1.56$) regions of ECAL. Plots of the m_{vis} distributions in the pass and fail regions are presented for the loose WP of the electron discriminant in Fig. 23. In $Z/\gamma^* \rightarrow \tau\tau$ events that enter the pass region, the tag electrons are mainly due to $\tau^- \rightarrow e^- \bar{\nu}_e \nu_\tau$ decays, while the probes are typically due to hadronic τ decays.

The $e \rightarrow \tau_h$ misidentification rates measured for different WP of the electron discriminant are given in Table 6. The measured misidentification rates exceed the MC prediction by up to a factor of 1.7. The difference between data and MC simulation, quantified by the deviation in the ratio data/simulation from unity, increases for tight and very tight WP. Figure 24 shows a graphical comparison of the misidentification rates measured in data to the MC expectation. The measured data/simulation ratios are taken into account in physics analyses by applying suitable MC-to-data correction factors.

Table 6: Probability for electrons to pass different WP of the discriminant against electrons. The $e \rightarrow \tau_h$ misidentification rates measured in $Z/\gamma^* \rightarrow ee$ events are compared to the MC expectation, separately for electrons in the ECAL barrel and endcap regions.

WP	Simulation	Data	Data/Simulation
ECAL barrel ($ \eta < 1.46$)			
Very loose	$(2.06 \pm 0.01) \times 10^{-2}$	$(2.37 \pm 0.06) \times 10^{-2}$	1.15 ± 0.03
Loose	$(4.48 \pm 0.05) \times 10^{-3}$	$(5.61 \pm 0.17) \times 10^{-3}$	1.25 ± 0.04
Medium	$(1.73 \pm 0.03) \times 10^{-3}$	$(2.30 \pm 0.18) \times 10^{-3}$	1.33 ± 0.10
Tight	$(9.70 \pm 0.02) \times 10^{-4}$	$(1.28 \pm 0.21) \times 10^{-3}$	1.32 ± 0.21
Very tight	$(6.83 \pm 0.02) \times 10^{-4}$	$(1.13 \pm 0.20) \times 10^{-3}$	1.66 ± 0.30
ECAL endcap ($ \eta > 1.56$)			
Very loose	$(2.93 \pm 0.02) \times 10^{-2}$	$(3.11 \pm 0.09) \times 10^{-2}$	1.06 ± 0.03
Loose	$(4.46 \pm 0.09) \times 10^{-3}$	$(4.67 \pm 0.22) \times 10^{-3}$	1.05 ± 0.05
Medium	$(1.54 \pm 0.05) \times 10^{-3}$	$(1.83 \pm 0.22) \times 10^{-3}$	1.19 ± 0.15
Tight	$(8.83 \pm 0.38) \times 10^{-4}$	$(1.16 \pm 0.26) \times 10^{-3}$	1.32 ± 0.31
Very tight	$(6.50 \pm 0.33) \times 10^{-4}$	$(1.04 \pm 0.26) \times 10^{-3}$	1.60 ± 0.40

11.2 Misidentification rate for muons

In the measurement of the $\mu \rightarrow \tau_h$ misidentification rate, the distribution in m_{vis} is fitted within the range $60 < m_{\text{vis}} < 120$ GeV. The fit is performed separately in the regions $|\eta| < 1.2$, $1.2 \leq |\eta| \leq 1.7$, and $|\eta| > 1.7$. Plots of the m_{vis} distributions in the pass and fail regions are presented for the loose WP of the cutoff-based muon discriminant in Figs. 25 and 26. In $Z/\gamma^* \rightarrow \tau\tau$ events that enter the pass region, the tag muons are mainly due to $\tau^- \rightarrow \mu^- \bar{\nu}_\mu \nu_\tau$ decays, while the probes are typically due to hadronic τ decays.

The $\mu \rightarrow \tau_h$ misidentification rates measured for different WP of the cutoff-based and MVA-based muon discriminants are given in Table 7. The rates measured in the data exceed the MC prediction. The difference between data and MC simulation is higher in the forward than in the central region, and increases as the muon rejection criteria are tightened. Figure 27 illustrates the results given in Table 7. The observed differences between data and simulation have little effect on most analyses, as the background due to muons that get misidentified as τ_h decays is typically very small compared to other backgrounds.

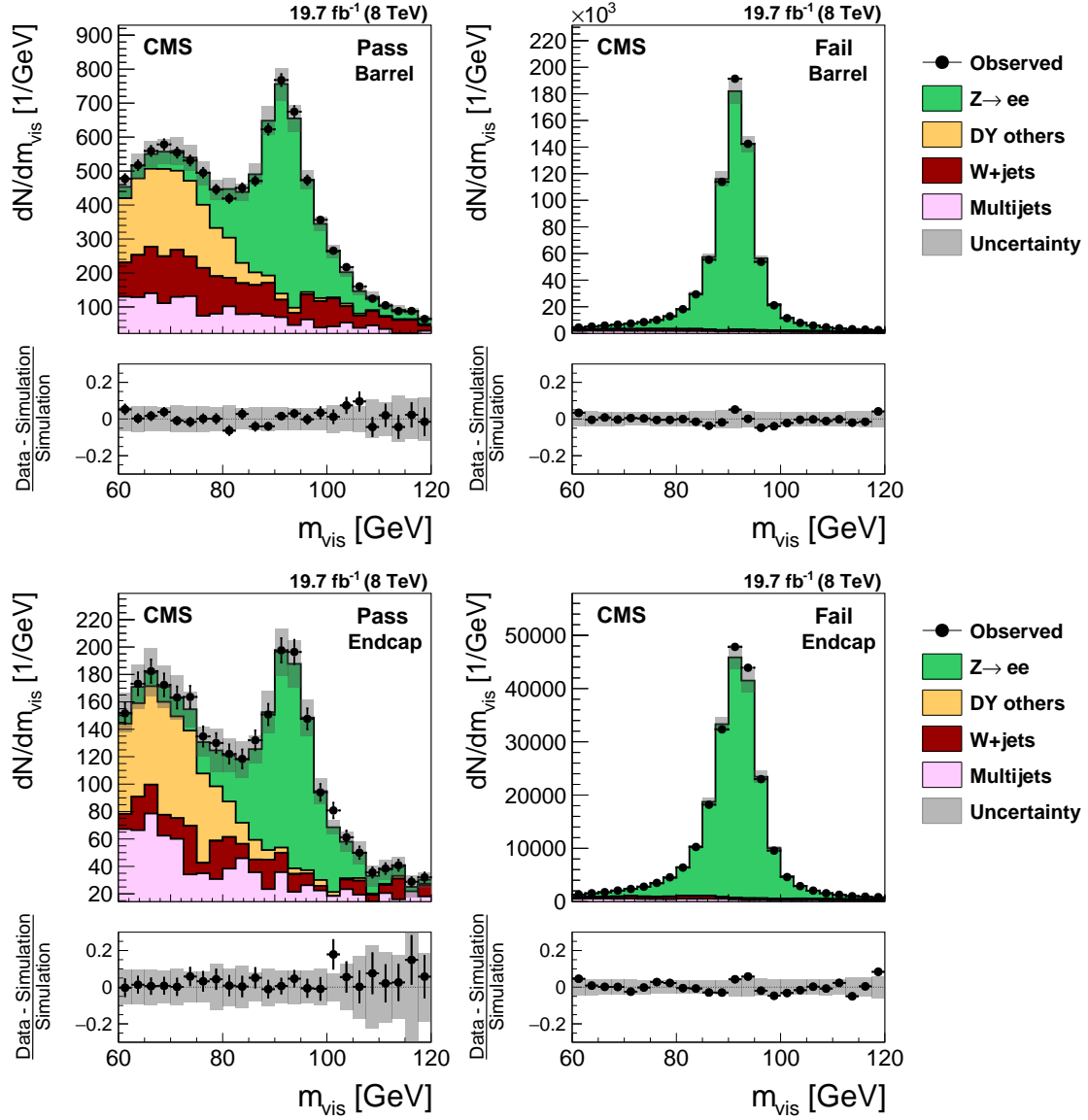


Figure 23: Distribution in the visible mass of the tag and probe pair in the pass (left) and fail (right) regions, for the loose WP of the electron discriminant in the barrel (top) and endcap (bottom) regions. The distributions observed in $Z/\gamma^* \rightarrow ee$ candidate events selected in data are compared to the MC expectation, shown for the values of nuisance parameters obtained from the likelihood fit to the data, as described in Section 7.3. The contributions from $Z/\gamma^* \rightarrow \tau\tau$ background are denoted by “DY others”. The $t\bar{t}$, single top quark, and diboson backgrounds yield a negligible contribution to the selected event sample and, while present in the fit, are omitted from the legend. The “Uncertainty” band represents the statistical and systematic uncertainties added in quadrature.

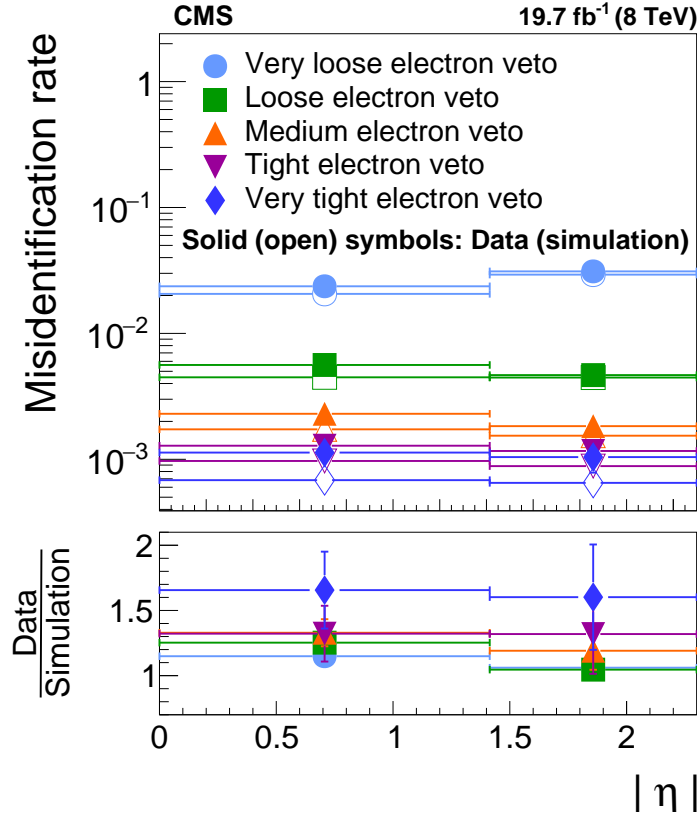


Figure 24: Probability for electrons in $Z/\gamma^* \rightarrow ee$ events to pass different WP of the discriminant against electrons. The $e \rightarrow \tau_h$ misidentification rates measured in data are compared to the MC expectation, separately for electrons in the barrel ($|\eta| < 1.46$) and in the endcap ($|\eta| > 1.56$) regions of the electromagnetic calorimeter.

12 Summary

The algorithms used by the CMS experiment for reconstruction and identification of hadronic τ decays in Run 1 data from the LHC have been presented, and their performance validated with proton-proton collision data recorded at $\sqrt{s} = 8$ TeV, corresponding to an integrated luminosity of 19.7 fb^{-1} .

The algorithms achieve a τ_h identification efficiency of typically 50–60%, and misidentification rates for quark and gluon jets, electrons, and muons that vary between the per mille and per cent level. The reconstruction of different τ_h decay modes and their energies is demonstrated to be robust against pileup.

The τ_h identification efficiency measured in the data agrees with the MC expectation within the uncertainty of the measurement of about 4.5%. The measured jet $\rightarrow \tau_h$ misidentification rates are about 20% higher than predicted for low- p_T jets and 20% lower for high- p_T jets. The probabilities for electrons and muons to pass the τ_h identification criteria, including dedicated discriminants that were developed to reduce the $e \rightarrow \tau_h$ and $\mu \rightarrow \tau_h$ misidentification rates, have been measured with a precision that ranges from a few % and 25%, for loose and tight working points, respectively. The measured misidentification rate for electrons exceeds the MC expectation by up to a factor 1.7.

The differences observed between data and MC simulation in the probabilities for jets, electrons, and muons to be misidentified as τ_h decays have been taken into account in physics

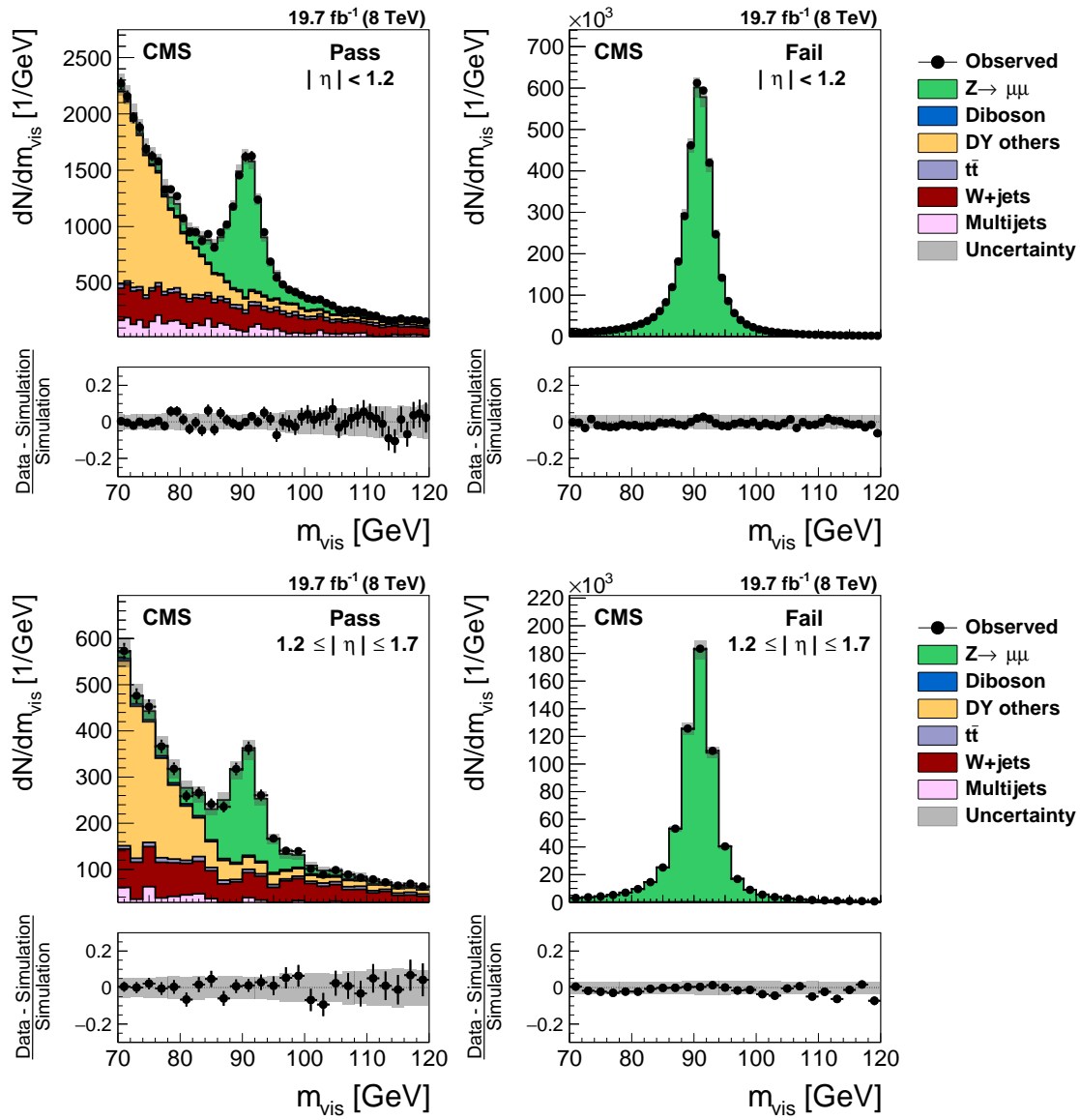


Figure 25: Distribution in the mass of the tag and probe pair in the pass (left) and fail (right) regions, for the loose WP of the cutoff-based muon discriminant in the region $|\eta| < 1.2$ (top) and $1.2 \leq |\eta| \leq 1.7$ (bottom). The distributions in $Z/\gamma^* \rightarrow \mu\mu$ candidate events selected in data are compared to the MC expectation, shown for the values of nuisance parameters obtained from the likelihood fit to the data, as described in Section 7.3. The contributions from $Z/\gamma^* \rightarrow \tau\tau$ background are denoted by “DY others”. The “Uncertainty” band represents the statistical and systematic uncertainties added in quadrature.

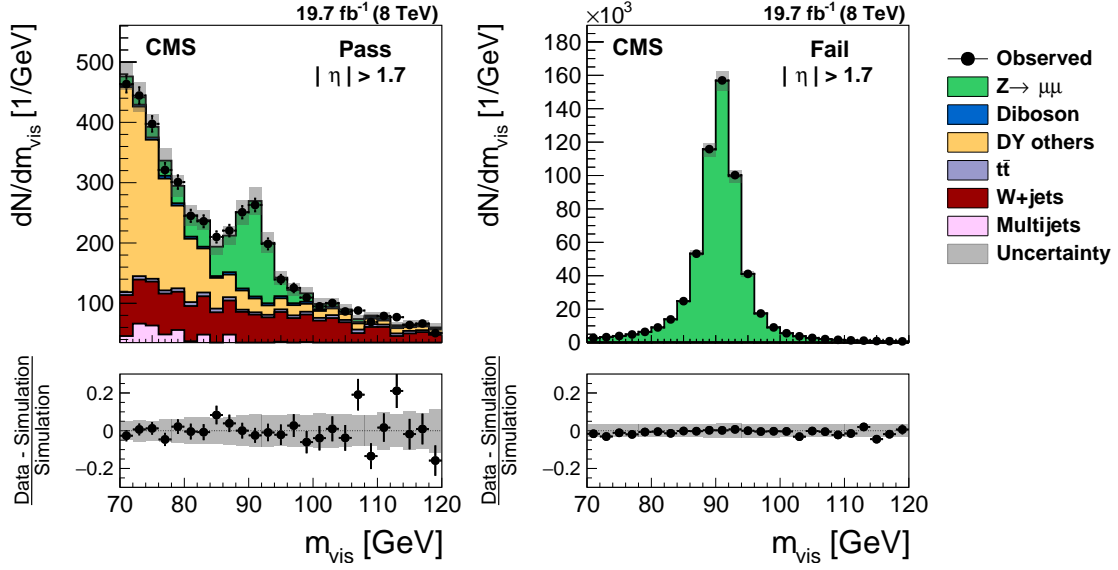


Figure 26: Distribution in the mass of the tag and probe pair in the pass (left) and fail (right) regions, for the loose WP of the cutoff-based muon discriminant in the region $|\eta| > 1.7$. The distributions in $Z/\gamma^* \rightarrow \mu\mu$ candidate events selected in data are compared to the MC expectation, shown for the values of nuisance parameters obtained from the likelihood fit to the data, as described in Section 7.3. The contributions from $Z/\gamma^* \rightarrow \tau\tau$ background are denoted by “DY others”. The “Uncertainty” band represents the statistical and systematic uncertainties added in quadrature.

analyses by applying appropriate MC-to-data correction factors.

The procedures developed for studying τ_h decays have provided a powerful tool for precision measurements as well as for the search for new phenomena beyond the standard model in Run 2 of the LHC.

Acknowledgments

We congratulate our colleagues in the CERN accelerator departments for the excellent performance of the LHC and thank the technical and administrative staffs at CERN and at other CMS institutes for their contributions to the success of the CMS effort. In addition, we gratefully acknowledge the computing centres and personnel of the Worldwide LHC Computing Grid for delivering so effectively the computing infrastructure essential to our analyses. Finally, we acknowledge the enduring support for the construction and operation of the LHC and the CMS detector provided by the following funding agencies: the Austrian Federal Ministry of Science, Research and Economy and the Austrian Science Fund; the Belgian Fonds de la Recherche Scientifique, and Fonds voor Wetenschappelijk Onderzoek; the Brazilian Funding Agencies (CNPq, CAPES, FAPERJ, and FAPESP); the Bulgarian Ministry of Education and Science; CERN; the Chinese Academy of Sciences, Ministry of Science and Technology, and National Natural Science Foundation of China; the Colombian Funding Agency (COLCIENCIAS); the Croatian Ministry of Science, Education and Sport, and the Croatian Science Foundation; the Research Promotion Foundation, Cyprus; the Ministry of Education and Research, Estonian Research Council via IUT23-4 and IUT23-6 and European Regional Development Fund, Estonia; the Academy of Finland, Finnish Ministry of Education and Culture, and Helsinki Institute of Physics; the Institut National de Physique Nucléaire et de Physique des Partic-

Table 7: Probability for muons to pass different WP of the cutoff-based and MVA-based discriminants against muons. The $\mu \rightarrow \tau_h$ misidentification rates measured in $Z/\gamma^* \rightarrow \mu\mu$ events are compared to the MC predictions in the regions $|\eta| < 1.2$, $1.2 \leq |\eta| \leq 1.7$, and $|\eta| > 1.7$.

WP	Simulation	Data	Data/Simulation
$ \eta < 1.2$			
Cutoff-based loose	$(2.48 \pm 0.02) \times 10^{-3}$	$(2.65 \pm 0.06) \times 10^{-3}$	1.07 ± 0.03
Cutoff-based tight	$(9.94 \pm 0.10) \times 10^{-4}$	$(1.05 \pm 0.05) \times 10^{-3}$	1.05 ± 0.05
MVA loose	$(4.28 \pm 0.09) \times 10^{-4}$	$(4.63 \pm 0.49) \times 10^{-4}$	1.08 ± 0.12
MVA medium	$(2.91 \pm 0.07) \times 10^{-4}$	$(3.08 \pm 0.50) \times 10^{-4}$	1.06 ± 0.17
MVA tight	$(2.56 \pm 0.07) \times 10^{-4}$	$(2.66 \pm 0.50) \times 10^{-4}$	1.04 ± 0.20
$1.2 \leq \eta \leq 1.7$			
Cutoff-based loose	$(1.64 \pm 0.03) \times 10^{-3}$	$(1.92 \pm 0.10) \times 10^{-3}$	1.17 ± 0.07
Cutoff-based tight	$(6.54 \pm 0.19) \times 10^{-4}$	$(8.33 \pm 0.81) \times 10^{-4}$	1.27 ± 0.13
MVA loose	$(5.61 \pm 0.18) \times 10^{-4}$	$(7.28 \pm 0.94) \times 10^{-4}$	1.30 ± 0.17
MVA medium	$(3.28 \pm 0.14) \times 10^{-4}$	$(5.05 \pm 0.97) \times 10^{-4}$	1.54 ± 0.30
MVA tight	$(2.63 \pm 0.12) \times 10^{-4}$	$(4.06 \pm 0.95) \times 10^{-4}$	1.54 ± 0.37
$ \eta > 1.7$			
Cutoff-based loose	$(9.85 \pm 0.30) \times 10^{-4}$	$(1.42 \pm 0.11) \times 10^{-3}$	1.45 ± 0.12
Cutoff-based tight	$(4.99 \pm 0.18) \times 10^{-4}$	$(7.42 \pm 1.09) \times 10^{-4}$	1.49 ± 0.22
MVA loose	$(4.66 \pm 0.17) \times 10^{-4}$	$(6.99 \pm 1.20) \times 10^{-4}$	1.50 ± 0.26
MVA medium	$(2.46 \pm 0.12) \times 10^{-4}$	$(4.57 \pm 0.92) \times 10^{-4}$	1.86 ± 0.38
MVA tight	$(1.95 \pm 0.11) \times 10^{-4}$	$(2.77 \pm 1.25) \times 10^{-4}$	1.42 ± 0.64

ules / CNRS, and Commissariat à l'Énergie Atomique et aux Énergies Alternatives / CEA, France; the Bundesministerium für Bildung und Forschung, Deutsche Forschungsgemeinschaft, and Helmholtz-Gemeinschaft Deutscher Forschungszentren, Germany; the General Secretariat for Research and Technology, Greece; the National Scientific Research Foundation, and National Innovation Office, Hungary; the Department of Atomic Energy and the Department of Science and Technology, India; the Institute for Studies in Theoretical Physics and Mathematics, Iran; the Science Foundation, Ireland; the Istituto Nazionale di Fisica Nucleare, Italy; the Ministry of Science, ICT and Future Planning, and National Research Foundation (NRF), Republic of Korea; the Lithuanian Academy of Sciences; the Ministry of Education, and University of Malaya (Malaysia); the Mexican Funding Agencies (CINVESTAV, CONACYT, SEP, and UASLP-FAI); the Ministry of Business, Innovation and Employment, New Zealand; the Pakistan Atomic Energy Commission; the Ministry of Science and Higher Education and the National Science Centre, Poland; the Fundação para a Ciência e a Tecnologia, Portugal; JINR, Dubna; the Ministry of Education and Science of the Russian Federation, the Federal Agency of Atomic Energy of the Russian Federation, Russian Academy of Sciences, and the Russian Foundation for Basic Research; the Ministry of Education, Science and Technological Development of Serbia; the Secretaría de Estado de Investigación, Desarrollo e Innovación and Programa Consolider-Ingenio 2010, Spain; the Swiss Funding Agencies (ETH Board, ETH Zurich, PSI, SNF, UniZH, Canton Zurich, and SER); the Ministry of Science and Technology, Taipei; the Thailand Center of Excellence in Physics, the Institute for the Promotion of Teaching Science and Technology of Thailand, Special Task Force for Activating Research and the National Science and Technology Development Agency of Thailand; the Scientific and Technical Research Council of Turkey, and Turkish Atomic Energy Authority; the National Academy of Sciences of Ukraine, and State Fund for Fundamental Researches, Ukraine; the Science and Technology Facilities Council, UK; the US Department of Energy, and the US National Science Foundation.

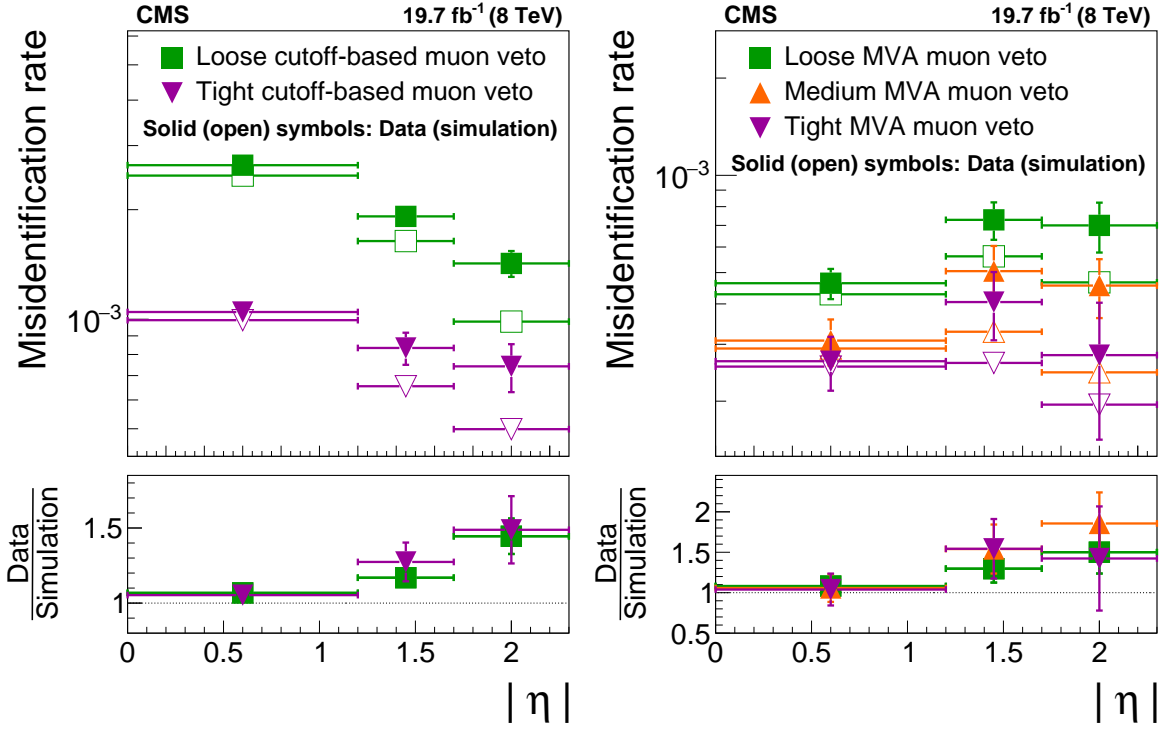


Figure 27: Probability for muons in $Z/\gamma^* \rightarrow \mu\mu$ events to pass different WP of the (left) cut-based and (right) MVA-based discriminants against muons. The $\mu \rightarrow \tau_h$ misidentification rates measured in data are compared to the MC simulation in the regions $|\eta| < 1.2$, $1.2 \leq |\eta| \leq 1.7$, and $|\eta| > 1.7$.

Individuals have received support from the Marie-Curie programme and the European Research Council and EPLANET (European Union); the Leventis Foundation; the A. P. Sloan Foundation; the Alexander von Humboldt Foundation; the Belgian Federal Science Policy Office; the Fonds pour la Formation à la Recherche dans l'Industrie et dans l'Agriculture (FRIA-Belgium); the Agentschap voor Innovatie door Wetenschap en Technologie (IWT-Belgium); the Ministry of Education, Youth and Sports (MEYS) of the Czech Republic; the Council of Science and Industrial Research, India; the HOMING PLUS programme of the Foundation for Polish Science, cofinanced from European Union, Regional Development Fund; the OPUS programme of the National Science Center (Poland); the Compagnia di San Paolo (Torino); the Consorzio per la Fisica (Trieste); MIUR project 20108T4XTM (Italy); the Thalís and Aristeia programmes cofinanced by EU-ESF and the Greek NSRF; the National Priorities Research Program by Qatar National Research Fund; the Rachadapisek Sompot Fund for Postdoctoral Fellowship, Chulalongkorn University (Thailand); and the Welch Foundation, contract C-1845.

References

- [1] CMS Collaboration, “Evidence for the 125 GeV Higgs boson decaying to a pair of τ leptons”, *JHEP* **05** (2014) 104, doi:10.1007/JHEP05(2014)104, arXiv:1401.5041.
- [2] ATLAS Collaboration, “Evidence for the Higgs-boson Yukawa coupling to tau leptons with the ATLAS detector”, *JHEP* **04** (2015) 117, doi:10.1007/JHEP04(2015)117, arXiv:1501.04943.

- [3] CMS Collaboration, “Search for neutral MSSM Higgs bosons decaying to τ pairs in pp collisions at $\sqrt{s} = 7$ TeV”, *Phys. Rev. Lett.* **106** (2011) 231801, doi:10.1103/PhysRevLett.106.231801, arXiv:1104.1619.
- [4] ATLAS Collaboration, “Search for neutral MSSM Higgs bosons decaying to $\tau^+\tau^-$ pairs in proton-proton collisions at $\sqrt{s} = 7$ TeV with the ATLAS detector”, *Phys. Lett. B* **705** (2011) 174, doi:10.1016/j.physletb.2011.10.001, arXiv:1107.5003.
- [5] CMS Collaboration, “Search for neutral MSSM Higgs bosons decaying to a pair of τ leptons in pp collisions”, *JHEP* **10** (2014) 160, doi:10.1007/JHEP10(2014)160, arXiv:1408.3316.
- [6] ATLAS Collaboration, “Search for neutral Higgs bosons of the minimal supersymmetric standard model in pp collisions at $\sqrt{s} = 8$ TeV with the ATLAS detector”, *JHEP* **11** (2014) 056, doi:10.1007/JHEP11(2014)056, arXiv:1409.6064.
- [7] CMS Collaboration, “Search for a light charged Higgs boson in top quark decays in pp collisions at $\sqrt{s} = 7$ TeV”, *JHEP* **07** (2012) 143, doi:10.1007/JHEP07(2012)143, arXiv:1205.5736.
- [8] ATLAS Collaboration, “Search for charged Higgs bosons decaying via $H^\pm \rightarrow \tau^\pm \nu$ in fully hadronic final states using pp collision data at $\sqrt{s} = 8$ TeV with the ATLAS detector”, *JHEP* **03** (2015) 088, doi:10.1007/JHEP03(2015)088, arXiv:1412.6663.
- [9] CMS Collaboration, “Measurement of the inclusive Z cross section via decays to τ pairs in pp collisions at $\sqrt{s} = 7$ TeV”, *JHEP* **08** (2011) 117, doi:10.1007/JHEP08(2011)117, arXiv:1104.1617.
- [10] CMS Collaboration, “Measurement of the top quark pair production cross section in pp collisions at $\sqrt{s} = 7$ TeV in dilepton final states containing a τ ”, *Phys. Rev. D* **85** (2012) 112007, doi:10.1103/PhysRevD.85.112007, arXiv:1203.6810.
- [11] CMS Collaboration, “Measurement of the $t\bar{t}$ production cross section in pp collisions at $\sqrt{s} = 8$ TeV in dilepton final states containing one τ lepton”, *Phys. Lett. B* **739** (2014) 23, doi:10.1016/j.physletb.2014.10.032, arXiv:1407.6643.
- [12] CMS Collaboration, “Search for physics beyond the standard model in events with τ leptons, jets, and large transverse momentum imbalance in pp collisions at $\sqrt{s} = 7$ TeV”, *Eur. Phys. J. C* **73** (2013) 2493, doi:10.1140/epjc/s10052-013-2493-8, arXiv:1301.3792.
- [13] CMS Collaboration, “Search for anomalous production of events with three or more leptons in pp collisions at $\sqrt{s} = 8$ TeV”, *Phys. Rev. D* **90** (2014) 032006, doi:10.1103/PhysRevD.90.032006, arXiv:1404.5801.
- [14] CMS Collaboration, “Search for top squarks in R-parity-violating supersymmetry using three or more leptons and b-tagged jets”, *Phys. Rev. Lett.* **111** (2013) 221801, doi:10.1103/PhysRevLett.111.221801, arXiv:1306.6643.
- [15] CMS Collaboration, “Search for pair production of third-generation leptoquarks and top squarks in pp collisions at $\sqrt{s} = 7$ TeV”, *Phys. Rev. Lett.* **110** (2013) 081801, doi:10.1103/PhysRevLett.110.081801, arXiv:1210.5629.

- [16] CMS Collaboration, “Search for high mass resonances decaying into τ lepton pairs in pp collisions at $\sqrt{s} = 7$ TeV”, *Phys. Lett. B* **716** (2012) 82, doi:10.1016/j.physletb.2012.07.062, arXiv:1206.1725.
- [17] CMS Collaboration, “A search for a doubly-charged Higgs boson in pp collisions at $\sqrt{s} = 7$ TeV”, *Eur. Phys. J. C* **72** (2012) 2189, doi:10.1140/epjc/s10052-012-2189-5, arXiv:1207.2666.
- [18] Particle Data Group, “Review of particle physics”, *Chin. Phys. C* **38** (2014) 090001, doi:10.1088/1674-1137/38/9/090001.
- [19] CMS Collaboration, “The CMS experiment at the CERN LHC”, *JINST* **3** (2008) S08004, doi:10.1088/1748-0221/3/08/S08004.
- [20] CMS Collaboration, “Performance of τ -lepton reconstruction and identification in CMS”, *JINST* **7** (2012) P01001, doi:10.1088/1748-0221/7/01/P01001, arXiv:1109.6034.
- [21] CMS Collaboration, “Description and performance of track and primary-vertex reconstruction with the CMS tracker”, *JINST* **9** (2014) P10009, doi:10.1088/1748-0221/9/10/P10009, arXiv:1405.6569.
- [22] J. Alwall et al., “The automated computation of tree-level and next-to-leading order differential cross sections, and their matching to parton shower simulations”, *JHEP* **07** (2014) 079, doi:10.1007/JHEP07(2014)079, arXiv:1405.0301.
- [23] P. Nason, “A new method for combining NLO QCD with shower Monte Carlo algorithms”, *JHEP* **11** (2004) 040, doi:10.1088/1126-6708/2004/11/040, arXiv:hep-ph/0409146.
- [24] S. Frixione, P. Nason, and C. Oleari, “Matching NLO QCD computations with parton shower simulations: the POWHEG method”, *JHEP* **11** (2007) 070, doi:10.1088/1126-6708/2007/11/070, arXiv:0709.2092.
- [25] S. Alioli, P. Nason, C. Oleari, and E. Re, “A general framework for implementing NLO calculations in shower Monte Carlo programs: the POWHEG BOX”, *JHEP* **06** (2010) 043, doi:10.1007/JHEP06(2010)043, arXiv:1002.2581.
- [26] T. Sjöstrand, S. Mrenna, and P. Z. Skands, “PYTHIA 6.4 physics and manual”, *JHEP* **05** (2006) 026, doi:10.1088/1126-6708/2006/05/026, arXiv:hep-ph/0603175.
- [27] R. Field, “Early LHC underlying event data - findings and surprises”, in *Hadron collider physics. Proceedings, 22nd Conference, HCP 2010, Toronto, Canada, August 23-27, 2010*. 2010. arXiv:1010.3558.
- [28] J. Pumplin et al., “New generation of parton distributions with uncertainties from global QCD analysis”, *JHEP* **07** (2002) 012, doi:10.1088/1126-6708/2002/07/012, arXiv:hep-ph/0201195.
- [29] S. Jadach, Z. Was, R. Decker, and J. H. Kühn, “The τ decay library TAUOLA, version 2.4”, *Comput. Phys. Commun.* **76** (1993) 361, doi:10.1016/0010-4655(93)90061-G.
- [30] K. Melnikov and F. Petriello, “Electroweak gauge boson production at hadron colliders through $O(\alpha_s^2)$ ”, *Phys. Rev. D* **74** (2006) 114017, doi:10.1103/PhysRevD.74.114017, arXiv:hep-ph/0609070.

- [31] CMS Collaboration, “Measurement of the $t\bar{t}$ production cross section in the dilepton channel in pp collisions at $\sqrt{s} = 8$ TeV”, *JHEP* **02** (2014) 024, doi:10.1007/JHEP02(2014)024, arXiv:1312.7582. [Erratum: doi:10.1007/JHEP02(2014)102].
- [32] CMS Collaboration, “Measurement of differential top-quark pair production cross sections in pp collisions at $\sqrt{s} = 7$ TeV”, *Eur. Phys. J. C* **73** (2013) 2339, doi:10.1140/epjc/s10052-013-2339-4, arXiv:1211.2220.
- [33] CMS Collaboration, “Measurement of the differential cross section for top quark pair production in pp collisions at $\sqrt{s} = 8$ TeV”, (2015). arXiv:1505.04480.
- [34] J. M. Campbell, R. K. Ellis, and C. Williams, “Vector boson pair production at the LHC”, *JHEP* **07** (2011) 018, doi:10.1007/JHEP07(2011)018, arXiv:1105.0020.
- [35] M. Cacciari, G. P. Salam, and G. Soyez, “The anti- k_t jet clustering algorithm”, *JHEP* **04** (2008) 063, doi:10.1088/1126-6708/2008/04/063, arXiv:0802.1189.
- [36] GEANT4 Collaboration, “GEANT4—a simulation toolkit”, *Nucl. Instrum. Meth. A* **506** (2003) 250, doi:10.1016/S0168-9002(03)01368-8.
- [37] CMS Collaboration, “Performance of the CMS missing transverse momentum reconstruction in pp data at $\sqrt{s} = 8$ TeV”, *JINST* **10** (2015) P02006, doi:10.1088/1748-0221/10/02/P02006, arXiv:1411.0511.
- [38] CMS Collaboration, “Particle-flow event reconstruction in CMS and performance for jets, taus, and E_T^{miss} ”, CMS Physics Analysis Summary CMS-PAS-PFT-09-001, 2009.
- [39] CMS Collaboration, “Commissioning of the particle-flow event reconstruction with the first LHC collisions recorded in the CMS detector”, CMS Physics Analysis Summary CMS-PAS-PFT-10-001, 2010.
- [40] CMS Collaboration, “Commissioning of the particle-flow reconstruction in minimum-bias and jet events from pp collisions at 7 TeV”, CMS Physics Analysis Summary CMS-PAS-PFT-10-002, 2010.
- [41] CMS Collaboration, “Particle-flow commissioning with muons and electrons from J/Ψ and W events at 7 TeV”, CMS Physics Analysis Summary CMS-PAS-PFT-10-003, 2010.
- [42] S. Baffioni et al., “Electron reconstruction in CMS”, *Eur. Phys. J. C* **49** (2007) 1099, doi:10.1140/epjc/s10052-006-0175-5.
- [43] W. Adam, R. Frühwirth, A. Strandlie, and T. Todorov, “Reconstruction of electrons with the Gaussian sum filter in the CMS tracker at LHC”, *J. Phys. G: Nucl. Part. Phys.* **31** (2003) N9, doi:10.1088/0954-3899/31/9/N01, arXiv:physics/0306087.
- [44] H. Voss, A. Höcker, J. Stelzer, and F. Tegenfeldt, “TMVA, the Toolkit for Multivariate Data Analysis with ROOT”, in *XIth International Workshop on Advanced Computing and Analysis Techniques in Physics Research (ACAT)*, p. 40. 2007. arXiv:physics/0703039.
- [45] CMS Collaboration, “Performance of electron reconstruction and selection with the CMS detector in proton-proton collisions at $\sqrt{s} = 8$ TeV”, *JINST* **10** (2015) P06005, doi:10.1088/1748-0221/10/06/P06005, arXiv:1502.02701.

- [46] CMS Collaboration, “Performance of CMS muon reconstruction in pp collision events at $\sqrt{s} = 7$ TeV”, *JINST* **7** (2012) P10002, doi:10.1088/1748-0221/7/10/P10002, arXiv:1206.4071.
- [47] E. Chabanat and N. Estre, “Deterministic annealing for vertex finding at CMS”, in *Computing in high energy physics and nuclear physics. Proceedings, Conference, CHEP’04, Interlaken, Switzerland, September 27-October 1, 2004*, p. 287. 2005.
- [48] W. Waltenberger, R. Frühwirth, and P. Vanlaer, “Adaptive vertex fitting”, *J. Phys. G: Nucl. Part. Phys.* **34** (2007) N343, doi:10.1088/0954-3899/34/12/N01.
- [49] CMS Collaboration, “Jet performance in pp collisions at $\sqrt{s} = 7$ TeV”, CMS Physics Analysis Summary CMS-PAS-JME-10-003, 2010.
- [50] CMS Collaboration, “Pileup jet identification”, CMS Physics Analysis Summary CMS-PAS-JME-13-005, 2013.
- [51] CMS Collaboration, “Determination of jet energy calibration and transverse momentum resolution in CMS”, *JINST* **6** (2011) P11002, doi:10.1088/1748-0221/6/11/P11002, arXiv:1107.4277.
- [52] M. Cacciari, G. P. Salam, and G. Soyez, “The catchment area of jets”, *JHEP* **04** (2008) 005, doi:10.1088/1126-6708/2008/04/005, arXiv:0802.1188.
- [53] M. Cacciari and G. P. Salam, “Pileup subtraction using jet areas”, *Phys. Lett. B* **659** (2008) 119, doi:10.1016/j.physletb.2007.09.077, arXiv:0707.1378.
- [54] CMS Collaboration, “Identification of b quark jets with the CMS experiment”, *JINST* **8** (2013) P04013, doi:10.1088/1748-0221/8/04/P04013, arXiv:1211.4462.
- [55] CMS Collaboration, “Performance of b tagging at $\sqrt{s} = 8$ TeV in multijet, $t\bar{t}$ and boosted topology events”, CMS Physics Analysis Summary CMS-PAS-BTV-13-001, 2013.
- [56] CMS Collaboration, “Measurement of the inclusive W and Z production cross sections in pp collisions at $\sqrt{s} = 7$ TeV”, *JHEP* **10** (2011) 132, doi:10.1007/JHEP10(2011)132, arXiv:1107.4789.
- [57] CMS Collaboration, “CMS luminosity based on pixel cluster counting – summer 2013 update”, CMS Physics Analysis Summary CMS-PAS-LUM-13-001, 2013.
- [58] S. Alekhin et al., “The PDF4LHC Working Group interim report”, (2011). arXiv:1101.0536.
- [59] PDF4LHC Working Group, M. Botje et al., “The PDF4LHC Working Group interim recommendations”, (2011). arXiv:1101.0538.
- [60] ATLAS and CMS Collaborations and LHC Higgs Combination Group, “Procedure for the LHC Higgs boson search combination in summer 2011”, Technical Report ATL-PHYS-PUB-2011-011, CMS-NOTE-2011-005, 2011.
- [61] CMS Collaboration, “Combined results of searches for the standard model Higgs boson in pp collisions at $\sqrt{s} = 7$ TeV”, *Phys. Lett. B* **710** (2012) 26, doi:10.1016/j.physletb.2012.02.064, arXiv:1202.1488.

- [62] J. S. Conway, “Incorporating nuisance parameters in likelihoods for multisource spectra”, in *Proceedings, PHYSTAT 2011 workshop on statistical issues related to discovery claims in search experiments and unfolding*, CERN, Geneva, Switzerland 17-20 January, 2011. 2011. arXiv:1103.0354.
- [63] R. J. Barlow and C. Beeston, “Fitting using finite Monte Carlo samples”, *Comput. Phys. Commun.* **77** (1993) 219, doi:10.1016/0010-4655(93)90005-W.
- [64] CDF Collaboration, “Search for neutral MSSM Higgs bosons decaying to τ pairs in $p\bar{p}$ collisions at $\sqrt{s} = 1.96$ TeV”, *Phys. Rev. Lett.* **96** (2006) 011802, doi:10.1103/PhysRevLett.96.011802, arXiv:hep-ex/0508051.
- [65] P. Adzic et al., “Reconstruction of the signal amplitude of the CMS electromagnetic calorimeter”, *Eur. Phys. J. C* **46** (2006) 23, doi:10.1140/epjcd/s2006-02-002-x.

A The CMS Collaboration

Yerevan Physics Institute, Yerevan, Armenia

V. Khachatryan, A.M. Sirunyan, A. Tumasyan

Institut für Hochenergiephysik der OeAW, Wien, Austria

W. Adam, E. Asilar, T. Bergauer, J. Brandstetter, E. Brondolin, M. Dragicevic, J. Erö, M. Flechl, M. Friedl, R. Frühwirth¹, V.M. Ghete, C. Hartl, N. Hörmann, J. Hrubec, M. Jeitler¹, V. Knünz, A. König, M. Krammer¹, I. Krätschmer, D. Liko, T. Matsushita, I. Mikulec, D. Rabady², B. Rahbaran, H. Rohringer, J. Schieck¹, R. Schöffbeck, J. Strauss, W. Treberer-Treberspurg, W. Waltenberger, C.-E. Wulz¹

National Centre for Particle and High Energy Physics, Minsk, Belarus

V. Mossolov, N. Shumeiko, J. Suarez Gonzalez

Universiteit Antwerpen, Antwerpen, Belgium

S. Alderweireldt, T. Cornelis, E.A. De Wolf, X. Janssen, A. Knutsson, J. Lauwers, S. Luyckx, S. Ochesanu, R. Rougny, M. Van De Klundert, H. Van Haevermaet, P. Van Mechelen, N. Van Remortel, A. Van Spilbeeck

Vrije Universiteit Brussel, Brussel, Belgium

S. Abu Zeid, F. Blekman, J. D'Hondt, N. Daci, I. De Bruyn, K. Deroover, N. Heracleous, J. Keaveney, S. Lowette, L. Moreels, A. Olbrechts, Q. Python, D. Strom, S. Tavernier, W. Van Doninck, P. Van Mulders, G.P. Van Onsem, I. Van Parijs

Université Libre de Bruxelles, Bruxelles, Belgium

P. Barria, H. Brun, C. Caillol, B. Clerbaux, G. De Lentdecker, H. Delannoy, G. Fasanella, L. Favart, A.P.R. Gay, A. Grebenyuk, G. Karapostoli, T. Lenzi, A. Léonard, T. Maerschalk, A. Marinov, L. Perniè, A. Randle-conde, T. Reis, T. Seva, C. Vander Velde, P. Vanlaer, R. Yonamine, F. Zenoni, F. Zhang³

Ghent University, Ghent, Belgium

K. Beernaert, L. Benucci, A. Cimmino, S. Crucy, D. Dobur, A. Fagot, G. Garcia, M. Gul, J. Mccartin, A.A. Ocampo Rios, D. Poyraz, D. Ryckbosch, S. Salva, M. Sigamani, N. Strobbe, M. Tytgat, W. Van Driessche, E. Yazgan, N. Zaganidis

Université Catholique de Louvain, Louvain-la-Neuve, Belgium

S. Basegmez, C. Beluffi⁴, O. Bondu, S. Brochet, G. Bruno, R. Castello, A. Caudron, L. Ceard, G.G. Da Silveira, C. Delaere, D. Favart, L. Forthomme, A. Giammanco⁵, J. Hollar, A. Jafari, P. Jez, M. Komm, V. Lemaitre, A. Mertens, C. Nuttens, L. Perrini, A. Pin, K. Piotrkowski, A. Popov⁶, L. Quertenmont, M. Selvaggi, M. Vidal Marono

Université de Mons, Mons, Belgium

N. Beliy, G.H. Hammad

Centro Brasileiro de Pesquisas Fisicas, Rio de Janeiro, Brazil

W.L. Aldá Júnior, G.A. Alves, L. Brito, M. Correa Martins Junior, M. Hamer, C. Hensel, C. Mora Herrera, A. Moraes, M.E. Pol, P. Rebello Teles

Universidade do Estado do Rio de Janeiro, Rio de Janeiro, Brazil

E. Belchior Batista Das Chagas, W. Carvalho, J. Chinellato⁷, A. Custódio, E.M. Da Costa, D. De Jesus Damiao, C. De Oliveira Martins, S. Fonseca De Souza, L.M. Huertas Guativa, H. Malbouisson, D. Matos Figueiredo, L. Mundim, H. Nogima, W.L. Prado Da Silva, A. Santoro, A. Sznajder, E.J. Tonelli Manganote⁷, A. Vilela Pereira

Universidade Estadual Paulista ^a, Universidade Federal do ABC ^b, São Paulo, Brazil

S. Ahuja^a, C.A. Bernardes^b, A. De Souza Santos^b, S. Dogra^a, T.R. Fernandez Perez Tomei^a, E.M. Gregores^b, P.G. Mercadante^b, C.S. Moon^{a,8}, S.F. Novaes^a, Sandra S. Padula^a, D. Romero Abad, J.C. Ruiz Vargas

Institute for Nuclear Research and Nuclear Energy, Sofia, Bulgaria

A. Aleksandrov, R. Hadjiiska, P. Iaydjiev, M. Rodozov, S. Stoykova, G. Sultanov, M. Vutova

University of Sofia, Sofia, Bulgaria

A. Dimitrov, I. Glushkov, L. Litov, B. Pavlov, P. Petkov

Institute of High Energy Physics, Beijing, China

M. Ahmad, J.G. Bian, G.M. Chen, H.S. Chen, M. Chen, T. Cheng, R. Du, C.H. Jiang, R. Plestina⁹, F. Romeo, S.M. Shaheen, J. Tao, C. Wang, Z. Wang, H. Zhang

State Key Laboratory of Nuclear Physics and Technology, Peking University, Beijing, China

C. Asawatrangkuldee, Y. Ban, Q. Li, S. Liu, Y. Mao, S.J. Qian, D. Wang, Z. Xu, W. Zou

Universidad de Los Andes, Bogota, Colombia

C. Avila, A. Cabrera, L.F. Chaparro Sierra, C. Florez, J.P. Gomez, B. Gomez Moreno, J.C. Sanabria

University of Split, Faculty of Electrical Engineering, Mechanical Engineering and Naval Architecture, Split, Croatia

N. Godinovic, D. Lelas, I. Puljak, P.M. Ribeiro Cipriano

University of Split, Faculty of Science, Split, Croatia

Z. Antunovic, M. Kovac

Institute Rudjer Boskovic, Zagreb, Croatia

V. Brigljevic, K. Kadija, J. Luetic, S. Micanovic, L. Sudic

University of Cyprus, Nicosia, Cyprus

A. Attikis, G. Mavromanolakis, J. Mousa, C. Nicolaou, F. Ptochos, P.A. Razis, H. Rykaczewski

Charles University, Prague, Czech Republic

M. Bodlak, M. Finger¹⁰, M. Finger Jr.¹⁰

Academy of Scientific Research and Technology of the Arab Republic of Egypt, Egyptian Network of High Energy Physics, Cairo, Egypt

A.A. Abdelalim^{11,12}, A. Awad^{13,14}, M. El Sawy^{15,14}, A. Mahrous¹¹, Y. Mohammed¹⁶, A. Radi^{14,13}

National Institute of Chemical Physics and Biophysics, Tallinn, Estonia

B. Calpas, M. Kadastik, M. Murumaa, M. Raidal, A. Tiko, C. Veelken

Department of Physics, University of Helsinki, Helsinki, Finland

P. Eerola, J. Pekkanen, M. Voutilainen

Helsinki Institute of Physics, Helsinki, Finland

J. Härkönen, V. Karimäki, R. Kinnunen, T. Lampén, K. Lassila-Perini, S. Lehti, T. Lindén, P. Luukka, T. Mäenpää, T. Peltola, E. Tuominen, J. Tuominiemi, E. Tuovinen, L. Wendland

Lappeenranta University of Technology, Lappeenranta, Finland

J. Talvitie, T. Tuuva

DSM/IRFU, CEA/Saclay, Gif-sur-Yvette, France

M. Besancon, F. Couderc, M. Dejardin, D. Denegri, B. Fabbro, J.L. Faure, C. Favaro, F. Ferri,

S. Ganjour, A. Givernaud, P. Gras, G. Hamel de Monchenault, P. Jarry, E. Locci, M. Machet, J. Malcles, J. Rander, A. Rosowsky, M. Titov, A. Zghiche

Laboratoire Leprince-Ringuet, Ecole Polytechnique, IN2P3-CNRS, Palaiseau, France

I. Antropov, S. Baffioni, F. Beaudette, P. Busson, L. Cadamuro, E. Chapon, C. Charlot, T. Dahms, O. Davignon, N. Filipovic, A. Florent, R. Granier de Cassagnac, S. Lisniak, L. Mastrolorenzo, P. Miné, I.N. Naranjo, M. Nguyen, C. Ochando, G. Ortona, P. Paganini, P. Pigard, S. Regnard, R. Salerno, J.B. Sauvan, Y. Sirois, T. Strebler, Y. Yilmaz, A. Zabi

Institut Pluridisciplinaire Hubert Curien, Université de Strasbourg, Université de Haute Alsace Mulhouse, CNRS/IN2P3, Strasbourg, France

J.-L. Agram¹⁷, J. Andrea, A. Aubin, D. Bloch, J.-M. Brom, M. Buttignol, E.C. Chabert, N. Chanon, C. Collard, E. Conte¹⁷, X. Coubez, J.-C. Fontaine¹⁷, D. Gelé, U. Goerlach, C. Goetzmann, A.-C. Le Bihan, J.A. Merlin², K. Skovpen, P. Van Hove

Centre de Calcul de l'Institut National de Physique Nucleaire et de Physique des Particules, CNRS/IN2P3, Villeurbanne, France

S. Gadrat

Université de Lyon, Université Claude Bernard Lyon 1, CNRS-IN2P3, Institut de Physique Nucléaire de Lyon, Villeurbanne, France

S. Beauceron, C. Bernet, G. Boudoul, E. Bouvier, C.A. Carrillo Montoya, R. Chierici, D. Contardo, B. Courbon, P. Depasse, H. El Mamouni, J. Fan, J. Fay, S. Gascon, M. Gouzevitch, B. Ille, F. Lagarde, I.B. Laktineh, M. Lethuillier, L. Mirabito, A.L. Pequegnot, S. Perries, J.D. Ruiz Alvarez, D. Sabes, L. Sgandurra, V. Sordini, M. Vander Donckt, P. Verdier, S. Viret, H. Xiao

Tbilisi State University, Tbilisi, Georgia

Z. Tsamalaidze¹⁰

RWTH Aachen University, I. Physikalisches Institut, Aachen, Germany

C. Autermann, S. Beranek, M. Edelhoff, L. Feld, A. Heister, M.K. Kiesel, K. Klein, M. Lipinski, A. Ostapchuk, M. Preuten, F. Raupach, S. Schael, J.F. Schulte, T. Verlage, H. Weber, B. Wittmer, V. Zhukov⁶

RWTH Aachen University, III. Physikalisches Institut A, Aachen, Germany

M. Ata, M. Brodski, E. Dietz-Laursonn, D. Duchardt, M. Endres, M. Erdmann, S. Erdweg, T. Esch, R. Fischer, A. Güth, T. Hebbeker, C. Heidemann, K. Hoepfner, D. Klingebiel, S. Knutzen, P. Kreuzer, M. Merschmeyer, A. Meyer, P. Millet, M. Olschewski, K. Padeken, P. Papacz, T. Pook, M. Radziej, H. Reithler, M. Rieger, F. Scheuch, L. Sonnenschein, D. Teyssier, S. Thüer

RWTH Aachen University, III. Physikalisches Institut B, Aachen, Germany

V. Cherepanov, Y. Erdogan, G. Flügge, H. Geenen, M. Geisler, F. Hoehle, B. Kargoll, T. Kress, Y. Kuessel, A. Künsken, J. Lingemann², A. Nehr Korn, A. Nowack, I.M. Nugent, C. Pistone, O. Pooth, A. Stahl

Deutsches Elektronen-Synchrotron, Hamburg, Germany

M. Aldaya Martin, I. Asin, N. Bartosik, O. Behnke, U. Behrens, A.J. Bell, K. Borras, A. Burgmeier, A. Cakir, L. Calligaris, A. Campbell, S. Choudhury, F. Costanza, C. Diez Pardos, G. Dolinska, S. Dooling, T. Dorland, G. Eckerlin, D. Eckstein, T. Eichhorn, G. Flucke, E. Gallo¹⁸, J. Garay Garcia, A. Geiser, A. Gizhko, P. Gunnellini, J. Hauk, M. Hempel¹⁹, H. Jung, A. Kalogeropoulos, O. Karacheban¹⁹, M. Kasemann, P. Katsas, J. Kieseler, C. Kleinwort, I. Korol, W. Lange, J. Leonard, K. Lipka, A. Lobanov, W. Lohmann¹⁹, R. Mankel, I. Marfin¹⁹, I.-A. Melzer-Pellmann, A.B. Meyer, G. Mittag, J. Mnich, A. Mussgiller, S. Naumann-Emme, A. Nayak,

E. Ntomari, H. Perrey, D. Pitzl, R. Placakyte, A. Raspereza, B. Roland, M.Ö. Sahin, P. Saxena, T. Schoerner-Sadenius, M. Schröder, C. Seitz, S. Spannagel, K.D. Trippkewitz, R. Walsh, C. Wissing

University of Hamburg, Hamburg, Germany

V. Blobel, M. Centis Vignali, A.R. Draeger, J. Erfle, E. Garutti, K. Goebel, D. Gonzalez, M. Görner, J. Haller, M. Hoffmann, R.S. Höing, A. Junkes, R. Klanner, R. Kogler, T. Lapsien, T. Lenz, I. Marchesini, D. Marconi, M. Meyer, D. Nowatschin, J. Ott, F. Pantaleo², T. Peiffer, A. Perieanu, N. Pietsch, J. Poehlsen, D. Rathjens, C. Sander, H. Schettler, P. Schleper, E. Schlieckau, A. Schmidt, J. Schwandt, M. Seidel, V. Sola, H. Stadie, G. Steinbrück, H. Tholen, D. Troendle, E. Usai, L. Vanelderen, A. Vanhoefer, B. Vormwald

Institut für Experimentelle Kernphysik, Karlsruhe, Germany

M. Akbiyik, C. Barth, C. Baus, J. Berger, C. Böser, E. Butz, T. Chwalek, F. Colombo, W. De Boer, A. Descroix, A. Dierlamm, S. Fink, F. Frensch, M. Giffels, A. Gilbert, F. Hartmann², S.M. Heindl, U. Husemann, I. Katkov⁶, A. Kornmayer², P. Lobelle Pardo, B. Maier, H. Mildner, M.U. Mozer, T. Müller, Th. Müller, M. Plagge, G. Quast, K. Rabbertz, S. Röcker, F. Roscher, H.J. Simonis, F.M. Stober, R. Ulrich, J. Wagner-Kuhr, S. Wayand, M. Weber, T. Weiler, C. Wöhrmann, R. Wolf

Institute of Nuclear and Particle Physics (INPP), NCSR Demokritos, Aghia Paraskevi, Greece

G. Anagnostou, G. Daskalakis, T. Gerasis, V.A. Giakoumopoulou, A. Kyriakis, D. Loukas, A. Psallidas, I. Topsis-Giotis

University of Athens, Athens, Greece

A. Agapitos, S. Kesisoglou, A. Panagiotou, N. Saoulidou, E. Tziaferi

University of Ioánnina, Ioánnina, Greece

I. Evangelou, G. Flouris, C. Foudas, P. Kokkas, N. Loukas, N. Manthos, I. Papadopoulos, E. Paradas, J. Strologas

Wigner Research Centre for Physics, Budapest, Hungary

G. Bencze, C. Hajdu, A. Hazi, P. Hidas, D. Horvath²⁰, F. Sikler, V. Veszpremi, G. Vesztergombi²¹, A.J. Zsigmond

Institute of Nuclear Research ATOMKI, Debrecen, Hungary

N. Beni, S. Czellar, J. Karancsi²², J. Molnar, Z. Szillasi

University of Debrecen, Debrecen, Hungary

M. Bartók²³, A. Makovec, P. Raics, Z.L. Trocsanyi, B. Ujvari

National Institute of Science Education and Research, Bhubaneswar, India

P. Mal, K. Mandal, N. Sahoo, S.K. Swain

Panjab University, Chandigarh, India

S. Bansal, S.B. Beri, V. Bhatnagar, R. Chawla, R. Gupta, U. Bhawandeep, A.K. Kalsi, A. Kaur, M. Kaur, R. Kumar, A. Mehta, M. Mittal, J.B. Singh, G. Walia

University of Delhi, Delhi, India

Ashok Kumar, A. Bhardwaj, B.C. Choudhary, R.B. Garg, A. Kumar, S. Malhotra, M. Naimuddin, N. Nishu, K. Ranjan, R. Sharma, V. Sharma

Saha Institute of Nuclear Physics, Kolkata, India

S. Banerjee, S. Bhattacharya, K. Chatterjee, S. Dey, S. Dutta, Sa. Jain, N. Majumdar, A. Modak,

K. Mondal, S. Mukherjee, S. Mukhopadhyay, A. Roy, D. Roy, S. Roy Chowdhury, S. Sarkar, M. Sharan

Bhabha Atomic Research Centre, Mumbai, India

A. Abdulsalam, R. Chudasama, D. Dutta, V. Jha, V. Kumar, A.K. Mohanty², L.M. Pant, P. Shukla, A. Topkar

Tata Institute of Fundamental Research, Mumbai, India

T. Aziz, S. Banerjee, S. Bhowmik²⁴, R.M. Chatterjee, R.K. Dewanjee, S. Dugad, S. Ganguly, S. Ghosh, M. Guchait, A. Gurtu²⁵, G. Kole, S. Kumar, B. Mahakud, M. Maity²⁴, G. Majumder, K. Mazumdar, S. Mitra, G.B. Mohanty, B. Parida, T. Sarkar²⁴, K. Sudhakar, N. Sur, B. Sutar, N. Wickramage²⁶

Indian Institute of Science Education and Research (IISER), Pune, India

S. Chauhan, S. Dube, S. Sharma

Institute for Research in Fundamental Sciences (IPM), Tehran, Iran

H. Bakhshiansohi, H. Behnamian, S.M. Etesami²⁷, A. Fahim²⁸, R. Goldouzian, M. Khakzad, M. Mohammadi Najafabadi, M. Naseri, S. Paktinat Mehdiabadi, F. Rezaei Hosseinabadi, B. Safarzadeh²⁹, M. Zeinali

University College Dublin, Dublin, Ireland

M. Felcini, M. Grunewald

INFN Sezione di Bari ^a, Università di Bari ^b, Politecnico di Bari ^c, Bari, Italy

M. Abbrescia^{a,b}, C. Calabria^{a,b}, C. Caputo^{a,b}, A. Colaleo^a, D. Creanza^{a,c}, L. Cristella^{a,b}, N. De Filippis^{a,c}, M. De Palma^{a,b}, L. Fiore^a, G. Iaselli^{a,c}, G. Maggi^{a,c}, M. Maggi^a, G. Miniello^{a,b}, S. My^{a,c}, S. Nuzzo^{a,b}, A. Pompili^{a,b}, G. Pugliese^{a,c}, R. Radogna^{a,b}, A. Ranieri^a, G. Selvaggi^{a,b}, L. Silvestris^{a,2}, R. Venditti^{a,b}, P. Verwilligen^a

INFN Sezione di Bologna ^a, Università di Bologna ^b, Bologna, Italy

G. Abbiendi^a, C. Battilana², A.C. Benvenuti^a, D. Bonacorsi^{a,b}, S. Braibant-Giacomelli^{a,b}, L. Brigliadori^{a,b}, R. Campanini^{a,b}, P. Capiluppi^{a,b}, A. Castro^{a,b}, F.R. Cavallo^a, S.S. Chhibra^{a,b}, G. Codispoti^{a,b}, M. Cuffiani^{a,b}, G.M. Dallavalle^a, F. Fabbri^a, A. Fanfani^{a,b}, D. Fasanella^{a,b}, P. Giacomelli^a, C. Grandi^a, L. Guiducci^{a,b}, S. Marcellini^a, G. Masetti^a, A. Montanari^a, F.L. Navarria^{a,b}, A. Perrotta^a, A.M. Rossi^{a,b}, T. Rovelli^{a,b}, G.P. Siroli^{a,b}, N. Tosi^{a,b}, R. Travaglini^{a,b}

INFN Sezione di Catania ^a, Università di Catania ^b, Catania, Italy

G. Cappello^a, M. Chiorboli^{a,b}, S. Costa^{a,b}, F. Giordano^{a,b}, R. Potenza^{a,b}, A. Tricomi^{a,b}, C. Tuve^{a,b}

INFN Sezione di Firenze ^a, Università di Firenze ^b, Firenze, Italy

G. Barbagli^a, V. Ciulli^{a,b}, C. Civinini^a, R. D'Alessandro^{a,b}, E. Focardi^{a,b}, S. Gonzi^{a,b}, V. Gori^{a,b}, P. Lenzi^{a,b}, M. Meschini^a, S. Paoletti^a, G. Sguazzoni^a, A. Tropiano^{a,b}, L. Viliani^{a,b}

INFN Laboratori Nazionali di Frascati, Frascati, Italy

L. Benussi, S. Bianco, F. Fabbri, D. Piccolo, F. Primavera

INFN Sezione di Genova ^a, Università di Genova ^b, Genova, Italy

V. Calvelli^{a,b}, F. Ferro^a, M. Lo Vetere^{a,b}, M.R. Monge^{a,b}, E. Robutti^a, S. Tosi^{a,b}

INFN Sezione di Milano-Bicocca ^a, Università di Milano-Bicocca ^b, Milano, Italy

L. Brianza, M.E. Dinardo^{a,b}, S. Fiorendi^{a,b}, S. Gennai^a, R. Gerosa^{a,b}, A. Ghezzi^{a,b}, P. Govoni^{a,b}, S. Malvezzi^a, R.A. Manzoni^{a,b}, B. Marzocchi^{a,b,2}, D. Menasce^a, L. Moroni^a, M. Paganoni^{a,b}, D. Pedrini^a, S. Ragazzi^{a,b}, N. Redaelli^a, T. Tabarelli de Fatis^{a,b}

INFN Sezione di Napoli ^a, Università di Napoli 'Federico II' ^b, Napoli, Italy, Università della Basilicata ^c, Potenza, Italy, Università G. Marconi ^d, Roma, Italy

S. Buontempo^a, N. Cavallo^{a,c}, S. Di Guida^{a,d,2}, M. Esposito^{a,b}, F. Fabozzi^{a,c}, A.O.M. Iorio^{a,b}, G. Lanza^a, L. Lista^a, S. Meola^{a,d,2}, M. Merola^a, P. Paolucci^{a,2}, C. Sciacca^{a,b}, F. Thyssen

INFN Sezione di Padova ^a, Università di Padova ^b, Padova, Italy, Università di Trento ^c, Trento, Italy

P. Azzi^{a,2}, N. Bacchetta^a, M. Bellato^a, L. Benato^{a,b}, A. Boletti^{a,b}, A. Branca^{a,b}, M. Dall'Osso^{a,b,2}, T. Dorigo^a, U. Dosselli^a, F. Fanzago^a, A. Gozzelino^a, M. Gulmini^{a,30}, S. Lacaprara^a, M. Margoni^{a,b}, A.T. Meneguzzo^{a,b}, F. Montecassiano^a, M. Passaseo^a, J. Pazzini^{a,b}, M. Pegoraro^a, N. Pozzobon^{a,b}, P. Ronchese^{a,b}, F. Simonetto^{a,b}, E. Torassa^a, M. Tosi^{a,b}, S. Vanini^{a,b}, S. Ventura^a, M. Zanetti, P. Zotto^{a,b}, A. Zucchetta^{a,b,2}

INFN Sezione di Pavia ^a, Università di Pavia ^b, Pavia, Italy

A. Braghieri^a, A. Magnani^a, P. Montagna^{a,b}, S.P. Ratti^{a,b}, V. Re^a, C. Riccardi^{a,b}, P. Salvini^a, I. Vai^a, P. Vitulo^{a,b}

INFN Sezione di Perugia ^a, Università di Perugia ^b, Perugia, Italy

L. Alunni Solestizi^{a,b}, M. Biasini^{a,b}, G.M. Bilei^a, D. Ciangottini^{a,b,2}, L. Fanò^{a,b}, P. Lariccia^{a,b}, G. Mantovani^{a,b}, M. Menichelli^a, A. Saha^a, A. Santocchia^{a,b}, A. Spiezia^{a,b}

INFN Sezione di Pisa ^a, Università di Pisa ^b, Scuola Normale Superiore di Pisa ^c, Pisa, Italy

K. Androsov^{a,31}, P. Azzurri^a, G. Bagliesi^a, J. Bernardini^a, T. Boccali^a, G. Broccolo^{a,c}, R. Castaldi^a, M.A. Ciocci^{a,31}, R. Dell'Orso^a, S. Donato^{a,c,2}, G. Fedi, L. Foà^{a,c†}, A. Giassi^a, M.T. Grippo^{a,31}, F. Ligabue^{a,c}, T. Lomtadze^a, L. Martini^{a,b}, A. Messineo^{a,b}, F. Palla^a, A. Rizzi^{a,b}, A. Savoy-Navarro^{a,32}, A.T. Serban^a, P. Spagnolo^a, P. Squillacioti^{a,31}, R. Tenchini^a, G. Tonelli^{a,b}, A. Venturi^a, P.G. Verdini^a

INFN Sezione di Roma ^a, Università di Roma ^b, Roma, Italy

L. Barone^{a,b}, F. Cavallari^a, G. D'imperio^{a,b,2}, D. Del Re^{a,b}, M. Diemoz^a, S. Gelli^{a,b}, C. Jorda^a, E. Longo^{a,b}, F. Margaroli^{a,b}, P. Meridiani^a, G. Organtini^{a,b}, R. Paramatti^a, F. Preiato^{a,b}, S. Rahatlou^{a,b}, C. Rovelli^a, F. Santanastasio^{a,b}, P. Traczyk^{a,b,2}

INFN Sezione di Torino ^a, Università di Torino ^b, Torino, Italy, Università del Piemonte Orientale ^c, Novara, Italy

N. Amapane^{a,b}, R. Arcidiacono^{a,c,2}, S. Argiro^{a,b}, M. Arneodo^{a,c}, R. Bellan^{a,b}, C. Biino^a, N. Cartiglia^a, M. Costa^{a,b}, R. Covarelli^{a,b}, A. Degano^{a,b}, N. Demaria^a, L. Finco^{a,b,2}, B. Kiani^{a,b}, C. Mariotti^a, S. Maselli^a, E. Migliore^{a,b}, V. Monaco^{a,b}, E. Monteil^{a,b}, M. Musich^a, M.M. Obertino^{a,b}, L. Pacher^{a,b}, N. Pastrone^a, M. Pelliccioni^a, G.L. Pinna Angioni^{a,b}, F. Ravera^{a,b}, A. Romero^{a,b}, M. Ruspa^{a,c}, R. Sacchi^{a,b}, A. Solano^{a,b}, A. Staiano^a, U. Tamponi^a

INFN Sezione di Trieste ^a, Università di Trieste ^b, Trieste, Italy

S. Belforte^a, V. Candelise^{a,b,2}, M. Casarsa^a, F. Cossutti^a, G. Della Ricca^{a,b}, B. Gobbo^a, C. La Licata^{a,b}, M. Marone^{a,b}, A. Schizzi^{a,b}, A. Zanetti^a

Kangwon National University, Chunchon, Korea

A. Kropivnitskaya, S.K. Nam

Kyungpook National University, Daegu, Korea

D.H. Kim, G.N. Kim, M.S. Kim, D.J. Kong, S. Lee, Y.D. Oh, A. Sakharov, D.C. Son

Chonbuk National University, Jeonju, Korea

J.A. Brochero Cifuentes, H. Kim, T.J. Kim, M.S. Ryu

Chonnam National University, Institute for Universe and Elementary Particles, Kwangju, Korea

S. Song

Korea University, Seoul, Korea

S. Choi, Y. Go, D. Gyun, B. Hong, M. Jo, H. Kim, Y. Kim, B. Lee, K. Lee, K.S. Lee, S. Lee, S.K. Park, Y. Roh

Seoul National University, Seoul, Korea

H.D. Yoo

University of Seoul, Seoul, Korea

M. Choi, H. Kim, J.H. Kim, J.S.H. Lee, I.C. Park, G. Ryu

Sungkyunkwan University, Suwon, Korea

Y. Choi, Y.K. Choi, J. Goh, D. Kim, E. Kwon, J. Lee, I. Yu

Vilnius University, Vilnius, Lithuania

A. Juodagalvis, J. Vaitkus

National Centre for Particle Physics, Universiti Malaya, Kuala Lumpur, Malaysia

I. Ahmed, Z.A. Ibrahim, J.R. Komaragiri, M.A.B. Md Ali³³, F. Mohamad Idris³⁴, W.A.T. Wan Abdullah, M.N. Yusli

Centro de Investigacion y de Estudios Avanzados del IPN, Mexico City, Mexico

E. Casimiro Linares, H. Castilla-Valdez, E. De La Cruz-Burelo, I. Heredia-de La Cruz³⁵, A. Hernandez-Almada, R. Lopez-Fernandez, A. Sanchez-Hernandez

Universidad Iberoamericana, Mexico City, Mexico

S. Carrillo Moreno, F. Vazquez Valencia

Benemerita Universidad Autonoma de Puebla, Puebla, Mexico

I. Pedraza, H.A. Salazar Ibarguen

Universidad Autónoma de San Luis Potosí, San Luis Potosí, Mexico

A. Morelos Pineda

University of Auckland, Auckland, New Zealand

D. Krofcheck

University of Canterbury, Christchurch, New Zealand

P.H. Butler

National Centre for Physics, Quaid-I-Azam University, Islamabad, Pakistan

A. Ahmad, M. Ahmad, Q. Hassan, H.R. Hoorani, W.A. Khan, T. Khurshid, M. Shoaib

National Centre for Nuclear Research, Swierk, Poland

H. Bialkowska, M. Bluj, B. Boimska, T. Frueboes, M. Górski, M. Kazana, K. Nawrocki, K. Romanowska-Rybinska, M. Szleper, P. Zalewski

Institute of Experimental Physics, Faculty of Physics, University of Warsaw, Warsaw, Poland

G. Brona, K. Bunkowski, K. Doroba, A. Kalinowski, M. Konecki, J. Krolikowski, M. Misiura, M. Olszewski, M. Walczak

Laboratório de Instrumentação e Física Experimental de Partículas, Lisboa, Portugal

P. Bargassa, C. Beirão Da Cruz E Silva, A. Di Francesco, P. Faccioli, P.G. Ferreira Parracho,

M. Gallinaro, N. Leonardo, L. Lloret Iglesias, F. Nguyen, J. Rodrigues Antunes, J. Seixas, O. Toldaiev, D. Vadrucio, J. Varela, P. Vischia

Joint Institute for Nuclear Research, Dubna, Russia

S. Afanasiev, P. Bunin, M. Gavrilenko, I. Golutvin, I. Gorbunov, A. Kamenev, V. Karjavin, V. Konoplyanikov, A. Lanev, A. Malakhov, V. Matveev³⁶, P. Moisezenz, V. Palichik, V. Perelygin, S. Shmatov, S. Shulha, N. Skatchkov, V. Smirnov, A. Zarubin

Petersburg Nuclear Physics Institute, Gatchina (St. Petersburg), Russia

V. Golovtsov, Y. Ivanov, V. Kim³⁷, E. Kuznetsova, P. Levchenko, V. Murzin, V. Oreshkin, I. Smirnov, V. Sulimov, L. Uvarov, S. Vavilov, A. Vorobyev

Institute for Nuclear Research, Moscow, Russia

Yu. Andreev, A. Dermenev, S. Gninenko, N. Golubev, A. Karneyeu, M. Kirsanov, N. Krasnikov, A. Pashenkov, D. Tlisov, A. Toropin

Institute for Theoretical and Experimental Physics, Moscow, Russia

V. Epshteyn, V. Gavrillov, N. Lychkovskaya, V. Popov, I. Pozdnyakov, G. Safronov, A. Spiridonov, E. Vlasov, A. Zhokin

National Research Nuclear University 'Moscow Engineering Physics Institute' (MEPhI), Moscow, Russia

A. Bylinkin

P.N. Lebedev Physical Institute, Moscow, Russia

V. Andreev, M. Azarkin³⁸, I. Dremin³⁸, M. Kirakosyan, A. Leonidov³⁸, G. Mesyats, S.V. Rusakov, A. Vinogradov

Skobeltsyn Institute of Nuclear Physics, Lomonosov Moscow State University, Moscow, Russia

A. Baskakov, A. Belyaev, E. Boos, M. Dubinin³⁹, L. Dudko, A. Ershov, A. Gribushin, V. Klyukhin, O. Kodolova, I. Lokhtin, I. Myagkov, S. Obraztsov, S. Petrushanko, V. Savrin, A. Snigirev

State Research Center of Russian Federation, Institute for High Energy Physics, Protvino, Russia

I. Azhgirey, I. Bayshev, S. Bitioukov, V. Kachanov, A. Kalinin, D. Konstantinov, V. Krychkine, V. Petrov, R. Ryutin, A. Sobol, L. Tourtchanovitch, S. Troshin, N. Tyurin, A. Uzunian, A. Volkov

University of Belgrade, Faculty of Physics and Vinca Institute of Nuclear Sciences, Belgrade, Serbia

P. Adzic⁴⁰, M. Ekmedzic, J. Milosevic, V. Rekovic

Centro de Investigaciones Energéticas Medioambientales y Tecnológicas (CIEMAT), Madrid, Spain

J. Alcaraz Maestre, E. Calvo, M. Cerrada, M. Chamizo Llatas, N. Colino, B. De La Cruz, A. Delgado Peris, D. Domínguez Vázquez, A. Escalante Del Valle, C. Fernandez Bedoya, J.P. Fernández Ramos, J. Flix, M.C. Fouz, P. Garcia-Abia, O. Gonzalez Lopez, S. Goy Lopez, J.M. Hernandez, M.I. Josa, E. Navarro De Martino, A. Pérez-Calero Yzquierdo, J. Puerta Pelayo, A. Quintario Olmeda, I. Redondo, L. Romero, M.S. Soares

Universidad Autónoma de Madrid, Madrid, Spain

C. Albajar, J.F. de Trocóniz, M. Missiroli, D. Moran

Universidad de Oviedo, Oviedo, Spain

J. Cuevas, J. Fernandez Menendez, S. Folgueras, I. Gonzalez Caballero, E. Palencia Cortezon, J.M. Vizan Garcia

Instituto de Física de Cantabria (IFCA), CSIC-Universidad de Cantabria, Santander, Spain

I.J. Cabrillo, A. Calderon, J.R. Castiñeiras De Saa, P. De Castro Manzano, J. Duarte Campderros, M. Fernandez, J. Garcia-Ferrero, G. Gomez, A. Lopez Virto, J. Marco, R. Marco, C. Martinez Rivero, F. Matorras, F.J. Munoz Sanchez, J. Piedra Gomez, T. Rodrigo, A.Y. Rodríguez-Marrero, A. Ruiz-Jimeno, L. Scodellaro, I. Vila, R. Vilar Cortabitarte

CERN, European Organization for Nuclear Research, Geneva, Switzerland

D. Abbaneo, E. Auffray, G. Auzinger, M. Bachtis, P. Baillon, A.H. Ball, D. Barney, A. Benaglia, J. Bendavid, L. Benhabib, J.F. Benitez, G.M. Berruti, P. Bloch, A. Bocci, A. Bonato, C. Botta, H. Breuker, T. Camporesi, G. Cerminara, S. Colafranceschi⁴¹, M. D'Alfonso, D. d'Enterria, A. Dabrowski, V. Daponte, A. David, M. De Gruttola, F. De Guio, A. De Roeck, S. De Visscher, E. Di Marco, M. Dobson, M. Dordevic, B. Dorney, T. du Pree, M. Dünser, N. Dupont, A. Elliott-Peisert, G. Franzoni, W. Funk, D. Gigi, K. Gill, D. Giordano, M. Girone, F. Glege, R. Guida, S. Gundacker, M. Guthoff, J. Hammer, P. Harris, J. Hegeman, V. Innocente, P. Janot, H. Kirschenmann, M.J. Kortelainen, K. Kousouris, K. Krajczar, P. Lecoq, C. Lourenço, M.T. Lucchini, N. Magini, L. Malgeri, M. Mannelli, A. Martelli, L. Masetti, F. Meijers, S. Mersi, E. Meschi, F. Moortgat, S. Morovic, M. Mulders, M.V. Nemallapudi, H. Neugebauer, S. Orfanelli⁴², L. Orsini, L. Pape, E. Perez, M. Peruzzi, A. Petrilli, G. Petrucciani, A. Pfeiffer, D. Piparo, A. Racz, G. Rolandi⁴³, M. Rovere, M. Ruan, H. Sakulin, C. Schäfer, C. Schwick, A. Sharma, P. Silva, M. Simon, P. Sphicas⁴⁴, D. Spiga, J. Steggemann, B. Stieger, M. Stoye, Y. Takahashi, D. Treille, A. Triossi, A. Tsiros, G.I. Veres²¹, N. Wardle, H.K. Wöhri, A. Zagozdinska⁴⁵, W.D. Zeuner

Paul Scherrer Institut, Villigen, Switzerland

W. Bertl, K. Deiters, W. Erdmann, R. Horisberger, Q. Ingram, H.C. Kaestli, D. Kotlinski, U. Langenegger, D. Renker, T. Rohe

Institute for Particle Physics, ETH Zurich, Zurich, Switzerland

F. Bachmair, L. Bäni, L. Bianchini, M.A. Buchmann, B. Casal, G. Dissertori, M. Dittmar, M. Donegà, P. Eller, C. Grab, C. Heidegger, D. Hits, J. Hoss, G. Kasieczka, W. Lustermann, B. Mangano, M. Marionneau, P. Martinez Ruiz del Arbol, M. Masciovecchio, D. Meister, F. Micheli, P. Musella, F. Nessi-Tedaldi, F. Pandolfi, J. Pata, F. Pauss, L. Perrozzi, M. Quitnat, M. Rossini, A. Starodumov⁴⁶, M. Takahashi, V.R. Tavolaro, K. Theofilatos, R. Wallny

Universität Zürich, Zurich, Switzerland

T.K. Aarrestad, C. Amsler⁴⁷, L. Caminada, M.F. Canelli, V. Chiochia, A. De Cosa, C. Galloni, A. Hinzmann, T. Hreus, B. Kilminster, C. Lange, J. Ngadiuba, D. Pinna, P. Robmann, F.J. Ronga, D. Salerno, Y. Yang

National Central University, Chung-Li, Taiwan

M. Cardaci, K.H. Chen, T.H. Doan, Sh. Jain, R. Khurana, M. Konyushikhin, C.M. Kuo, W. Lin, Y.J. Lu, S.S. Yu

National Taiwan University (NTU), Taipei, Taiwan

Arun Kumar, R. Bartek, P. Chang, Y.H. Chang, Y.W. Chang, Y. Chao, K.F. Chen, P.H. Chen, C. Dietz, F. Fiori, U. Grundler, W.-S. Hou, Y. Hsiung, Y.F. Liu, R.-S. Lu, M. Miñano Moya, E. Petrakou, J.F. Tsai, Y.M. Tzeng

Chulalongkorn University, Faculty of Science, Department of Physics, Bangkok, Thailand

B. Asavapibhop, K. Kovitanggoon, G. Singh, N. Srimanobhas, N. Suwonjandee

Cukurova University, Adana, Turkey

A. Adiguzel, S. Cerci⁴⁸, Z.S. Demiroglu, C. Dozen, I. Dumanoglu, S. Girgis, G. Gokbulut, Y. Guler, E. Gurpinar, I. Hos, E.E. Kangal⁴⁹, A. Kayis Topaksu, G. Onengut⁵⁰, K. Ozdemir⁵¹, S. Ozturk⁵², B. Tali⁴⁸, H. Topakli⁵², M. Vergili, C. Zorbilmez

Middle East Technical University, Physics Department, Ankara, Turkey

I.V. Akin, B. Bilin, S. Bilmis, B. Isildak⁵³, G. Karapinar⁵⁴, M. Yalvac, M. Zeyrek

Bogazici University, Istanbul, Turkey

E.A. Albayrak⁵⁵, E. Gülmez, M. Kaya⁵⁶, O. Kaya⁵⁷, T. Yetkin⁵⁸

Istanbul Technical University, Istanbul, Turkey

K. Cankocak, S. Sen⁵⁹, F.I. Vardarli

Institute for Scintillation Materials of National Academy of Science of Ukraine, Kharkov, Ukraine

B. Grynyov

National Scientific Center, Kharkov Institute of Physics and Technology, Kharkov, Ukraine

L. Levchuk, P. Sorokin

University of Bristol, Bristol, United Kingdom

R. Aggleton, F. Ball, L. Beck, J.J. Brooke, E. Clement, D. Cussans, H. Flacher, J. Goldstein, M. Grimes, G.P. Heath, H.F. Heath, J. Jacob, L. Kreczko, C. Lucas, Z. Meng, D.M. Newbold⁶⁰, S. Paramesvaran, A. Poll, T. Sakuma, S. Seif El Nasr-storey, S. Senkin, D. Smith, V.J. Smith

Rutherford Appleton Laboratory, Didcot, United Kingdom

K.W. Bell, A. Belyaev⁶¹, C. Brew, R.M. Brown, D. Cieri, D.J.A. Cockerill, J.A. Coughlan, K. Harder, S. Harper, E. Olaiya, D. Petyt, C.H. Shepherd-Themistocleous, A. Thea, L. Thomas, I.R. Tomalin, T. Williams, W.J. Womersley, S.D. Worm

Imperial College, London, United Kingdom

M. Baber, R. Bainbridge, O. Buchmuller, A. Bundock, D. Burton, S. Casasso, M. Citron, D. Colling, L. Corpe, N. Cripps, P. Dauncey, G. Davies, A. De Wit, M. Della Negra, P. Dunne, A. Elwood, W. Ferguson, J. Fulcher, D. Futyan, G. Hall, G. Iles, M. Kenzie, R. Lane, R. Lucas⁶⁰, L. Lyons, A.-M. Magnan, S. Malik, J. Nash, A. Nikitenko⁴⁶, J. Pela, M. Pesaresi, K. Petridis, D.M. Raymond, A. Richards, A. Rose, C. Seez, A. Tapper, K. Uchida, M. Vazquez Acosta⁶², T. Virdee, S.C. Zenz

Brunel University, Uxbridge, United Kingdom

J.E. Cole, P.R. Hobson, A. Khan, P. Kyberd, D. Leggat, D. Leslie, I.D. Reid, P. Symonds, L. Teodorescu, M. Turner

Baylor University, Waco, USA

A. Borzou, K. Call, J. Dittmann, K. Hatakeyama, A. Kasmi, H. Liu, N. Pastika

The University of Alabama, Tuscaloosa, USA

O. Charaf, S.I. Cooper, C. Henderson, P. Rumerio

Boston University, Boston, USA

A. Avetisyan, T. Bose, C. Fantasia, D. Gastler, P. Lawson, D. Rankin, C. Richardson, J. Rohlf, J. St. John, L. Sulak, D. Zou

Brown University, Providence, USA

J. Alimena, E. Berry, S. Bhattacharya, D. Cutts, N. Dhingra, A. Ferapontov, A. Garabedian, J. Hakala, U. Heintz, E. Laird, G. Landsberg, Z. Mao, M. Narain, S. Piperov, S. Sagir, T. Sinthuprasith, R. Syarif

University of California, Davis, Davis, USA

R. Breedon, G. Breto, M. Calderon De La Barca Sanchez, S. Chauhan, M. Chertok, J. Conway, R. Conway, P.T. Cox, R. Erbacher, M. Gardner, W. Ko, R. Lander, M. Mulhearn, D. Pellett, J. Pilot, F. Ricci-Tam, S. Shalhout, J. Smith, M. Squires, D. Stolp, M. Tripathi, S. Wilbur, R. Yohay

University of California, Los Angeles, USA

R. Cousins, P. Everaerts, C. Farrell, J. Hauser, M. Ignatenko, D. Saltzberg, E. Takasugi, V. Valuev, M. Weber

University of California, Riverside, Riverside, USA

K. Burt, R. Clare, J. Ellison, J.W. Gary, G. Hanson, J. Heilman, M. Ivova PANEVA, P. Jandir, E. Kennedy, F. Lacroix, O.R. Long, A. Luthra, M. Malberti, M. Olmedo Negrete, A. Shrinivas, H. Wei, S. Wimpenny, B. R. Yates

University of California, San Diego, La Jolla, USA

J.G. Branson, G.B. Cerati, S. Cittolin, R.T. D'Agnolo, A. Holzner, R. Kelley, D. Klein, J. Letts, I. Macneill, D. Olivito, S. Padhi, M. Pieri, M. Sani, V. Sharma, S. Simon, M. Tadel, A. Vartak, S. Wasserbaech⁶³, C. Welke, F. Würthwein, A. Yagil, G. Zevi Della Porta

University of California, Santa Barbara, Santa Barbara, USA

D. Barge, J. Bradmiller-Feld, C. Campagnari, A. Dishaw, V. Dutta, K. Flowers, M. Franco Sevilla, P. Geffert, C. George, F. Golf, L. Gouskos, J. Gran, J. Incandela, C. Justus, N. Mccoll, S.D. Mullin, J. Richman, D. Stuart, I. Suarez, W. To, C. West, J. Yoo

California Institute of Technology, Pasadena, USA

D. Anderson, A. Apresyan, A. Bornheim, J. Bunn, Y. Chen, J. Duarte, A. Mott, H.B. Newman, C. Pena, M. Pierini, M. Spiropulu, J.R. Vlimant, S. Xie, R.Y. Zhu

Carnegie Mellon University, Pittsburgh, USA

M.B. Andrews, V. Azzolini, A. Calamba, B. Carlson, T. Ferguson, M. Paulini, J. Russ, M. Sun, H. Vogel, I. Vorobiev

University of Colorado Boulder, Boulder, USA

J.P. Cumalat, W.T. Ford, A. Gaz, F. Jensen, A. Johnson, M. Krohn, T. Mulholland, U. Nauenberg, K. Stenson, S.R. Wagner

Cornell University, Ithaca, USA

J. Alexander, A. Chatterjee, J. Chaves, J. Chu, S. Dittmer, N. Eggert, N. Mirman, G. Nicolas Kaufman, J.R. Patterson, A. Rinkevicius, A. Ryd, L. Skinnari, L. Soffi, W. Sun, S.M. Tan, W.D. Teo, J. Thom, J. Thompson, J. Tucker, Y. Weng, P. Wittich

Fermi National Accelerator Laboratory, Batavia, USA

S. Abdullin, M. Albrow, J. Anderson, G. Apollinari, L.A.T. Bauerdick, A. Beretvas, J. Berryhill, P.C. Bhat, G. Bolla, K. Burkett, J.N. Butler, H.W.K. Cheung, F. Chlebana, S. Cihangir, V.D. Elvira, I. Fisk, J. Freeman, E. Gottschalk, L. Gray, D. Green, S. Grünendahl, O. Gutsche, J. Hanlon, D. Hare, R.M. Harris, J. Hirschauer, B. Hooberman, Z. Hu, S. Jindariani, M. Johnson, U. Joshi, A.W. Jung, B. Klima, B. Kreis, S. Kwan[†], S. Lammel, J. Linacre, D. Lincoln, R. Lipton, T. Liu, R. Lopes De Sá, J. Lykken, K. Maeshima, J.M. Marraffino, V.I. Martinez Outschoorn,

S. Maruyama, D. Mason, P. McBride, P. Merkel, K. Mishra, S. Mrenna, S. Nahn, C. Newman-Holmes, V. O'Dell, K. Pedro, O. Prokofyev, G. Rakness, E. Sexton-Kennedy, A. Soha, W.J. Spalding, L. Spiegel, L. Taylor, S. Tkaczyk, N.V. Tran, L. Uplegger, E.W. Vaandering, C. Vernieri, M. Verzocchi, R. Vidal, H.A. Weber, A. Whitbeck, F. Yang

University of Florida, Gainesville, USA

D. Acosta, P. Avery, P. Bortignon, D. Bourilkov, A. Carnes, M. Carver, D. Curry, S. Das, G.P. Di Giovanni, R.D. Field, I.K. Furic, J. Hugon, J. Konigsberg, A. Korytov, J.F. Low, P. Ma, K. Matchev, H. Mei, P. Milenovic⁶⁴, G. Mitselmakher, D. Rank, R. Rossin, L. Shchutska, M. Snowball, D. Sperka, N. Terentyev, J. Wang, S. Wang, J. Yelton

Florida International University, Miami, USA

S. Hewamanage, S. Linn, P. Markowitz, G. Martinez, J.L. Rodriguez

Florida State University, Tallahassee, USA

A. Ackert, J.R. Adams, T. Adams, A. Askew, J. Bochenek, B. Diamond, J. Haas, S. Hagopian, V. Hagopian, K.F. Johnson, A. Khatiwada, H. Prosper, V. Veeraraghavan, M. Weinberg

Florida Institute of Technology, Melbourne, USA

M.M. Baarmand, V. Bhopatkar, M. Hohlmann, H. Kalakhety, D. Noonan, T. Roy, F. Yumiceva

University of Illinois at Chicago (UIC), Chicago, USA

M.R. Adams, L. Apanasevich, D. Berry, R.R. Betts, I. Bucinskaite, R. Cavanaugh, O. Evdokimov, L. Gauthier, C.E. Gerber, D.J. Hofman, P. Kurt, C. O'Brien, I.D. Sandoval Gonzalez, C. Silkworth, P. Turner, N. Varelas, Z. Wu, M. Zakaria

The University of Iowa, Iowa City, USA

B. Bilki⁶⁵, W. Clarida, K. Dilsiz, S. Durgut, R.P. Gandrajula, M. Haytmyradov, V. Khristenko, J.-P. Merlo, H. Mermerkaya⁶⁶, A. Mestvirishvili, A. Moeller, J. Nachtman, H. Ogul, Y. Onel, F. Ozok⁵⁵, A. Penzo, C. Snyder, P. Tan, E. Tiras, J. Wetzel, K. Yi

Johns Hopkins University, Baltimore, USA

I. Anderson, B.A. Barnett, B. Blumenfeld, D. Fehling, L. Feng, A.V. Gritsan, P. Maksimovic, C. Martin, M. Osherson, M. Swartz, M. Xiao, Y. Xin, C. You

The University of Kansas, Lawrence, USA

P. Baringer, A. Bean, G. Benelli, C. Bruner, R.P. Kenny III, D. Majumder, M. Malek, M. Murray, S. Sanders, R. Stringer, Q. Wang

Kansas State University, Manhattan, USA

A. Ivanov, K. Kaadze, S. Khalil, M. Makouski, Y. Maravin, A. Mohammadi, L.K. Saini, N. Skhirtladze, S. Toda

Lawrence Livermore National Laboratory, Livermore, USA

D. Lange, F. Rebassoo, D. Wright

University of Maryland, College Park, USA

C. Anelli, A. Baden, O. Baron, A. Belloni, B. Calvert, S.C. Eno, C. Ferraioli, J.A. Gomez, N.J. Hadley, S. Jabeen, R.G. Kellogg, T. Kolberg, J. Kunkle, Y. Lu, A.C. Mignerey, Y.H. Shin, A. Skuja, M.B. Tonjes, S.C. Tonwar

Massachusetts Institute of Technology, Cambridge, USA

A. Apyan, R. Barbieri, A. Baty, K. Bierwagen, S. Brandt, W. Busza, I.A. Cali, Z. Demiragli, L. Di Matteo, G. Gomez Ceballos, M. Goncharov, D. Gulhan, Y. Iiyama, G.M. Innocenti, M. Klute, D. Kovalskyi, Y.S. Lai, Y.-J. Lee, A. Levin, P.D. Luckey, A.C. Marini, C. Mcginn,

C. Mironov, X. Niu, C. Paus, D. Ralph, C. Roland, G. Roland, J. Salfeld-Nebgen, G.S.F. Stephans, K. Sumorok, M. Varma, D. Velicanu, J. Veverka, J. Wang, T.W. Wang, B. Wyslouch, M. Yang, V. Zhukova

University of Minnesota, Minneapolis, USA

B. Dahmes, A. Finkel, A. Gude, P. Hansen, S. Kalafut, S.C. Kao, K. Klapoetke, Y. Kubota, Z. Lesko, J. Mans, S. Nourbakhsh, N. Ruckstuhl, R. Rusack, N. Tambe, J. Turkewitz

University of Mississippi, Oxford, USA

J.G. Acosta, S. Oliveros

University of Nebraska-Lincoln, Lincoln, USA

E. Avdeeva, K. Bloom, S. Bose, D.R. Claes, A. Dominguez, C. Fangmeier, R. Gonzalez Suarez, R. Kamalieddin, J. Keller, D. Knowlton, I. Kravchenko, J. Lazo-Flores, F. Meier, J. Monroy, F. Ratnikov, J.E. Siado, G.R. Snow

State University of New York at Buffalo, Buffalo, USA

M. Alyari, J. Dolen, J. George, A. Godshalk, C. Harrington, I. Iashvili, J. Kaisen, A. Kharchilava, A. Kumar, S. Rappoccio

Northeastern University, Boston, USA

G. Alverson, E. Barberis, D. Baumgartel, M. Chasco, A. Hortiangtham, A. Massironi, D.M. Morse, D. Nash, T. Orimoto, R. Teixeira De Lima, D. Trocino, R.-J. Wang, D. Wood, J. Zhang

Northwestern University, Evanston, USA

K.A. Hahn, A. Kubik, N. Mucia, N. Odell, B. Pollack, A. Pozdnyakov, M. Schmitt, S. Stoynev, K. Sung, M. Trovato, M. Velasco

University of Notre Dame, Notre Dame, USA

A. Brinkerhoff, N. Dev, M. Hildreth, C. Jessop, D.J. Karmgard, N. Kellams, K. Lannon, S. Lynch, N. Marinelli, F. Meng, C. Mueller, Y. Musienko³⁶, T. Pearson, M. Planer, A. Reinsvold, R. Ruchti, G. Smith, S. Taroni, N. Valls, M. Wayne, M. Wolf, A. Woodard

The Ohio State University, Columbus, USA

L. Antonelli, J. Brinson, B. Bylsma, L.S. Durkin, S. Flowers, A. Hart, C. Hill, R. Hughes, W. Ji, K. Kotov, T.Y. Ling, B. Liu, W. Luo, D. Puigh, M. Rodenburg, B.L. Winer, H.W. Wulsin

Princeton University, Princeton, USA

O. Driga, P. Elmer, J. Hardenbrook, P. Hebda, S.A. Koay, P. Lujan, D. Marlow, T. Medvedeva, M. Mooney, J. Olsen, C. Palmer, P. Piroué, X. Quan, H. Saka, D. Stickland, C. Tully, J.S. Werner, A. Zuranski

University of Puerto Rico, Mayaguez, USA

S. Malik

Purdue University, West Lafayette, USA

V.E. Barnes, D. Benedetti, D. Bortoletto, L. Gutay, M.K. Jha, M. Jones, K. Jung, M. Kress, D.H. Miller, N. Neumeister, B.C. Radburn-Smith, X. Shi, I. Shipsey, D. Silvers, J. Sun, A. Svyatkovskiy, F. Wang, W. Xie, L. Xu

Purdue University Calumet, Hammond, USA

N. Parashar, J. Stupak

Rice University, Houston, USA

A. Adair, B. Akgun, Z. Chen, K.M. Ecklund, F.J.M. Geurts, M. Guilbaud, W. Li, B. Michlin, M. Northup, B.P. Padley, R. Redjimi, J. Roberts, J. Rorie, Z. Tu, J. Zabel

University of Rochester, Rochester, USA

B. Betchart, A. Bodek, P. de Barbaro, R. Demina, Y. Eshaq, T. Ferbel, M. Galanti, A. Garcia-Bellido, J. Han, A. Harel, O. Hindrichs, A. Khukhunaishvili, G. Petrillo, M. Verzetti

The Rockefeller University, New York, USA

L. Demortier

Rutgers, The State University of New Jersey, Piscataway, USA

S. Arora, A. Barker, J.P. Chou, C. Contreras-Campana, E. Contreras-Campana, D. Duggan, D. Ferencek, Y. Gershtein, R. Gray, E. Halkiadakis, D. Hidas, E. Hughes, S. Kaplan, R. Kunnawalkam Elayavalli, A. Lath, K. Nash, S. Panwalkar, M. Park, S. Salur, S. Schnetzer, D. Sheffield, S. Somalwar, R. Stone, S. Thomas, P. Thomassen, M. Walker

University of Tennessee, Knoxville, USA

M. Foerster, G. Riley, K. Rose, S. Spanier, A. York

Texas A&M University, College Station, USA

O. Bouhali⁶⁷, A. Castaneda Hernandez⁶⁷, M. Dalchenko, M. De Mattia, A. Delgado, S. Dildick, R. Eusebi, W. Flanagan, J. Gilmore, T. Kamon⁶⁸, V. Krutelyov, R. Montalvo, R. Mueller, I. Osipenkov, Y. Pakhotin, R. Patel, A. Perloff, J. Roe, A. Rose, A. Safonov, A. Tatarinov, K.A. Ulmer²

Texas Tech University, Lubbock, USA

N. Akchurin, C. Cowden, J. Damgov, C. Dragoiu, P.R. Duder, J. Faulkner, S. Kunori, K. Lamichhane, S.W. Lee, T. Libeiro, S. Undleeb, I. Volobouev

Vanderbilt University, Nashville, USA

E. Appelt, A.G. Delannoy, S. Greene, A. Gurrola, R. Janjam, W. Johns, C. Maguire, Y. Mao, A. Melo, H. Ni, P. Sheldon, B. Snook, S. Tuo, J. Velkovska, Q. Xu

University of Virginia, Charlottesville, USA

M.W. Arenton, S. Boutle, B. Cox, B. Francis, J. Goodell, R. Hirosky, A. Ledovskoy, H. Li, C. Lin, C. Neu, E. Wolfe, J. Wood, F. Xia

Wayne State University, Detroit, USA

C. Clarke, R. Harr, P.E. Karchin, C. Kottachchi Kankanamge Don, P. Lamichhane, J. Sturdy

University of Wisconsin, Madison, USA

D.A. Belknap, D. Carlsmith, M. Cepeda, A. Christian, S. Dasu, L. Dodd, S. Duric, E. Friis, B. Gomber, R. Hall-Wilton, M. Herndon, A. Hervé, P. Klabbers, A. Lanaro, A. Levine, K. Long, R. Loveless, A. Mohapatra, I. Ojalvo, T. Perry, G.A. Pierro, G. Polese, I. Ross, T. Ruggles, T. Sarangi, A. Savin, A. Sharma, N. Smith, W.H. Smith, D. Taylor, N. Woods

†: Deceased

1: Also at Vienna University of Technology, Vienna, Austria

2: Also at CERN, European Organization for Nuclear Research, Geneva, Switzerland

3: Also at State Key Laboratory of Nuclear Physics and Technology, Peking University, Beijing, China

4: Also at Institut Pluridisciplinaire Hubert Curien, Université de Strasbourg, Université de Haute Alsace Mulhouse, CNRS/IN2P3, Strasbourg, France

5: Also at National Institute of Chemical Physics and Biophysics, Tallinn, Estonia

-
- 6: Also at Skobeltsyn Institute of Nuclear Physics, Lomonosov Moscow State University, Moscow, Russia
 - 7: Also at Universidade Estadual de Campinas, Campinas, Brazil
 - 8: Also at Centre National de la Recherche Scientifique (CNRS) - IN2P3, Paris, France
 - 9: Also at Laboratoire Leprince-Ringuet, Ecole Polytechnique, IN2P3-CNRS, Palaiseau, France
 - 10: Also at Joint Institute for Nuclear Research, Dubna, Russia
 - 11: Also at Helwan University, Cairo, Egypt
 - 12: Now at Zewail City of Science and Technology, Zewail, Egypt
 - 13: Also at Ain Shams University, Cairo, Egypt
 - 14: Now at British University in Egypt, Cairo, Egypt
 - 15: Also at Beni-Suef University, Bani Sweif, Egypt
 - 16: Now at Fayoum University, El-Fayoum, Egypt
 - 17: Also at Université de Haute Alsace, Mulhouse, France
 - 18: Also at University of Hamburg, Hamburg, Germany
 - 19: Also at Brandenburg University of Technology, Cottbus, Germany
 - 20: Also at Institute of Nuclear Research ATOMKI, Debrecen, Hungary
 - 21: Also at Eötvös Loránd University, Budapest, Hungary
 - 22: Also at University of Debrecen, Debrecen, Hungary
 - 23: Also at Wigner Research Centre for Physics, Budapest, Hungary
 - 24: Also at University of Visva-Bharati, Santiniketan, India
 - 25: Now at King Abdulaziz University, Jeddah, Saudi Arabia
 - 26: Also at University of Ruhuna, Matara, Sri Lanka
 - 27: Also at Isfahan University of Technology, Isfahan, Iran
 - 28: Also at University of Tehran, Department of Engineering Science, Tehran, Iran
 - 29: Also at Plasma Physics Research Center, Science and Research Branch, Islamic Azad University, Tehran, Iran
 - 30: Also at Laboratori Nazionali di Legnaro dell'INFN, Legnaro, Italy
 - 31: Also at Università degli Studi di Siena, Siena, Italy
 - 32: Also at Purdue University, West Lafayette, USA
 - 33: Also at International Islamic University of Malaysia, Kuala Lumpur, Malaysia
 - 34: Also at Malaysian Nuclear Agency, MOSTI, Kajang, Malaysia
 - 35: Also at Consejo Nacional de Ciencia y Tecnología, Mexico city, Mexico
 - 36: Also at Institute for Nuclear Research, Moscow, Russia
 - 37: Also at St. Petersburg State Polytechnical University, St. Petersburg, Russia
 - 38: Also at National Research Nuclear University 'Moscow Engineering Physics Institute' (MEPhI), Moscow, Russia
 - 39: Also at California Institute of Technology, Pasadena, USA
 - 40: Also at Faculty of Physics, University of Belgrade, Belgrade, Serbia
 - 41: Also at Facoltà Ingegneria, Università di Roma, Roma, Italy
 - 42: Also at National Technical University of Athens, Athens, Greece
 - 43: Also at Scuola Normale e Sezione dell'INFN, Pisa, Italy
 - 44: Also at University of Athens, Athens, Greece
 - 45: Also at Warsaw University of Technology, Institute of Electronic Systems, Warsaw, Poland
 - 46: Also at Institute for Theoretical and Experimental Physics, Moscow, Russia
 - 47: Also at Albert Einstein Center for Fundamental Physics, Bern, Switzerland
 - 48: Also at Adiyaman University, Adiyaman, Turkey
 - 49: Also at Mersin University, Mersin, Turkey
 - 50: Also at Cag University, Mersin, Turkey
 - 51: Also at Piri Reis University, Istanbul, Turkey

- 52: Also at Gaziosmanpasa University, Tokat, Turkey
- 53: Also at Ozyegin University, Istanbul, Turkey
- 54: Also at Izmir Institute of Technology, Izmir, Turkey
- 55: Also at Mimar Sinan University, Istanbul, Istanbul, Turkey
- 56: Also at Marmara University, Istanbul, Turkey
- 57: Also at Kafkas University, Kars, Turkey
- 58: Also at Yildiz Technical University, Istanbul, Turkey
- 59: Also at Hacettepe University, Ankara, Turkey
- 60: Also at Rutherford Appleton Laboratory, Didcot, United Kingdom
- 61: Also at School of Physics and Astronomy, University of Southampton, Southampton, United Kingdom
- 62: Also at Instituto de Astrofísica de Canarias, La Laguna, Spain
- 63: Also at Utah Valley University, Orem, USA
- 64: Also at University of Belgrade, Faculty of Physics and Vinca Institute of Nuclear Sciences, Belgrade, Serbia
- 65: Also at Argonne National Laboratory, Argonne, USA
- 66: Also at Erzincan University, Erzincan, Turkey
- 67: Also at Texas A&M University at Qatar, Doha, Qatar
- 68: Also at Kyungpook National University, Daegu, Korea